

Prescription Dose Optimization for Personalized Radiotherapy

Yaru Pang

2023.07

A thesis submitted of the partial fulfilment of the requirements for the degree of Doctor
of Philosophy at University College London

Department of Medical Physics and Biomedical Engineering,

University College London,

Malet Place,

London,

WC1E 6BT

Declaration:

I, Yaru Pang, confirm that the work presented in this thesis is my own. Where information has been derived from other sources, I confirm that this has been indicated in the thesis.

.....

Signature

Acknowledgement

Life in UCL has been an extraordinary and unforgettable experience for me. I have gained much more than I imagined. The work in this thesis would not have been possible without the support and expertise of my supervisors and many collaborators.

First of all, I wish to express my deepest gratitude to my supervisor Professor Gary Royle, for providing me this excellent research opportunity in UCL. His professional guidance, clever ideas, valuable suggestions and comments have been extremely helpful during my PhD.

I would also like to thank my academic advisor Dr. Spyros Manolopoulos at Newcastle Upon Tyne Hospital, Dr. Michael Kosmin at UCLH, Dr. Catarina Veiga, Dr. Kate Ricketts, Dr. Stacey Holloway and Mr. Zhixin Zu from Varian for numerous helpful discussions, and for sharing with me valuable clinical suggestions and paper writing comments. Without their help, many of my publications would never have seen the light.

I would also like to express my thanks to Dr. Jailan Alshaikhi, Dr. Ying Zhang, Dr. Zhuoyan Shen, Dr. Xinhuan Zhou, Dr. Hang Ren, Dr. Fan Zhang, Dr. Chaoxu Chen, and many other friends' support and thoughtful discussions. I will never forget the pleasant and enjoyable moments when we gathered together. I could not forget all hard efforts we have made together.

I wish to thank my financial supporters, UCL and the China Scholarship Council, and data support from Shenzhen People's Hospital. In particular, I am very fortunate to have met Dr. Xianming Li for inspiring me lots of diligent and highly motivated spirit to work

hard and overcome challenges. I would also like to thank Prof. Bing Lu for leading me into radiotherapy research and gave me chances to gain clinical experiences.

Last but not least, I would like to express my deepest gratitude to my parents, parents in law and my husband for their unconditional love and support over the years. Without them it would have been impossible to complete or even start this work. They are the most caring and the kindest people I know, and they always love me no matter what and no matter where I am.

Abstract

As one of the most complex tumors, there are over a hundred tumor types of brain tumors. Among all treatment options, radiotherapy (RT) has been shown to greatly enhance the survival and local control rates for brain malignancies, and it is the standard method for brain tumor treatment, with better results than treating with only surgery or chemotherapy. Given the complexity of the biological system in brain tumors, an effective and personalized method for determining doses for radiation prescriptions is essential.

Tumor control probability (TCP) and normal tissue complication probability (NTCP) are indicators that can measure how the three-dimensional physical dose distributions are transferred into biological effects. In this thesis, I first investigated the parameter uncertainties in radiobiological models (*e.g.*, TCP and NTCP), and offered a personalized prescription dose prediction method based on an optimized model by considering individual variances in radiobiological parameters and constraints on several organs at risks (OARs). The therapeutic ratio for brain tumors following the proposed principles has been increased, while normal tissues have been protected.

Since glioblastoma multiforme (GBM) is one of the most malignant primary brain tumors. Local recurrence after RT is the most common mode of failure. Standard RT practice applies the prescription dose uniformly across tumor volume disregarding radiological tumor heterogeneity. I presented a novel strategy by using diffusion-weighted (DW-) MRI to calculate the cellular density at the voxel level within the gross tumor volume (GTV) in order to facilitate dose escalation to a biological target volume (BTV) to improve tumor control probability. The pre-treatment apparent diffusion coefficient (ADC) maps derived from DW-MRI of ten GBM patients treated with radical

chemoradiotherapy were used to calculate the local (per voxel) cellular density. Then, a TCP model was used to calculate voxelated TCP maps from the derived cell density values. The dose was escalated using a simultaneous integrated boost (SIB) to the BTV. By applying a SIB between 3.60Gy and 16.80Gy isotoxically to the BTV, the cohort's TCP has been increased by a mean of 8.44% (ranging from 7.19% to 16.84%).

As a promising alternative treatment, proton radiation therapy can significantly protect normal tissues due to the Bragg curve and thus the dose to tumor can have more headroom to increase, consequently increasing the tumor control rate and the therapeutic ratio. Therefore, proton therapy has been considered as a potential and increasingly popular treatment method. In this thesis, I investigated the uncertainty factors within the proton RT flow, and calculated the proton-related BTV and SIB, leading to an improvement of overall TCP. Comparisons between photon and proton dose optimization methods were also discussed. Exploitation of the proton-related SIB dose with radiosensitivity parameters from in-vitro biological experiments, 4.18Gy to 17.67Gy were provided to BTV, and TCP values were increased by 11.39% to 34.25%. The proton plans had lower doses to all the OARs and the doses to all non-tumor tissue (body minus PTV) was on average 3.31Gy lower than photon treatments, which means the OARs and normal tissues have been better protected.

Impact Statement

Since brain tumors have been considered as one of the most complex malignancies, in particular, glioblastoma multiforme (GBM) is the most frequent malignant brain tumor with low survival rates, the impact of optimising prescription doses in the radiotherapy treatment is significant. As has been reviewed, the range of current prescription doses is related to different types of brain tumors, both for adults and children, ranging from 20Gy to 90Gy, which indicates a huge difference. Such wide ranges are mainly due to differences in the patients' age, Karnofsky Performance Scale (KPS), brain tumor types and tumor locations. It is also noted that the European Organisation for Research and Treatment of Cancer (EORTC) or the Radiation Therapy Oncology Group (RTOG) guideline only suggested the range of the prescription doses for different brain tumor types, and dose ranges used in different cancer centers have their own standard protocols. Therefore, a personalized and accurate prescription dose prior to the physical radiotherapy treatment is investigated in this thesis. 27 patients with brain tumors were enrolled, and TCP and NTCP models were reimplemented for the proposed prescription dose optimisation methods. To further justify the proposed personalised method in practice, I first analysed the constraints of organs at risk, dose distribution, tumor types and radiotherapy techniques for each patient, and then the corresponding TCP/NTCP values were calculated. The experimental results demonstrated the outperformance in the therapeutic ratio improvement for all patients enrolled in the thesis. In addition, robust evaluation in proton therapy was performed and satisfied for all patients, which fulfilled the requirements of clinical treatments. Since this project was truly collaborative and cross-disciplinary, its impacts can go beyond the themes explicitly presented in this thesis.

The whole program architecture can be implemented in clinical research settings and used as a clinical tool for prescription dose optimization for individual patients. It is foreseeable that the proposed method can be used for the design of clinical trials in radiotherapy and this planning study is the first step to that end.

This technique can be applied to the design of clinical plans for both photon and proton, and through the comparison of radiotherapy plans, it is possible to analyse which radiotherapy regimen is more appropriate for different tumor types. For example, given that large-scale proton radiotherapy will not be available in the near future, it is more important to select tumors that are suitable for proton radiotherapy, while for some other tumours the existing photon radiotherapy can be optimised to achieve treatment goals.

Contents

List of Figures.....	11
List of Tables.....	14
Abbreviations Glossary	16
Chapter 1 Introduction.....	19
1.1 Aims and Objectives	21
1.2 Novelty of The Thesis.....	23
1.3 List of Publications	24
Chapter 2 Literature Review.....	26
2.1 Radiotherapy and Radiobiological Models for Brain Tumors.....	26
2.1.1 Brain Tumors and Radiotherapy	26
2.1.2 Current Radiation Prescription Doses for Brain Tumors	28
2.1.3 Radiobiological Models	35
2.1.3.1 Cell Survival Theory and Liner Quadratic (LQ) Model.....	36
2.1.3.2 Tumor Control Probability (TCP) Models	38
2.1.3.3 Normal Tissue Complication Probability (NTCP) Models	41
2.1.4 Conclusion.....	46
2.2 Dose Escalation and Imaging-based Dose Painting for Glioblastoma Multiforme	46
2.2.1 Glioblastoma Multiforme.....	46
2.2.2 Dose Escalation for Glioblastoma Multiforme	49
2.2.3 Diffusion-weighted MRI	59
2.2.4 Dose Painting	63
2.3 Preliminaries of Proton Therapy.....	68
Chapter 3 An In-silico Prescription-dose Optimisation Method.....	78
3.1 Introduction.....	78
3.2 Preliminaries of Radiotherapy Treatment Plans	80
3.3 Methods and Materials.....	83
3.3.1 Data Input and Augmentation	83
3.3.2 LQ-Poisson TCP under Inhomogeneous Dose Distribution	83
3.3.3 Parameter Selection.....	85
3.3.4 Calculations of TCP and NTCP	87
3.3.5 Prescription Dose Optimisation	88
3.3.6 Evaluation	91

3.4 Results and Discussions	93
3.4.1 TCP and NTCP Values	93
3.4.2 Optimized Prescription Doses	93
3.5 Conclusion	103
Chapter 4 Isotoxic Dose Escalated Radiotherapy for GBM Based on Diffusion-Weighted MRI and Tumor Control Probability	105
4.1 Introduction.....	105
4.2 Methods	108
4.2.1 Dataset.....	109
4.2.2 Cell Density Map	111
4.2.3 TCP Map	112
4.2.4 Biological Tumor Volume and Simultaneous Integrated Boost	113
4.2.5 SIB Isotoxic Dose-escalated Treatment Plan.....	114
4.3 Results.....	116
4.4 Discussions	124
Chapter 5 Proton Dose Painting for GBM.....	132
5.1 Introduction.....	132
5.2 Materials and Methods.....	134
5.2.1 Patients	134
5.2.2 Photon Dose Painting Plans	134
5.2.3 Proton Dose Painting Plans.....	135
5.2.4 Robust Evaluation	140
5.3 Results.....	140
5.3.1 SIB Doses and TCP Improvements.....	141
5.3.2 Doses to Target and OARs.....	145
5.3.3 Robustness Evaluation	149
5.4 Discussion.....	154
5.5 Conclusion	158
Chapter 6 Conclusion and Future Work.....	159
6.1 Summary of Contributions.....	159
6.2 Future Work.....	162
6.3 Final Remarks	165
References	166

List of Figures

Figure 2.1 Distribution of malignant primary central nervous system tumors by site [11]	27
Figure 2.2 Distribution of malignant primary central nervous system tumors by histology [11]	27
Figure 2.3 Cell survival curve of LQmodel [36].....	38
Figure 2.4 One-year OS rates and median OS months in studies with standard-dose and dose-escalated RT.....	54
Figure 2.5 One-year PFS rates and median PFS months in studies with standard-dose and dose-escalated RT.....	56
Figure 2.6 PDD of X-ray and Proton beams [157].....	71
Figure 2.7 An illustration of spread-out Bragg peak (SOBP) [156].....	73
Figure 2.8 A schematic of scattering system (a) and pencil beam scanning (PBS) system (b)	74
Figure 2.9 The spot weights at a single layer in proton treatment plan system.....	75
Figure 3.1 Plots of differential and cumulative DVHs.....	82
Figure 3.2 TCP and NTCP distributions for one patient. The TCP and OAR's NTCP have a range of uncertainties. Solid lines represent the median value of TCPs and each OAR's NTCPs, and dashed lines represent their lower and upper bound. D_{opt} denotes the optimized prescription dose.....	92

Figure 3.3 Dose volume histogram of patient #17 (a) and dose volume histogram of patient #13 (b) under optimized and original prescription doses. The dotted lines represent dose volumes after optimisation and the solid indicating the original dose volumes. For patient #17, the optimized prescription dose is greater than the original one. For patient #13, the optimized prescription dose is lower than the original one99

Figure 4.1 Cell density and the corresponding ADC values derived by Eidel *et al.* [181], where the line represents a linear fit performed herein using Equation 4.1, Pearson's $r = -0.40$, Spearman's $R_s = -0.48$, and both with p -values less than 0.01112

Figure 4.2 The flow charts of the methods applied to obtain escalated SIB isotoxic dose117

Figure 4.3 Frequency distribution histogram of the ADC values within GTV for 10 patients, where x -axis represents the ADC levels and y -axis represents the proportion of each ADC level.....118

Figure 4.4 Stepwise analysis to deduce BTV and SIB doses on the same axial plane of the example patient: (a) ADC image and outlined GTV, (b) the calculated cell density, (c) the TCP that corresponds to the clinical dose distribution (60 Gy in 30 fractions) and (d) the derived BTV119

Figure 4.5 TCP distributions with and without using the proposed method, where x -axis represents the TCP levels and y -axis represents the proportion of each TCP level. Blue bars represent the TCP values from all voxels in the clinical plan for this patient, while orange bars represent TCP values that corresponds to the SIB escalated dose to the BTV121

Figure 4.6 Relationships between TCP increases and the original TCP, and the number of tumor cells, respectively126

Figure 5.1 A flow chart of proton dose painting plan generation.136

Figure 5.2 Proton fields arrangement, a patient case study. This proton plan comprises three fields: 200 degree of gantry, 270 degree of gantry with 30 degree of couch, and 50 degree of gantry with 270 degree of couch	139
Figure 5.3 TCP distributions with different optimisation strategies in photon and proton radiotherapy	144
Figure 5.4 Dose distributions of photon dose painting plan (left column) and proton dose painting plan (right column) for an example patient case	145

List of Tables

Table 2.1 Summary of current prescription doses for brain tumors.....	29
Table 2.2 An overview of different TCP and NTCP models and their expressions.....	45
Table 2.3 Target dose requirements for GBM.....	48
Table 2.4 Failure pattern of recurrence in field based on clinical trials	49
Table 2.5 The survival rates and toxicities for newly diagnosed GBM when performing RT with standard dose levels.....	51
Table 2.6 The survival rates and toxicities for newly diagnosed GBM when performing dose-escalated RT	52
Table 2.7 The overview of using functional imaging for dose-escalated RT for newly diagnosed GBM.....	59
Table 2.8 Proton interactions with matter [1], [2].....	69
Table 3.1 The range of α and β for the Poisson LQ TCP model.....	86
Table 3.2 Parameters used in the LKB NTCP model.....	87
Table 3.3 OARs' tolerance [33], [42].....	89
Table 3.4 Optimised prescription doses for 17 brain tumor patients.....	94
Table 3.5 TCP increases based on different γ_{50} values.....	96
Table 3.6 Successful rates of OARs' metrics for 17 brain tumor patients.....	98
Table 3.7 Maximum doses to OARs under optimized and original prescription doses (PDs)	100
Table 4.1 Patients characteristics in terms of dose and gross tumor volume (GTV). D2% means the dose received in at least 2% of the GTV; D50% means the dose received in at least 50% of the GTV; D95% means the dose received in at least 95% of GTV; and D98% means the dose received in at least 98% of the GTV	110
Table 4.2 Critical organs tolerance doses and target dose requirements for GBM [15], [33], [42], [187]	115
Table 4.3 Results of proposed method for 10 GBM patients	121
Table 4.4 The volume of BTVs for each patient.....	123

Table 4.5 Doses of the OARs for the ten patients, expressed in terms of maximum doses in optic nerves, optic chiasm, eyes and lens and D0.1cc in brainstem. The dose tolerance indicated by the QUANTEC or RTOG 0825 protocols for those organs are also presented125

Table 5.1 Results of SIB doses and TCP increases for photon and proton dose painting plans, respectively.142

Table 5.2 Results of dose coverage in original plan and dose painting plans (the range shown the table represents the median, lowest and highest values among 10 patients)147

Table 5.3 Dose coverage for BTV and CTV from the complete proton dose painting plans of all patients.150

Table 5.4 Dose levels to OARs from the complete proton dose painting plans of all patients.....151

Table 5.5 The comparison of robust evaluation between the photon dose painting plans and the proton dose painting plans (lower *R* values with statistical difference are displayed as bold; and the range shown the table represents the median, lowest and highest values among 10 patients).153

Abbreviations Glossary

¹⁸ F-DOPA	3,4-dihydroxy-6-[¹⁸ F]-fluoro-L-phenylalanine
3D-CRT	3-dimensional conformal radiation therapy
ADC	Apparent diffusion coefficient
BED ₁₀	Biological equivalent dose in Gy, when assuming α/β ratio equals to 10
BTV	Biological tumor volume
CGE	Cobalt gray equivalent
CSI	Craniospinal irradiation
CT	Computed tomography
CTV	Clinical target volume
D ₅₀	The delivered dose resulting in 50% tumor control probability
DIR	Deformable image registration
DPBC	Dose painting by contours
DPBN	Dose painting by numbers
DVH	Dose-volume histograms
DW-MRI	Diffusion-weighted MRI
EORTC	European organization for research and treatment of cancer
EQD ₂	Equivalent dose
ESTRO	European society radiation oncology
EUD	Equivalent uniform dose
GARD	Genomic-adjusted radiation dose
GBM	Glioblastoma multiforme
GMD	Generalized mean dose
GTV	Gross tumor volume
ICRU	International commission on radiation units & measurements
IMPT	Intensity modulated proton therapy
IMRT	Intensity modulated radiation therapy
KPS	Karnofsky performance scale

LKB	Lyman-Kutcher-Burman
LQ	Liner quadratic
MFO	Multi field optimization
MPFS	Median progression-free survival months
MRI	Magnetic resonance imaging
MRSI	Magnetic resonance spectrum imaging
MS	Median overall survival months
NTCP	Normal tissue complication probability
OAR	Organs at risk
OS	Overall survival
PDD	Percentage depth dose curve
PET	Positron emission topography
PFS	Progression-free survival rate
PTCOG	Particle therapy co-operative group
PTV	Planning target volume
QUANTEC	Quantitative analyses of normal tissue effects in the clinic
ROC	Receiver operating characteristic
RSI	Radiosensitivity index
RT	Radiotherapy
RTOG	Radiation therapy oncology group
SDR	Sigmoidal dose response
SFO	Single field optimization
SIB	Simultaneous integrated boost
SIB	Simultaneously integrated boost
SOBP	Spread-out Bragg peak
SRT	Stereotactic radiation therapy
SUV	Standardized uptake values
TCD ₉₅	The dose required to achieve a tumor control rate of 95%
TCP	Tumor control probability
TD _{5/5}	The dose required to produce a probability of 5% of patients with severe radiation injury within 5 years after treatment

TD _{50/5}	The doses required to produce a probability of 50% patients have severe radiation injury within 5 years after treatment
TMZ	Temozolomide
TPS	Treatment planning system
TV	Target volume
VMAT	Volumetric modulated arc therapy

Chapter 1

Introduction

There have been over a hundred different types of brain tumors [3], [4]. Radiotherapy (RT) has been demonstrated to considerably improve brain tumor survival and local control rates [5], [6]. Prescription dosage is one of the primary factors that can affect the radiotherapy-related results [7]. Considering the complexity of the biological system in brain tumors, it is necessary to propose an effective and individualized approach for determining prescription doses for radiotherapy. This thesis presents a series of investigations towards a potential treatment for brain tumors using radiotherapy.

The conformity of the isodose line to the target volume (TV) and the normal tissue range involved in an RT plan is typically assessed using the three-dimensional dose distribution generated by the treatment planning system (TPS). Tumor control probability (TCP) and normal tissue complication probability (NTCP) have been used to model the biological impacts from the three-dimensional physical dose distributions, where TCP and NTCP denote the probability of removing tumor cells and radiological complications in normal tissues, respectively. This work proposed a method to optimize the prescription dose, for improving the therapeutic ratio and protecting normal tissues based on TCP and NTCP models. In particular, biological uncertainties in TCP and NTCP models have been discussed to provide a novel radiation treatment optimization.

Normally, the RT treatment plan is performed based on standard computed tomography (CT) imaging. I also assessed a specific type of magnetic resonance imaging (MRI) called diffusion-weighted MRI (DW-MRI), to provide additional information of tumor cell density versus conventional imaging methods. DW-MRI was used for defining the high risk of progression area and then designing the radiotherapy treatments to enable an increased dose to such area. The pre-treatment apparent diffusion coefficient (ADC) maps derived from DW-MRI of ten glioblastoma multiform (GBM) patients treated with radical chemoradiotherapy were used to calculate the local cellular density maps based on published data. Then, TCP models were used to calculate voxelated TCP maps from the derived cell density values. The dose was escalated using a simultaneous integrated boost (SIB) to the biological tumor volume (BTV), defined as the voxels for which the expected pre-boost TCP was in the lower quartile of the TCP range for each patient. The SIB dose was chosen so that the minimum TCP in the BTV was increased to match the average TCP of the whole tumor.

Proton RT-based BTV and SIB optimisation model has also been investigated to compare the proposed personalised dose escalation in photon radiotherapy, quantifying the expected TCP and therapeutic ratio increase. A collection of treatment uncertainties has been evaluated to allow the feasibility of delivering the proposed technique in clinical practice. The aim was to provide a basis upon which a future clinical trial could be designed. TCPs of brain tumor patients could be increased by escalating the dose to specific levels and intratumorally guided by the patient's biology (*e.g.*, cellularity), offering the possibility for personalized photon and proton RT treatments.

1.1 Aims and Objectives

Due to the complexity of the biological system and heterogeneity in brain tumors, this thesis aims to explore a personalized approach for prescribing radiation doses for individual patients with brain tumors in order to increase the therapeutic ratio. Personalized prescription of uniform tumor doses provides one way of improving the therapeutic ratio. In addition, a personalised dose-painting approach is investigated for further improving the therapeutic ration, individualizing doses on both voxel and patient levels. To achieve these research aims, I broke down them into the following technical objectives:

- Investigation of biological models, *i.e.*, TCP and NTCP models, to calculate personalised prescription doses, achieving higher therapeutic ratio and protecting the normal organs at risk within the radiation thresholds.
- Use of medical imaging-based biomarkers to enable a personalized radiobiological model to calculate the voxel-level TCP maps that correspond to the planned dose painting for each patient treatment.
- Performing personalised proton dose painting by use of the proton radiotherapy properties in the treatment of brain tumor patients.

The aims of each chapter are summarized herein:

- Chapter 2 highlights the theoretical background and reviews the work relevant to this thesis. Since this thesis is focussed upon brain tumor radiotherapy treatment, an overview of treatment procedures and retrospective studies for brain tumor

treatment is comprehensively reviewed. Following this, the current prescription doses for brain tumor, dose optimization studies and the state-of-the-art TCP and NTCP models are surveyed. After that, some necessary background of functional imaging and dose painting for precise radiotherapy are introduced. Finally, proton therapy is briefly described, and the benefits and limitations of photon and proton radiotherapy are discussed in detail.

- Chapter 3 presents a personalised radiation dose optimisation method by employing the biological uncertainty brought into TCP and NTCP models, with a focus on the commonly used Poisson-LQ model and LKB model in commercial treatment planning systems. Within the proposed method, characteristics of different organs at risk (OARs), and parameter variances in TCP and NTCP models are considered to produce an optimized prescription dose. Following this, planning system evaluation is performed by comparing whether the therapeutical ratio at the optimized dose is higher than using the original prescription dose.
- Chapter 4 investigates the relationship between apparent diffusion coefficient (ADC) and cell density, by employing the DW-MRI technique to estimate the number of tumor cells, a critical factor for the outcome of the treatment. ADC maps derived from DW-MRI are used to calculate the cellular density maps and TCP maps within the gross tumor volume (GTV) at the voxel level to define a personalized biological target volume (BTV). A simultaneous integrated boost (SIB) dose model is then proposed for individual patients, and the SIB dose is applied to BTV for the overall improvement in TCP.
- Chapter 5 proposes a novel dose painting approach for proton radiotherapy to achieve a heterogeneous dose distribution in the tumor area where high-risk

volumes are delivered with boosted doses. I investigated the technical features of proton radiotherapy, functional imaging and proton TCP model, to define the contour of BTV and calculate the SIB dose. Doses to OARs are decreased using this method, especially for visual pathways, with almost 0Gy in my patients' cohort. Characteristics, therapeutic ratio and robustness of proton and photon dose painting plans have been discussed.

- Chapter 6 concludes the thesis and suggests possible fruitful avenues for future research, such as an adaptive radiobiological treatment by tuning the BTV and prescribed dose per fraction.

1.2 Novelty of The Thesis

To address the aforementioned research objectives, novel contributions of the thesis are summarised as follows:

- A novel prescription-dose optimization method based on TCP and NTCP models, with a particular focus on prevailing models used in commercial treatment planning systems. (Chapter 3)
- A further investigation on various uncertainties within TCP and NTCP models to provide a robust prescription-dose prediction. (Chapter 3)
- A personalized treatment framework considering different OARs among patients, able to predict a prescription dose based on various constraints for individual patients. (Chapter 3)

- The first DW-MRI based dose painting method by investigating the voxel-level cell density for GBM. (Chapter 4)
- A novel method to produce voxel-level TCP maps based on voxel-level cell density analysis, where boosted doses are assigned into tumor area with lower TCP values (*i.e.*, area with higher cell density) for overall tumor control improvement. (Chapter 4)
- The first dose painting method for GBM in proton therapy which combines DW-MRI and voxel-level TCP maps for the improvement of tumor control and OARs protection. (Chapter 5)
- The robust optimisation and evaluation integrated range and position uncertainties specific to protons to better exploit the clinical potential for proton therapy. (Chapter 5)
- Quantitative and qualitative comparisons between photon dose painting and proton dose painting plans for GBM in terms of target coverage, normal tissue and OARs protection and robustness. (Chapter 5)

1.3 List of Publications

The work presented in this thesis based on the following publications:

- **Y. Pang, *et al.***, “Isotoxic dose escalated radiotherapy for glioblastoma based on diffusion weighted MRI and tumor control probability,” *British Journal of Radiology*, 2023 .

- Y. Zhang, J. Alshaikhi, R. Amos, W. Tan, V. Anaya, **Y. Pang**, G. Royle, E. Bar, “Pre treatment analysis of non-rigid variations can assist robust IMPT plan selection for head and neck patients”, *Medical Physics*, 2022.
- **Y. Pang, et al.**, “Medical Imaging Biomarker Discovery and Integration Towards AI-based Personalized Radiotherapy”, *Frontiers in Oncology*, 2021.
- **Y. Pang, et al.**, “Proton dose painting for glioblastoma based on DW-MRI and radiobiological models,” *Radiotherapy and Oncology (In preparation)*.

Oral Presentations

- **Y. Pang, et al.**, “Utilising diffusion-weighted MRI for isotoxic dose escalated radiotherapy for glioblastoma--a novel strategy”, European Society for Radiotherapy and Oncology Congress (ESTRO), 2021
- **Y. Pang, et al.**, “A dose optimization model for individualized brain tumor prescriptions based on biological uncertainties”, China Society for Radiotherapy and Oncology Congress (CSTRO), 2019
- **Y. Pang, et al.**, “Prescription dose optimization for specific Organ-at-risk based on radiobiology model”, Proton Physics Research and Implementation Group, 2018

Chapter 2

Literature Review

2.1 Radiotherapy and Radiobiological Models for Brain Tumor

2.1.1 Brain Tumor and Radiotherapy

Brain malignancy has been one of the most complex tumors in the world [3]. There have been more than a hundred tumor types in the central nervous system according to the study from Capper *et al.* [4]. Some brain tumors are difficult for surgical resection, such as medulloblastoma, ependymoma, atypical teratoid rhabdoid tumor, chordoma and chondrosarcoma of the skull base or cervical spine, since they have special anatomical positions [8]–[12]. Figures 2.1 and 2.2 show the distribution of brain tumors by tumor locations and types [13].

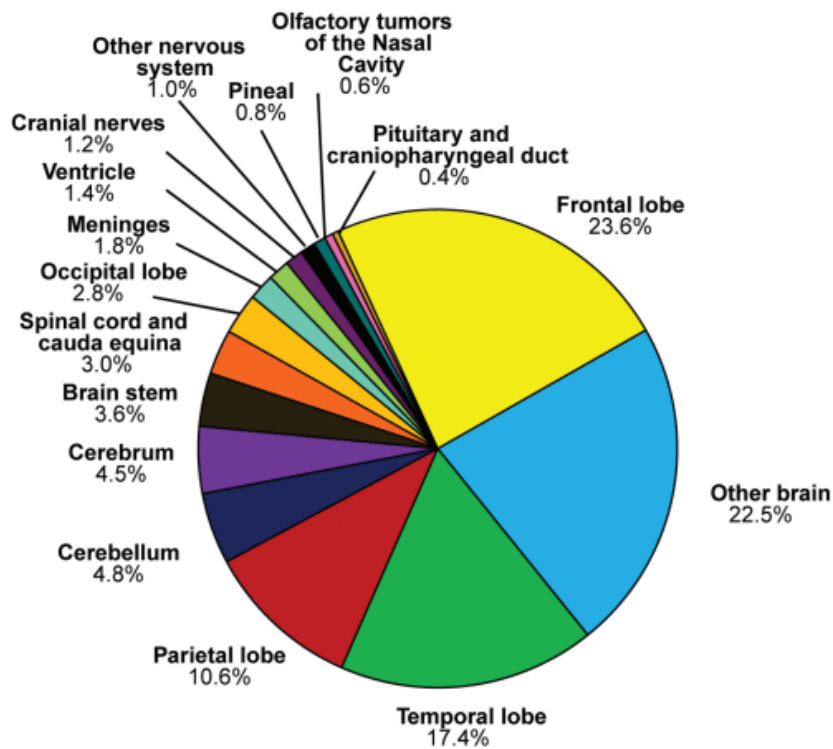


Figure 2.1 Distribution of malignant brain tumors by site [13].

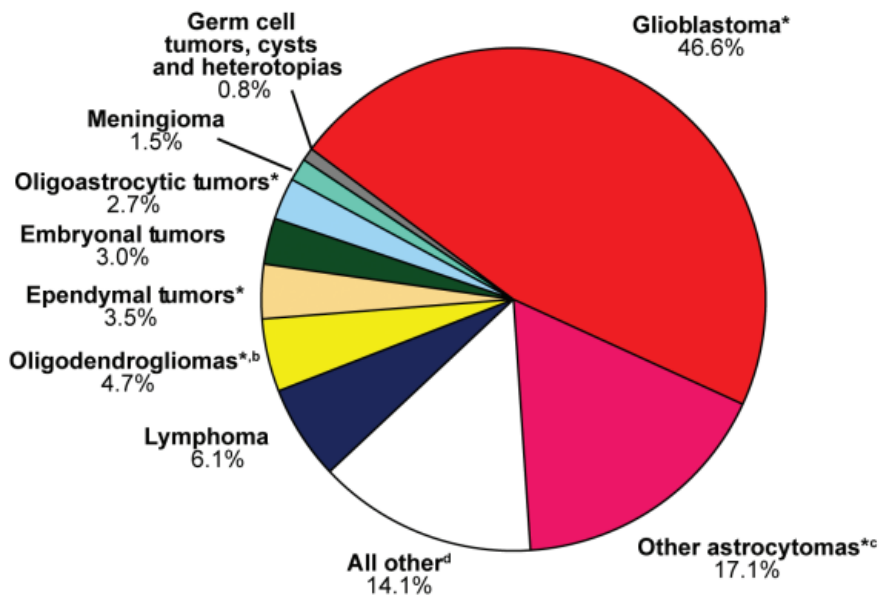


Figure 2.2 Distribution of malignant brain tumors by histology [13].

Among all the treatment methods, use of radiotherapy can significantly increase the survival and local control rates for brain tumors [6] and continues to be a standard method for these tumors, with improved outcomes over surgery and chemotherapy alone [11],

[14], [15]. Radiotherapy also continues to go through a rapid phase of technological development. Intensity-modulated radiotherapy, arc therapies, stereotactic therapy, image guidance and magnetic resonance imaging-linacs aim to deliver highly conformal beams to maximise tumor doses and reduce doses to normal tissues [16]. Recently, protons and heavy ions are used in radiotherapy to improve treatment outcomes, where a high radiation dose can be delivered to the tumor while minimizing the radiation dose to the surrounding healthy tissues, due to a characteristic known as Bragg peak, providing a more precise and effective treatment with fewer side effects [159, 160].

2.1.2 Current Radiation Prescription Doses for Brain Tumors

I presented a comprehensive review of prescription doses for brain tumors in recent published studies. Table 2.1 summarized prescription dose levels for different types of brain tumors (both for adults and children), where most of the prescription dose levels reviewed from the Perez and Brady's Principles and Practice of Radiation Oncology, the must-have standard reference for radiation oncologists. It is noted that the International Commission on Radiation Units & Measurements (ICRU) or the Radiation Therapy Oncology Group (RTOG) guideline only suggested the range of the prescription doses for different brain tumor types, and dose ranges used in different cancer centers have their own standard protocols [17], [18]. According to the survey in Table 2.1, the range of current prescription doses related to different types of brain tumors, both for adults and children, varies between 20Gy to 90Gy, which indicates a huge difference. Such wide ranges are mainly due to differences in the patient's age, Karnofsky Performance Scale (KPS), brain tumor types and tumor locations. Therefore, a personalized and accurate

prescription dose prior to the physical radiotherapy treatment needs to be investigated. In Chapter 3, I proposed a personalized prescription dose prediction and optimisation method, where the produced doses will be compared against currently released dose ranges shown in Table 2.1.

Table 2.1 Summary of current prescription doses for brain tumors.

Tumor types		Prescription dose	
Primary intracranial neoplasms	Malignant glioma	Grade III and IV are same with GBM	
	Glioblastoma (GBM)	Standard therapy	60 Gy in 30-33 fractions [19]
			45 Gy, 1.7-2 Gy daily [19]
			60 Gy in 6-7 weeks [19]
			60 Gy + 10Gy boost to a limited volume in 7 to 8 weeks [19]
			90 Gy [19]
			61.4 Gy in 69 fractions, 3 fractions/day [19]
			72 Gy in 60 fractions, 2 fractions/day [19]
			60-70 Cobalt Gray Equivalent (CGE) [19]
			90 CGE [19]
			Proton therapy

Primary intracranial neoplasms			50.4 CGE in 28 daily evening fractions [19]
		Treatment of older than 65-years old patients	60 Gy in 30 fractions [20]
			40 Gy in 15 fractions [20]
			34 Gy in 10 fractions [21]
	Anaplastic glioma		60 Gy in 30 fractions [19]
	Low-grade glioma	Pilocytic astrocytoma	50 to 55 Gy, 1.8-2Gy daily [19]
		Nonpilocytic/diffusely infiltrating gliomas	54 Gy, 1.8 Gy [22]
			59.4 Gy, 6.6 weeks [23]
			50.4, 28 fractions [24]
		64.8, 36 fractions [24]	
	Ependymoma		54-59.4 Gy [19]
	Medulloblastoma		35 Gy for whole brain [19]
			23.4 Gy craniospinal irradiation (CSI) for young adults, 36 Gy for the older [19]
			54-55.8 Gy for posterior fossa [19]
			45-50 Gy for spinal metastases [19]
			50-54 Gy for intracranial metastases [19]
	Meningioma	Grade 1	50-54 Gy in 25-30 fractions [19]
Grade 2-3		54 Gy in 30 fractions for atypical meningioma [19]	
		60 Gy in 33 fractions for malignant meningioma [19]	

	Craniopharyngiomas		50-54 Gy in 25 - 30 fractions [19]
			51.3 - 70 Gy [19]
	Vestibular schwannoma and neurofibroma		50-55 Gy in 25 to 30 fractions [19]
	Hemangioblastoma and hemangiopericytoma		50 - 60 Gy [19]
Pituitary gland cancer			45 Gy [25], [26]
Pediatric brain tumors	Conventional treatment	CNS	50 - 55.8 Gy, 1.8 Gy daily [19]
		Primary tumor of the spinal cord	50.4 Gy [19]
		Children younger than age 3 years	< 50.4 Gy [19]
		Radiosensitive tumors	30 - 45 Gy, 1.5 Gy daily [19]
	Astrocytic tumor in different grades	Low-grade astrocytoma (WHO Grades I and II)	45-50.4 Gy [19]
			59.4- 64.8 Gy [19]
			54-55 Gy for standard practice [19]
			45-50 Gy may be better [19]
			50-54 Gy depending on age and tumor location [19]
		High-grade astrocytoma (WHO Grades III and IV)	50-54 Gy due to the tolerance of optic chiasm [19]
			59-60 Gy [19]
	Optic pathway gliomas		45-50 Gy for younger than 5 years old [19]
			50-54 Gy for older than

Pediatric brain tumors	Astrocytic tumor in specific locations	Brainstem Gliomas	5 years old [19]	
			Focal tumors	54 Gy given over 6 weeks [19]
			Diffuse intrinsic pontine tumors (DIPGs)	54 Gy, 30 fractions [19]
				phase I/II: 64.8-78 Gy [19]
				50.4 Gy, 28 fractions, 2 fractions/day [19]
				39 Gy, 13 fractions [19]
	45 Gy, 15 fractions [19]			
	Astrocytoma of the spinal cord	50.4 Gy in 28 daily fractions [19]		
	Ependymal tumor	Myxopapillary ependymoma	50.4 Gy [19]	
		Ependymoma	45-54 Gy even 54 Gy [19]	
			54 Gy for children > 18months [19]	
			70.7 Gy [19]	
			70.4 Gy [19]	
		60 Gy [19]		
	Anaplastic ependymoma	54-55 Gy [19]		
59-60 Gy [19]				
Neuronal and mixed neuronal- glial tumors	50 Gy for typical neurocytomas [19]			

Pediatric brain tumors			54 Gy for atypical neurocytoma [19]
	Pineocytoma		50 to 55 Gy over 6 weeks [19]
	Embryonal tumors	Medulloblastoma	For > 3-years old, 35-36 Gy + boost to whole posterior fossa to 54-55.8 Gy [19]
			CSI 23.4 Gy [27]
			CSI 36 Gy [28]
		Supratentorial primitive neuroectodermal tumor (stPNET)	CSI dose >35 Gy and the primary site >54 Gy [19]
		Atypical teratoid/rhabdoid tumor	50.4 Gy for < 3-years old [19]
	54 Gy for > 3-years old [19]		
	Tumors of the sellar region	Craniopharyngioma	54 to 55 Gy in 30 daily fractions [19]
		Pituitary adenomas	45 to 50 Gy over 5 to 6 weeks [19]

Many researchers have been working on optimizing the current prescription dose. Scott *et al.* proposed a personalized prescription dose approach by using genomic markers of radiosensitivity [29]. They utilized the gene expression-based radiosensitivity index (RSI) and genomic-adjusted radiation dose (GARD) formalism to calculate a personalized RT prescription dose that biologically optimizes prescription dose for each patient. Results showed that personalized radiotherapy prescription doses deliver optimal doses to up-to

75% of the patients with non-small cell lung cancer, where they were restricted within the standard of care. However, this method highly relies on biological experiments at the gene level, thereby requiring high-end equipment usually unavailable for many institutions.

Even though a higher dosage is more effective in controlling tumors, it is hindered by the restricted dose capacity of normal tissues. Some researchers used receiver operating characteristic (ROC) to analyse the prescription dose [30], [31]. Su *et al.* calculated the cut-off value of PTV radiotherapy dose by ROC analysis [32]. In their study, different PTV radiotherapy doses correspond to different survival rates. However, ROC is able to analyze an optimized value based on only a single variable, while the prescription dose optimization is always a multi-variable problem.

There have been other works performing the clinical trials to observe the optimized prescription doses. It usually takes one to eight years for researchers to track the outcome of patients' treatment. Many patients usually cannot wait for the best treatment plan due to such a time-consuming process. Therefore, how to obtain an appropriate clinical trial design in terms of dose regimens in a patient acceptable time periods is of high value in clinical radiotherapy. Ajdari *et al.* from Harvard University published an editorial article in 2019 proposing that mathematical tools can help assess treatment efficiency and adapt the treatment plan based on individual biological responses [33]. Specifically, this study is based on two integral metrics: tumor control probability (TCP) and normal tissue complication probability (NTCP). Over the course of the treatment, the planner receives information (signals) about tumor/OAR responses through serial biomarkers and evaluates the adapted values of TCP and NTCP [33]. Inspired by this article, I decided to

construct a model to predict the prescription dose based on the differences between TCP and NTCP values. The details of my methods will be illustrated in Chapter 3.

2.1.3 Radiobiological Models

A fundamental way of improving both radical radiotherapy and palliative radiotherapy is to increase the therapeutic ratio, by increasing the radiation dose or the radiosensitivity of tumors, and reducing the dose to normal surrounding tissues. Both animal experiments and clinical radiotherapy practice have proven that the relationships of doses versus tumor control and the radiation complications are illustrated by TCP and NTCP models [34]. TCP represents the probability of eliminating all tumor clonogens. Normal tissue complications mean certain damage to organs or tissues after irradiation, such as radiation pneumonitis, blindness, pericarditis, *etc* [34]. Conventionally, a rise of TCP about 10%-20% per 10% increase in dose is expected [35]. However, if a tumor's TCP and NTCP curves are close to each other, the tumor treatment dose cannot be prescribed at a high level, otherwise serious radiation damage will occur. Therefore, how to obtain an accurate prescription dose has a great impact on controlling the tumor and reducing normal tissue complications. Clinicians generally give tumor doses (radiation prescription doses) to tumor lethal dose levels, which are defined as the doses required to achieve a tumor control rate of 95% (TCD₉₅) [36], [37]. However, doses high enough to control 95% of tumors can currently only be given to a few tumors, *e.g.*, prostate, due to the dose tolerance of the surrounding normal tissues. Emami *et al.* have compiled the lethal doses of different types and stages of tumors, and suggested that lethal doses vary with the tumor size, radiosensitivity and the range, pathological grade and degree of cell differentiation [37].

Since radiation inevitably cause damage to normal tissues and organs near the tumor, it is necessary to find out how much dosage is tolerable for a normal tissue, named normal tissue tolerance doses, including $TD_{5/5}$ and $TD_{50/5}$ [36], [37]. $TD_{5/5}$ is defined as the minimum injury dose, which means that, with standard treatment conditions, no more than 5% of patients with severe radiation injury caused by radiation therapy are within 5 years after treatment. $TD_{50/5}$ is defined as the maximum injury dose, which indicates that, with standard treatment conditions, no more than 50% patients have severe radiation injury due to radiation therapy within 5 years after treatment. In order to facilitate the design of treatment plans for radiation oncologists and radiophysicists, lethal doses of tumors and tolerated doses of normal tissues need to be considered. Emami investigated the tolerated doses of various normal tissues, corresponding to different endpoints [35].

2.1.3.1 Cell Survival Theory and Liner Quadratic (LQ) Model

TCP and NTCP values are indicators to measure how the three-dimensional physical dose distributions are transferred into biological effects, and they are calculated based on the cell survival theory [36]. After irradiation, the relationship between the fraction of cells retaining their reproductive integrity and the absorbed dose is shown in Figure 2.3. Radiation directly affects DNA molecules in the cell. As we all know, DNA has two strands. Single broken DNA strand can usually be repaired by the cell, while two broken DNA strands results in cell death [36]. When two strands are broken by a single particle, the probability of the lethal lesion is proportional to dose, then the cell survival rate (S) is written as

$$S = \exp(-\alpha D), \quad (2.1)$$

where α is the average probability that a cell can be killed by a single particle directly under the radiation dose D . If two broken strands come from two separate electrons, the probability is proportional to square of doses. S is then written as

$$S = \exp(-\beta D^2), \quad (2.2)$$

where β is the average probability that a cell can be killed by two particles directly under the square of radiation doses. Combining the aforementioned events, the Linear Quadratic (LQ) model is created and characterized as

$$S = \exp(-\alpha D - \beta D^2). \quad (2.3)$$

As is shown in Figure 2.3, there are two types of cell damage, α and β damage, where α damage is irreparable while β damage is repairable. D is the radiation dose. α and β values are the coefficients of dose proportional for the two types of damage. Their units are Gy^{-1} and Gy^{-2} respectively. When the effects of the two types of damage are equal, *i.e.*, $\alpha D = \beta D^2$, this leads to $D = \alpha/\beta$ which is a significant parameter of the LQ model. α/β value represents the curvature of the cell survival curve. The larger the value of α/β is, the more straight the cell survival curve will be. The value of α/β also represents the ability of cells to repair sub-lethal damage. Tissues with large α/β (*e.g.*, 10Gy) are called early response tissues, such as tumors, skin, mucous membranes, and intestinal epithelial cells, *etc.* They are sensitive to radiation and will occur damage early after irradiation. On the other hand, tissues with small α/β (*e.g.*, 3Gy) are called late reaction tissues, such as lung, kidney, spinal cord, and brain tissue, *etc.* They are not sensitive to radiation and damaged long time after the irradiation [38].

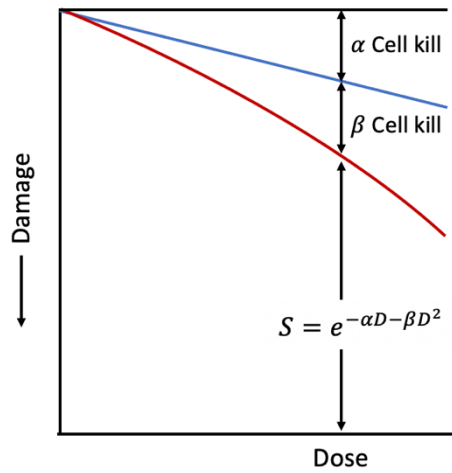


Figure 2.3 Cell survival curve of the LQ model [36].

2.1.3.2 Tumor Control Probability (TCP) Models

I. Schultheiss Logistic TCP Model

The Schultheiss logistic model can be used to assess the dose effect of both tumor and normal tissues. Because of the similarity of the dose-response curves between the tumor and normal tissues, *i.e.*, the TCP and NTCP curves are all S-shaped,

$$TCP(D) = \frac{1}{1 + \left(\frac{D_{50}}{D}\right)^k}, \quad (2.4)$$

where D represents total irradiation dose, D_{50} stands for the delivered dose resulting in 50% tumor control probability and k is a parameter describing the characteristics of the dose-response curve and is related to the slope of the dose-response curve.

Since the radiation dose to normal tissues is usually non-uniform, Niemierko proposed to use Equivalent Uniform Dose (EUD) instead of D in the Equation (2.4) and replaced k with $4\gamma_{50}$ [39]. γ is the normalized slope of the dose-response curve, defined as $\gamma = D \left(\frac{\partial TCP}{\partial D}\right)$.

γ_{50} is the slope at the point where the TCP value equals to 50%. Then, Equation (2.4) turns to be:

$$TCP(D) = \frac{1}{1 + \left(\frac{D_{50}}{EUD}\right)^{4\gamma_{50}}}. \quad (2.5)$$

The Schultheiss logistic model has only two parameters and its form is simple and intuitive. After introducing the EUD, it can predict the results of nonuniform irradiation results, which is beneficial to manual calculations.

II. Poisson TCP Model

When a tumor with N clonogenic cells is irradiated with a uniform dose D , the TCP follows a Poisson distribution, expressed as below:

$$TCP = \exp[-Np_s(D)], \quad (2.6)$$

where $p_s(D)$ is the survival rate of a single clone-derived cell after receiving D dose irradiation, expressed as

$$p_s(D) = \exp(-\alpha D). \quad (2.7)$$

Webb *et al.* derived the equations of N and α [40]

$$N = \ln 2 \exp\left(\gamma_{50} \frac{2}{\ln 2}\right), \quad (2.8)$$

$$\alpha = \frac{2}{\ln 2} \frac{\gamma_{50}}{D_{50}}. \quad (2.9)$$

As mentioned above, D_{50} and γ_{50} are used to describe the dose and the normalized slope at the point of 50% control probability, then Equation (2.6) can be rewritten as

$$TCP = \left(\frac{1}{2}\right)^{\exp\left[\frac{2\gamma_{50}\left(1-\frac{D}{D_{50}}\right)}{\ln 2}\right]} \quad (2.10)$$

For the case of heterogeneous irradiation, assuming all tumor subvolumes are independent, the overall probability of tumor control is the product of the probabilities of eliminating all clonogens in each tumor subvolume. Therefore, for heterogeneous dose distribution, Equation (2.10) can be rewritten as

$$TCP = \left(\frac{1}{2}\right)^{\sum_i V_i \exp\left[2\gamma_{50}\left(1-\frac{D_i}{D_{50}}\right)/\ln 2\right]}, \quad (2.11)$$

where D_{50} and γ_{50} are parameters we can choose and directly use from textbook [72]. A collection of tumor dose-response parameters (D_{50} and γ_{50}) extracted from single- and multi-institution datasets in terms of different tumor sites and grades has been summarized and published by Okunieff *et al.* [35].

III. Poisson Linear Quadratic TCP Model

Hall *et al.* combined the LQ model and the repair of tumor clone-derived cells to obtain a general Poisson LQ model [38]. If the dose distribution is homogeneous, then we have

$$TCP = \exp[-N \exp(-(\alpha + \beta d)D)], \quad (2.12)$$

where N is the initial number of clonogens, d is the dose in one fraction, D is the total dose, α and β are cell radio-sensitivity parameters as described in Section 2.1.3.1. Parameters of the Poisson LQ model were traditionally determined based on in-vitro experiments. Currently, a prevailing way to estimate parameters is from clinical data. However, there has already been enough clinical and experimental data to prove that it is a significant difference in the radio-sensitivity of tumor cells even within the same tumor [41]. Furthermore, the radio-sensitivity of tumor cells between patients' groups can vary greatly [41]. These differences affect the slope of the dose-response curve. Therefore, uncertainties of radio-sensitivity parameters, α and β , should be considered when using the Poisson LQ TCP model. For brain tumors, the values of α and β range from 0.04 to 0.102 and 0.0071 to 0.008, respectively [41]. A wide-ranging set of the parameters collected from literature can be used to build the model with a high degree of robustness, which is discussed in Chapter 3.

Under a uniform radiosensitivity, TCP values depend on the trade-off between the variations in dose and numbers of clonogenic cells [42]. If low-dose regions correspond to low clonogenic cell density then the TCP will not necessarily be reduced. However, there is a potential impact of ignoring patient-to-patient radiosensitivity variation in the TCP model. Webb and Nahum [42] suggested that the change of doses is related to clonogenic cell density and α . For dose-painting studies, the choice of α can affect the estimate of the optimised dose levels across the tumor. For example, a low α may result in over-estimating the degree to which doses should be varied with α . Therefore, it is necessary to consider patient-to-patient radiosensitivity variation in TCP calculations. The radiosensitivity parameters derived from clinical trials are more realistic than those obtained from in-vitro biological experiments, and will be more in line with in-vitro expectations by fitting a heterogeneous model [42]–[44].

The Poisson LQ model not only takes into account the statistical behavior of killing tumor cells, but also the repair of cells, and thus has currently become the most popular TCP model used by the mainstream TPS, such as PINNACLE from PHILIPS and Eclipse from VARIAN. In this thesis, I will use the Poisson LQ model to calculate TCP values.

2.1.3.3 Normal Tissue Complication Probability Models

I. Schultheiss Logistic NTCP Model

As described in Section 2.1.3.2, Schultheiss *et al.* derived a normal tissue dose-effect model from a generalized linear model [45], which can be both used in TCP and NTCP model, *i.e.*,

$$NTCP(V = 1, D) = \frac{1}{1 + \left(\frac{D_{50}}{D}\right)^k}. \quad (2.13)$$

In (2.13), D_{50} is the dose in the dose-response curve when $NTCP = 0.5$. k is a parameter describing the characteristics of the dose-response curve and is related to the slope of the dose-response curve. D_{50} can be replaced by the maximum injury tolerance dose $TD_{50/5}$. The relationship between these parameters is $k = 4\gamma_{50}$. Emami *et al.* used clinical data to enumerate the $TD_{50/5}$ for most normal tissues and organs in the human body [37]. Since the radiation dose to normal tissues is usually non-uniform, Niemierko proposed to use EUD instead of D in the Equation (2.13) [39], leading to

$$NTCP = \frac{1}{1 + \left(\frac{TD_{50/5}}{EUD}\right)^{4\gamma_{50}}}. \quad (2.14)$$

Equation (2.14) can be further simplified as

$$NTCP = \left(\frac{EUD}{TD_{50/5}}\right)^{4\gamma_{50}}. \quad (2.15)$$

II. Lyman-Kutcher-Burman NTCP model

Lyman proposed the first sigmoidal dose response (SDR) cumulative model to describe the dose response of the volume V in the normal tissue irradiated under the uniform dose of D [46]:

$$NTCP = \Phi\left(\frac{D - TD_{50/5}}{mTD_{50/5}}\right). \quad (2.16)$$

$\Phi(x)$ is the probability unit function

$$\begin{aligned} \Phi(x) &= \frac{1}{\sqrt{2\pi}} \int_{-\infty}^x e^{-t} dt \\ &= \frac{1}{2} \left[1 + \operatorname{erf}\left(\frac{x}{\sqrt{2}}\right)\right]. \end{aligned} \quad (2.17)$$

where $x = \frac{EUD - TD_{50/5}}{mTD_{50/5}}$. m is a parameter that controls the slope of the NTCP dose-response curve. With the development of radiotherapy technology, the level of non-uniformity in normal tissue has been increased. Kutcher and Burman improved the SDR model [47], [48]. They used EUD instead of D in Equation (2.16) to form the current universal Lyman-Kutcher-Burman (LKB) model,

$$NTCP = \Phi\left(\frac{EUD - D_{50}}{mD_{50}}\right). \quad (2.18)$$

Herein, in LKB model, the EUD is equal to a generalized mean dose (GMD), calculated from the dose-volume pairs (D_i, v_i) in the differential DVH (dDVH) using

$$GMD = (\sum_i V_i D_i^{1/n})^n, \quad (2.19)$$

where n is the volume effect factor, which determines the dose-volume dependence of a tissue and hence accounts for structural variations across tissues.

The most commonly used dose-response complication data for normal tissues was published by Burman *et al.* [44] and Emami *et al.* [34]. These data can estimate many distinct normal tissue types, corresponding to doses with complication rates of 5% and 50% for irradiation of one-third, two-thirds, and total organs. Burman *et al.* presented the estimates of the LKB model parameters for 27 normal tissues using these data [48]. In addition, uncertainties in the parameter values and the corresponding calculated NTCP values are indeterminate. With the development of radiotherapy, a number of works have provided parameter estimates for the LKB model, including brain stem, optical nerves and optical chiasma [49]–[53], Quantitative Analyses of Normal Tissue Effects in the Clinic (QUANTEC) suggested a set of uncertainties of the radiobiological parameters in the LKB model [54].

The Schultheiss logistic model is the foundation for both TCP and NTCP calculations, which considers only two parameters, characterized as a simple and intuitive form. The LKB model is a three-parameter DVH-based model, considering the irradiated volume of normal tissues, and its form is more mathematically complex than the Schultheiss logistic

model. The LKB model has been the most widely used tool to evaluate and compare treatment plans [55], and guide dose-escalation studies [56], [57], toxicity prediction and patient selection [58]. Research efforts to design biological-based treatment plans often employ the LKB model for the description of normal tissue complication probabilities [59], and to guide individual treatment plans [60]. The commercial TPS, such as PINNACLE from PHILIPS and Eclipse from VARIAN, have employed the LKB model to calculate NTCP. In this thesis, I will employ the LKB model and its parameter uncertainties to calculate NTCP values.

Table 2.2 An overview of different TCP and NTCP models and their expressions.

Type	Model	Equation and Parameters
TCP	Schultheiss logistic	$TCP(D) = \frac{1}{1 + \left(\frac{D_{50}}{EUD}\right)^{4\gamma_{50}}}$
		D_{50} : Delivered dose resulting in 50% tumor control probability. γ_{50} : Slope at the point of 50% tumor control probability.
	Poisson	$TCP = \left(\frac{1}{2}\right)^{\exp\left[\frac{2\gamma_{50}\left(1-\frac{D}{D_{50}}\right)}{\ln 2}\right]}$
		D_{50} : Delivered dose resulting in 50% tumor control probability. γ_{50} : Slope at the point of 50% tumor control probability.
	Poisson-LQ	$TCP = \exp[-N \exp(-(\alpha + \beta d)D)]$
		α : Average probability that a cell can be killed by a single particle directly under the radiation dose. β : Average probability that a cell can be killed by two particles directly under the square of radiation dose. N : The number of tumor clonogens.
NTCP	Schultheiss logistic	$NTCP = \left(\frac{EUD}{TD_{50/5}}\right)^{4\gamma_{50}}$
		$TD_{50/5}$: Tolerance dose of no more than 50% of patients with severe radiation injury caused by radiotherapy for 5 years after treatment. γ_{50} : Slope at the point of 50% tumor control probability.

		$NTCP = \Phi\left(\frac{EUD - TD_{50/5}}{mTD_{50/5}}\right)$
	LKB	<p>$TD_{50/5}$: Tolerance dose of no more than 50% of patients with severe radiation injury caused by radiotherapy for 5 years after treatment.</p> <p>m: The slope of the complication probability vs. dose curve.</p> <p>n: The volume dependence of the complication probability.</p>

2.1.4 Conclusion

Clinical and experimental evidence illustrated that TCP and NTCP show S-shaped curves with dose changes. A good treatment regimen should maximize the likelihood of tumor cure (high TCP) and minimize the risk of complications in normal tissues (low NTCP). In Chapter 3, the applications of TCP and NTCP in the treatment planning system is illustrated. The advantages of the TCP and NTCP radiobiological models are employed to consider biological optimization for dose prediction. In Chapter 4 and Chapter 5, the biological target volume (BTV) and biological optimization were further explored for dose optimization.

2.2 Dose Escalation and Imaging-based Dose Painting for GBM

2.2.1 Glioblastoma Multiforme

Glioblastoma multiforme (GBM) is the most common primary malignant brain tumor [61]. Figure 2.2 in Section 2.1.1 showed that GBM account for 46.6% of all the types of

brain tumors. To ensure patients with GBM undergoing radiotherapy in a safe and consistent manner, the standard treatment in UK is to use radiotherapy along with concurrent chemotherapy and adjuvant chemotherapy [62]. The Karnofsky Performance Scale (KPS) is used as an assessment tool for predicting the length of survival in terminally ill patients. The score of KPS ranges from 0 to 100. A KPS score approaching to 100 indicates the patient is better able to carry out daily activities. Generally, the age of 70 years is considered as the cut-off for radical therapy. According to the standard procedure for GBM treatment in UK [62], for patients under 70 years old and KPS values higher than 70, 60Gy in 30 daily fractions over 6 weeks is performed. For patients older than 70 years old and KPS less than 70, radiotherapy doses are only prescribed with 40.05Gy in 15 daily fractions over 3 weeks. Both groups are treated with concurrent chemotherapy and adjuvant chemotherapy using temozolomide (TMZ).

During the radiotherapy treatment, patients should be immobilized using thermoplastic shell in a supine position. The planning CT is usually scanned by 5mm slices and registered with pre- or post-operation MRI sequences (T1 plus gadolinium, T2, T2 FLAIR) [19]. In radical RT, the GTV is defined from the planning CT data and preoperative images from MRI fusion where possible. GTV is the enhanced tumor on MRI T1 images. Clinical target volume (CTV) is GTV plus the margin ranging from 2cm to 2.7cm [63]. PTV is defined as CTV plus the margin of 0.3cm-0.5cm. In the RT for GBM, the critical organs usually include brain stem, spinal cord, optic nerves, optic chiasma, retina and lenses. Their corresponding tolerance doses are evaluated according to the QUANTEC and Emami *et al.* [37], [54]. The dose requirements for tumor target are shown in Table 2.3. RapidArc intensity modulated radiation therapy (IMRT) is routinely considered as the RT technique for GBM in UK.

Table 2.3 Target dose requirements for GBM.

Dose Volume Index	Objective (% of Prescription Dose)
D_{99%}	90%
D_{95%}	95%
D_{50%}	50%
D_{5%}	105%
D_{2%}	107%

However, despite advanced diagnostic modalities and optimal multidisciplinary treatments that typically include maximal surgical resection, radiotherapy (RT) and systemic chemotherapy, the majority of patients with GBM still experience tumor progression and mortality. Most clinical trials reported that the median overall survival (OS) ranges from 14.6 to 16.7 months with a 2-year survival rate ranging from 26% to 33% [62]. Table 2.4 summarized the failure mode of the recurrence in field based on clinical trials. From Table 2.4, the in-field recurrence is the most common pattern for GBM, since most treatments cannot eradicate all tumor cells, explaining the high rate of recurrence. Molecular heterogeneity is one of the greatest challenges in developing effective treatment for patients with GBM [64]. Considering the diffuse nature of the disease, surgery is often insufficient. Reirradiation may help local disease control in a proportion of patients, but this approach is not always feasible due to the hazards of cumulative neurotoxicity [65]. Chemotherapy also has major limitations. Since most drugs cannot cross the bloodbrain barrier, penetration into tumor cells is limited [66].

Table 2.4 Failure pattern of recurrence in-field based on clinical trials.

	Number of enrolled patients	Recurrence in field
Milano <i>et al.</i> 2010 [67]	39	80%
McDonald <i>et al.</i> 2011 [68]	43	92%
Petrecca <i>et al.</i> 2013 [69]	20	90%
Sheriff <i>et al.</i> 2013 [70]	71	77%
Gebhardt <i>et al.</i> 2014 [71]	95	81%
Paulsson <i>et al.</i> 2014 [72]	78	77%
Choi <i>et al.</i> 2017 [73]	167	69%
Tini <i>et al.</i> 2018 [74]	129	79.1%
Gromeier <i>et al.</i> 2021 [75]	90	58%

2.2.2 Dose Escalation for GBM

Since the survival of GBM is poor and in-field recurrence is the most common failure pattern, indicating that the prescribed irradiation dose is not sufficient for tumors. Therefore, dose boosted radiotherapy has been explored to increase the tumor control [76], [67], [193]. Fitzek *et al.* conducted a phase II clinical trial to assess whether dose escalation to 90 cobalt gray equivalent (CEG) will improve local control and survival rate [193]. Their results showed that the median survival time was increased to 20 months. The dose of 90-CEG can prevent central recurrence. Tumor relapse usually occurred at the area next to the 90-CEG volume. However, challenges with radiation necrosis are expected to put a cap on attempts to increase local control by extending the radiation volume [193]. Tanaka *et al.* found that compared with conventional 60Gy RT, high-dose

(80-90Gy) RT significantly reduced the recurrence. The median survival in GBM patients was 16.2 months (12.8-19.6) for the high-dose group, while a survival period of 12.4 months (10.0-14.8) was reported for the patients using conventional dose levels [76]. With respect to the 2-year survival rate, 38.4% (23.5%–53.3%) and 11.4% (0.0%–25.3%) were reported for the high-dose group and conventional-dose group, respectively. Nakagawa *et al.* [77] found that 16 out of 19 patients have recurrences in the conventional 60Gy group, whereas only 4 of the 13 recurrences existed in the 90-Gy Group. However, patients treated with high dose levels may have higher risk of normal tissue complication. There were two patients in the high dose group with radiation necrosis and one of them has died. Therefore, high doses may reduce the recurrence but did not improve survival for GBM using 3-dimensional conformal radiation therapy (3D-CRT) technique, due to the increased related toxicity .

According to Minniti *et al.*'s research, contouring the target volumes by expanding the postoperative cavity with 2cm instead of expanding based on vasogenic edema can better spare the normal brain with the similar patterns of failure [78]. This suggests that dose escalation RT to smaller tumor volumes within the tumor target is feasible and beneficial [78]. In recent years, with the development of conformal radiation techniques, such as intensity modulated radiation therapy (IMRT) and volumetric modulated arc therapy (VMAT), they are able to deliver different dose levels to the target and better protect the normal tissue compared with 3D-CRT. Therefore, interest in employing IMRT and VMAT is growing to deliver boosted dose within tumors for GBM. Tables 2.5 and 2.6 reviewed publications in the past two decades, where partial dose escalation is used within tumor target for newly diagnosed GBM, to verify whether dose escalation can improve the treatment outcome compared to standard RT. In Tables 2.5 and 2.6, Gy/f is

Gy/fraction; EQD₂ is the equivalent dose; BED₁₀ is the biological equivalent dose in Gy, when assuming an α/β ratio of 10; 1yr OS is the 1-year overall survival rate (OS); 1yr PFS is the progression-free survival rate (PFS); MS represents median overall survival months; MPFS represents median progression-free survival months; 3D-CRT is 3 dimensional conformal radiation therapy; IMRT is intensity modulated radiation therapy; SIB is simultaneously integrated boost; and SRT is stereotactic radiation therapy.

Table 2.5 The survival rates and toxicities for newly diagnosed GBM when performing RT with standard dose levels.

Study	Prescription dose	EQD ₂	BED ₁₀	Chemo	1yr OS	1yr PFS	MS	MPFS	Toxicities	Technique
Roa <i>et al.</i> (2015) [20]	60Gy/30f	60.00	72.00	No	20.00%	6.00%	6.4	4.2	No > grade 2 acute toxicity	3D-CRT
Stupp <i>et al.</i> (2009) [79]	60Gy/30f	60.00	72.00	No	51.40%	\	11.8	\	\	3D-CRT
Perry <i>et al.</i> (2017) [80]	40.05Gy/15f	42.86	51.44	No	22.10%	1.10%	7.6	3.9	\	3D-CRT
Malmstrom <i>et al.</i> (2012) [21]	60Gy/30f	60.00	72.00	No	17.00%	\	6.0	\	1 fatal infection	Multiple field technique
Stupp <i>et al.</i> (2009) [79]	60Gy/30f	60.00	72.00	Yes	60.30%	\	12.6	\	Severe late grade 3/4 toxicities in 3 patients	3D-CRT
Perry <i>et al.</i> (2017) [80]	40.05Gy/15f	42.86	51.44	Yes	37.70%	15.70%	9.3	5.3	Higher rates of grade 3-4 hematologic toxicities than no chemo	3D-CRT

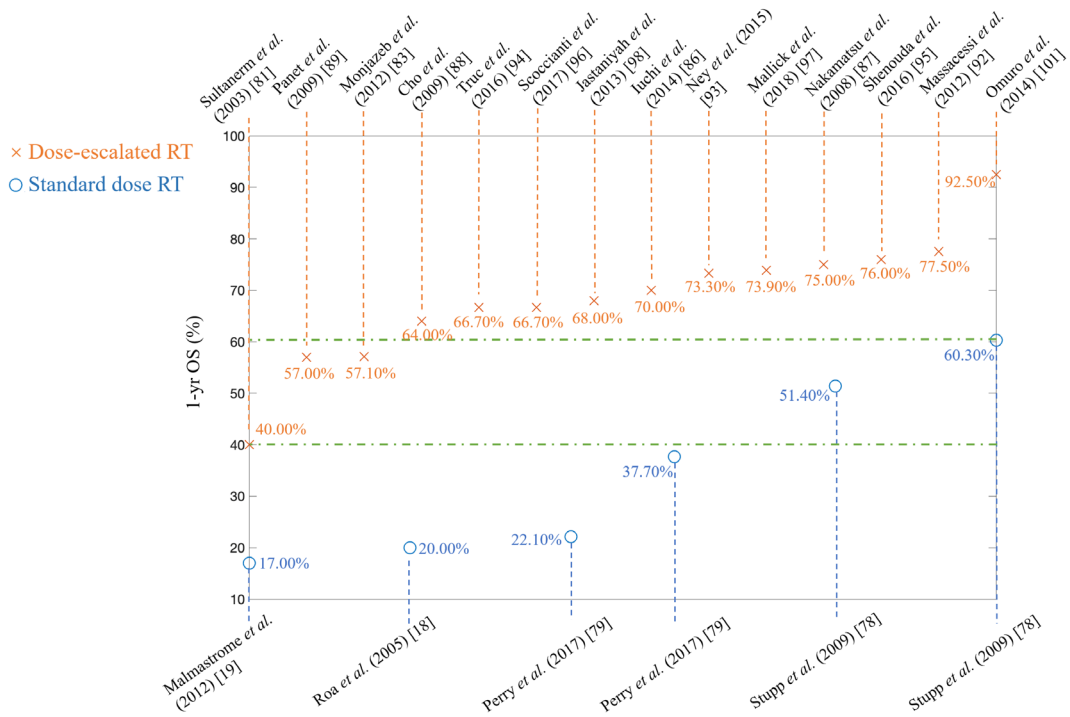
Table 2.6 The survival rates and toxicities for newly diagnosed GBM when performing dose-escalated RT.

Study	Prescription dose	EQD ₂	BED ₁₀	Chemo	1yr OS	1yr PFS	MS	MPFS	Toxicities	Tech.
Thilmann et al. (2001) [81]	75Gy/30f	78.13	93.75	No	\	\	\	\	\	
Sultanerm et al. (2003) [82]	60Gy/20f; 65Gy/25f	65.00;6 8.25	78.00; 81.90	No	40.00	\	9.5	5.2	No late toxicities observed	
Floyd et al. (2004) [83]	50Gy/10 f	62.50	75.00	No	\	\	7.0	6.0	3 patients with grade 3-4 toxicities (radionecrosis requiring resection)	
Monjazez et al. (2012) [84]	70, 75 and 80 Gy at 2.5Gy	72.92; 78.13; 83.33	87.50; 93.75; 100.00	No	57.10%	14.30%	13.6	6.5	8 patients with acute grade 3 toxicities, 1 with acute grade 4, 2 patients with late grade 3 toxicities, none with grade 4-5	
Chan et al. (2003) [85]	70Gy/33f	70.71	84.85	No	\	\	\	\	\	
Suzuki et al. (2003) [86]	70Gy/28f	72.92	87.50	Yes	\	\	7	5.4	One patient developed grade 3 radiation dermatitis	
Iuchi et al. (2014) [87]	68Gy/8f	104.83	125.80	Yes	70.00%	43.50%	24.0	14.0	No ≥ grade 3 toxicities noted	
Nakamatsu et al. (2008) [88]	70Gy/28f	72.92	87.50	Yes	75.00%	25.00%	16.5	8	No radiation-induced necrosis	SIB-IMRT
Cho et al. (2009) [89]	60Gy/25f	62.00	74.40	Yes	64.00%	42.00%	14.8	11.0	10% patients had grade 1 neurological toxicities	
Panet et al. (2009) [90]	60Gy/20f	65.00	78.00	Yes	57.00%	37.50%	14.4	7.7	1 patient had grade 3 or 4 toxicities of nausea and emesis were reported	
Reddy et al. (2011) [91]	60Gy/10f	80.00	96.00	Yes	\	\	16.6	\	No patient of grade 3 or higher nonhematologic toxicity	
Chen et al. (2011) [92]	60Gy/10f-20f	80.00;6 5.00	96.00; 78.00	Yes	\	\	16.2	\	3 patients with radionecrosis; 1 lost vision in left eye 7 months after RT	
Massaccesi et al. (2012) [93]	60, 62.5, 65, 67.5, and 70 Gy/25f	62.00; 65.10; 68.25; 71.44; 74.67	74.40; 78.13; 81.90; 85.73; 89.60	Yes	77.50%	43.60%	17.0	12.0	3/14 patients on 70 Gy/25 fraction dose level had a dose-limiting toxicity; No > grade 2 neurologic toxicities	
Ney et al. (2015) [94]	60 Gy/10f	80.00	96.00	Yes	73.30%	73.30%	16.3	14.3	Grade 3-4 nonhematologic toxicities of fatigue, wound dehiscence,	

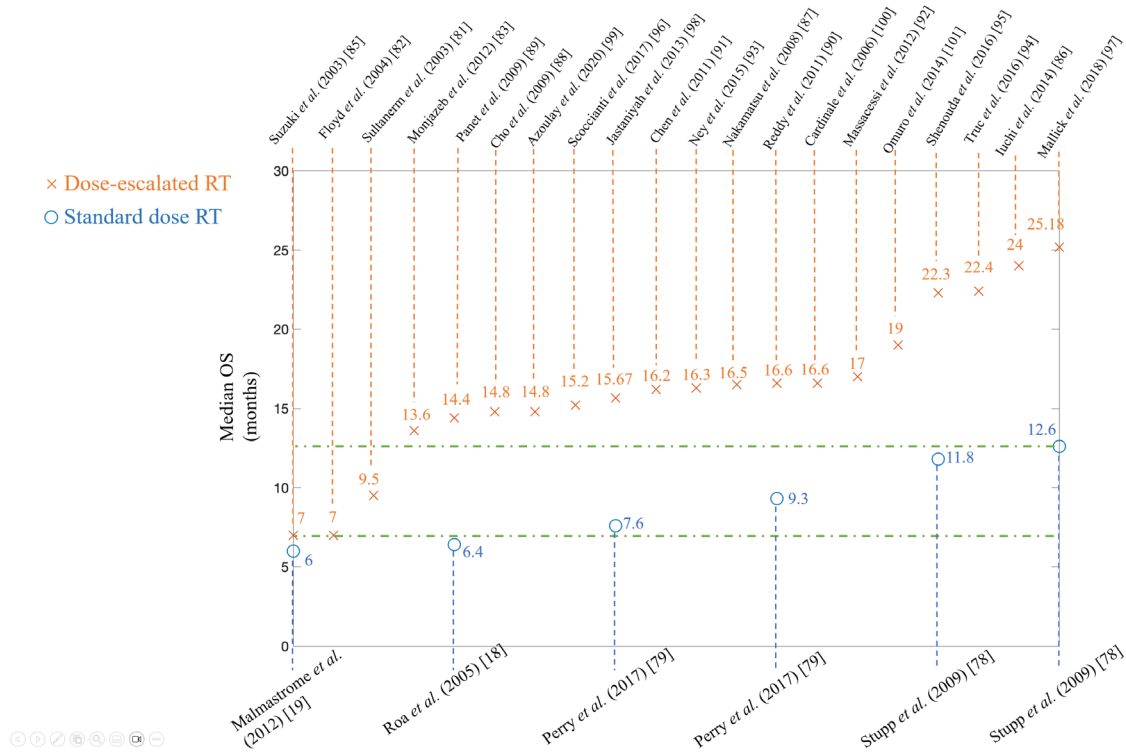
									stroke, pulmonary and embolism	
Gilles Truc et al. (2016) [95]	70Gy/28f; 75Gy/30f; 80Gy/32f	72.92; 78.13; 83.33	87.50; 93.75; 100.00	Yes	66.70%	\	22.4	\	No patients showed dose-limiting toxicity	
Shenouda et al. (2016) [96]	60 Gy/20f	65.00	78.00	Yes	76.00%	53%	22.3	13.7	Grade 5 pancytopenia in 1 patient	SIB-IMRT
Scoccianti et al. (2017) [97]	67.5 Gy/15f	81.56	97.88	Yes	66.70%	41.20%	15.2	8.6	3 patients with grade 3 myelotoxicity, 1 patient with radionecrosis requiring resection	
Mallick et al. (2018) [98]	60 Gy/20f	65.00	78.00	Yes	73.90%	63.70%	25.18	13.5	1 patient of radionecrosis; 4 patients of grade 3-4 thrombocytopenia	
Jastaniyah et al. (2013) [99]	54.4Gy/20f ; 60Gy/22f	57.66; 63.64	69.20; 76.36	Yes	68%	38%	15.67	6.7	Grade 3-4 hematologic toxicity in 2 patients	IMRT (helical tomotherapy)
Azoulay et al. (2020) [100]	25, 30, 35, and 40Gy/5f	31.25; 40.00; 49.58; 60.00	37.50; 48.00; 59.50; 72.00	Yes	60.50%	\	14.8	8.2	Dose-limiting toxicity defined as Grade acute or late neurologic 3-5 toxicity; no adverse radiation related grade 3-5 toxicities occurred	SRT
Cardinale et al. (2006) [101]	50Gy/25f + 20-28Gy/4f	75.00; 89.67	90.00; 107.60	Yes	\	\	16.6	\	3 acute grade 4 toxicities secondary to RT	3DCRT+SRT
Omuro, et al. (2014) [102]	36Gy/6f	48.00	57.60	Yes	92.50%	28%	19.0	6.5	50% patients have hematologic toxicities	SRT

In Tables 2.5 and 2.6, the majority of studies have the median follow-up time longer than 1 year. In Table 2.5, 1282 patients across 6 studies were performed by treatment with standard dose levels, *i.e.*, 60Gy in 30 fractions for patients younger than 70 years old and $KPS \geq 70$, or 40.5Gy in 15 fractions for patients older than 70 years old and $KPS \leq 70$. Of these, 4 studies were treated without chemotherapy. Their median 1-year overall survival (OS) are in the range of 8.50% to 51.40%. Median OS months are in the range of 5.1 to 11.8 months. The remaining 2 studies were treated with chemotherapy of TMZ and their median OS are in the range of 37.70% to 60.30%. Median OS months are in the

range of 9.3 to 12.6 months. In Table 2.6, five studies include 97 patients focusing on dose escalation RT without chemotherapy. Their EQD₂ are in the range of 62.50Gy to 78.13Gy. One-year OS are in the range of 40.00% to 57.10% and the median OS are in the range of 7.0 to 13.6 months. 610 patients across 18 studies were treated with dose escalation RT plus chemotherapy. Their EQD₂ are in the range of 62.00Gy to 81.56Gy. One-year OS rates are in the range of 56.00% to 92.50% and the median OS rates are in the range of 12.4 to 24.0 months. Figures 2.4(a) and 2.4(b) show the one-year overall survival and median overall survival months of studies listed in Tables 2.5 and 2.6, using standard RT and dose escalated RT.



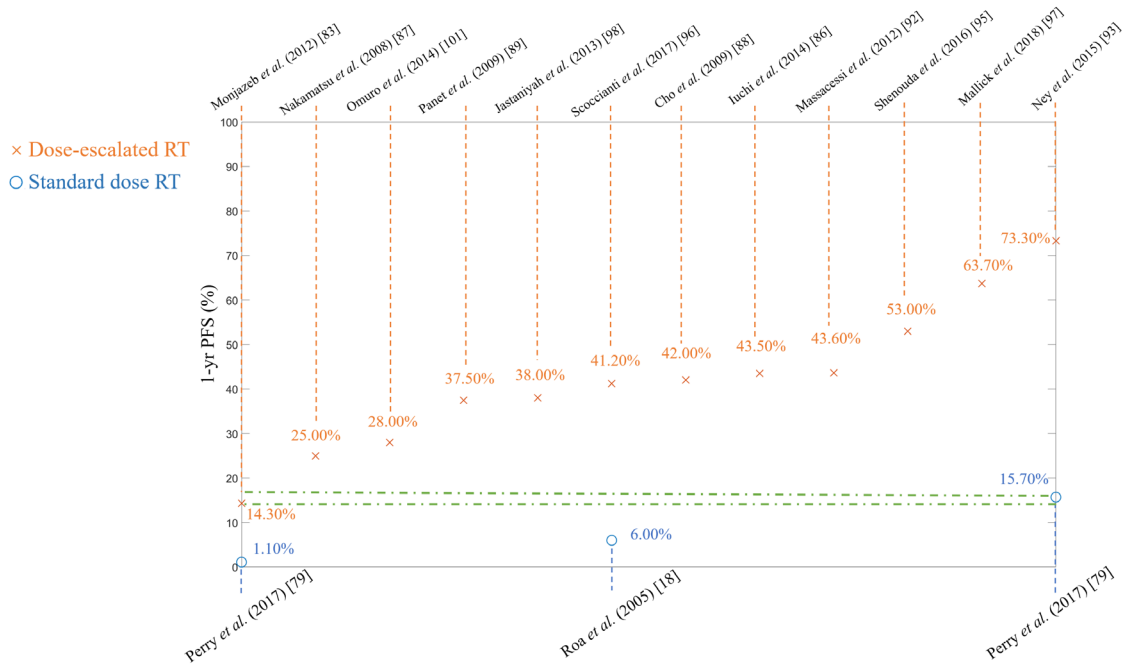
(a) One-year overall survival (OS) rates with standard-dose and dose-escalated RT.



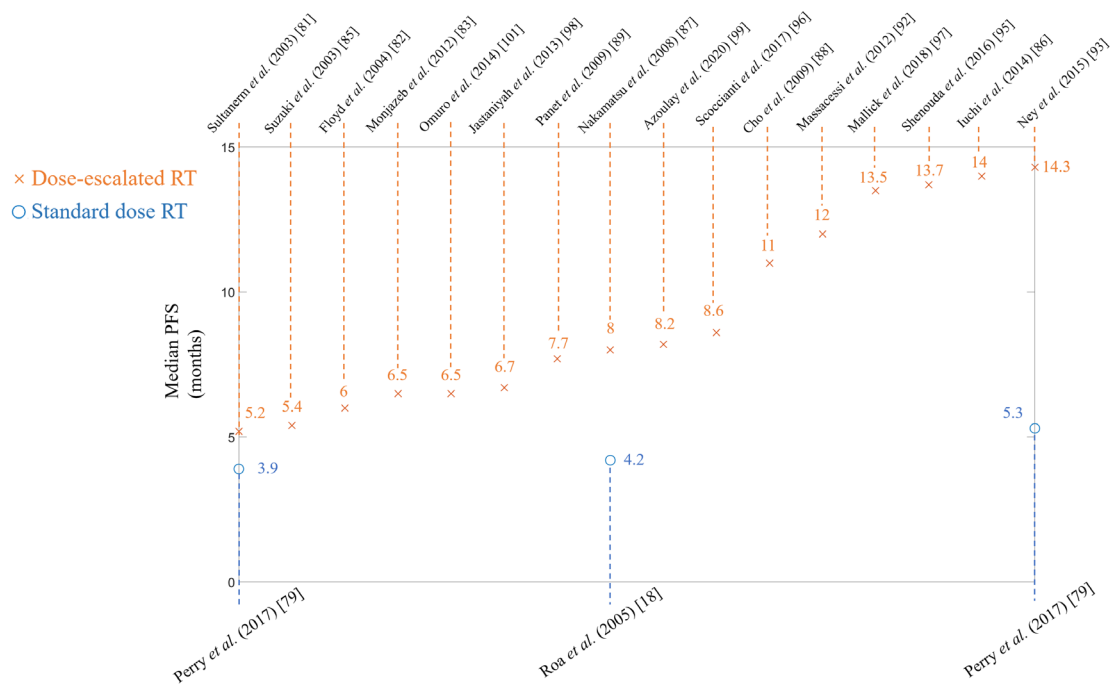
(b) Median OS months with standard-dose and dose-escalated RT.

Figure 2.4 One-year OS rates and median OS months in studies with standard-dose and dose-escalated RT.

Progression-free survival (PFS), in addition to overall survival, is another metric used to assess clinical studies. However, there are only 3 standard RT research provided 1-year PFS (shown in Table 2.5). Perry *et al.* evaluated the 1-year PFS for patients treated by standard RT without and with chemotherapy. For patients treated without chemotherapy, the result was only 1.1% of 1-year PFS. The median PFS was 3.9 months. For patients treated with chemotherapy, 1-year PFS and median PFS are 15.7% and 5.3 months, respectively. In Table 2.6, patients in the first 5 studies (rows 1-5) treated without chemotherapy have 1-year PFS of 14.3% and median PFS ranging from 5.2 to 6.5 months. The rest of studies in Table 2.6 are treated using dose-escalated RT with chemotherapy. The 1-year PFS is from 28% to 73.3% and the median PFS is from 6.5 to 14.3 months.



(a) One-year progression-free survival (PFS) rates of standard-dose and dose-escalated RT.



(b) Median PFS months of standard-dose and dose-escalated RT.

Figure 2.5 One-year PFS rates and median PFS months in studies of standard-dose and dose-escalated RT.

Figures 2.5(a) and 2.5(b) show the one-year progression-free survival (PFS) rates and median PFS months in patients of studies listed in Tables 2.5 and 2.6, using standard RT and dose escalated RT.

Cardinale *et al.* started the first modern multi-institutional prospective study examining the potential benefit of dose-escalated RT specifically for GBM patients, which were originally registered as the phase 2 Radiation Therapy Oncology Group 0023 trial [101]. After resection, 76 patients initially received conventionally fractionated RT of 50 Gy/25 fractions followed by a stereotactic boost of 20 to 28Gy/4 fractions, the total doses ranging from 70 to 78Gy followed by chemotherapy of adjuvant carmustine. Median OS was 16.6 months. Notably, the dose-escalated RT was well tolerated, with roughly 4% and 1% of patients experiencing acute and late grade 3 or greater RT-related toxicities, respectively. After this study, a number of prospective phase 1 and 2 trials were conducted. Given advancements in both diagnostic imaging as well as the conformality of RT delivery methods, there has been growing interest in the use of dose-escalated RT to improve outcomes over standard of care management. After a systematic review of these studies, significant PFS and OS increases have been achieved in dose-escalated RT compared to standard RT with or without chemotherapy.

It is worth noting that, in Table 2.6, the majority dose-escalated RT used the technique of simultaneously integrated boost (SIB) IMRT. The boosted doses were delivered to the high-risk areas within the tumor target. Most of the studies in Table 2.6 defined the high-risk areas as GTV plus 5mm margin. Such definition of high-risk areas has been commonly used clinically. With the development of the radiography, some studies employed the quantitative imaging, such as positron emission topography (PET) to define

the high-risk areas, as are shown in Table 2.7. Douglas *et al.* developed a functional imaging-based dose-escalated RT for 40 GBM patients using PET [103]. They delivered 79.4Gy to the PET abnormal areas. There were no incidences of grade 3 or greater toxicities. The median OS was 70 weeks. Piroth *et al.* conducted a study of 22 patients with GBM using PET-FET (fluoroethyl-L-tyrosine) to escalate dose to 72Gy/30 fractions to residual disease defined by FET-avidity. The median OS was 14.8 months without incidences of grade 3 or greater toxicities and no incidences of radionecrosis existed [104]. Tsien *et al.* alternatively used pretreatment MRI-PET to identify potential areas of failure, with dose-escalated RT cumulative doses of 66 to 81 Gy [105]. No patients received less than 75Gy experienced radionecrosis, with approximately 20% to 40% of patients experiencing dose-limiting toxicities at dose escalation RT cumulative doses of 75 Gy or greater. In 2013, Ken *et al.* proposed a design of Phase III trial using magnetic resonance spectrum imaging (MRSI) to define the high-risk areas [106]. In their study, dose-boosted area was defined as MRSI abnormalities plus 10mm with 72Gy in 30 fractions. Laprie *et al.* conducted the Phase III clinical trial across multicenter based on Ken *et al.*'s design, and found that dose increases were well tolerated and grade 1-2 neurological deficit were observed in the patients' cohort. After a median follow-up of 43.7 months, OS and PFS were 22.2 months and 7.8 months, respectively [107].

Kosztyla *et al.*[108] used the thresholds of ¹⁸F-DOPA uptake to define 7 high-risk areas. Each of them was delivered with 62.5,65, 67.5, 70, 72.5, 75, and 77.5Gy in 30 fractions. The dosimetry analysis proved that dose escalation with ¹⁸F-DOPA PET-defined high-risk area was feasible using commercially available TPS without increasing the dose delivered to cranial OARs. This technique would offer better disease control than conventional radiotherapy for high-grade gliomas.

Table 2.7 The overview of using quantitative imaging for dose-escalated RT for newly diagnosed GBM.

Study	High-risk target	PTV	Dose to high-risk area	Dose to PTV	1yr OS	1yr PFS	MS	MPFS	Toxicities
Douglas <i>et al.</i> (2005) [103]	PET-directed	GTV+15mm; GTV+20-30mm	79.4Gy	59.4Gy; 50.4Gy	70%	18%	16.2	5.5	All toxicities were grade 2 or less.
Piroth <i>et al.</i> (2012) [104]	PET-directed	MRI-directed	72Gy/30f	60Gy/30f	63.6%	25.4%	14.8	7.8	No grade 3-4 toxicities and no incidences of radionecrosis.
Tsien <i>et al.</i> (2012) [105]	MRI-PET abnormalities + 5mm	GTV+20mm	66-81Gy/30f	60Gy/30f	73.7%	33.8%	20.1	9.0	Late CNS > grade 2 toxicity at 78 Gy (2/7 patients) and 81 Gy (1/9 patients); 0/22 receiving <75 Gy experienced radionecrosis. Dose-limiting toxicities: 2/9 at 75 Gy, 3/7 at 78 Gy, and 2/9 at 81 Gy.
Kosztyla <i>et al.</i> (2018) [108]	Thresholds of 18F-FDOPA uptake	Contrast-enhancing tumor on T1 weighted MRI+ 25mm	62.5,65, 67.5, 70, 72.5, 75, and 77.5Gy/30f	60Gy/30f	\	\	\	\	\
Laprie <i>et al.</i> (2019) [107]	GTV2(Cho/NAA>2 on MRS) +7mm+GT V1+3mm	GTV1 (contrast enhancement) +20mm	72Gy/30f	60Gy/30f	\	\	22.2	7.8	Grade 1-2 neurological deficit

2.2.3 Diffusion-weighted MRI

As described in the end of Section 2.2.2, there are researchers starting using quantitative imaging to implement dose-escalated RT in recent years. Medical imaging is crucial for outcome management and treatment planning to ensure that patients after RT receive satisfying treatment [109]. The size and location of tumors can be assessed using

conventional anatomical imaging techniques, such as CT and MRI. However, conventional anatomical imaging techniques only offer a limited amount of information about the macro- and micro-environments of tumors, particularly when it comes to biological functions, such as metabolism, cell proliferation, perfusion, hypoxia, *etc.* Such tissue function and biological condition can be accessed by utilising biomarkers embedded in quantitative imaging. The severity of the disease can be evaluated accurately and target volumes can be more precisely depicted via quantitative imaging in treatment planning [110]. Moreover, quantitative imaging can be used for monitoring treatment effects and selecting treatment regimens [111]. Last but not the least, quantitative imaging can be used for dose optimization and dose mapping. According to the quantitative parameter maps, the prescription dose can be spatially re-assigned throughout the tumor volume [109],[112]. As a result, there has recently been an increase in interest in obtaining radiologic biomarkers using quantitative imaging [113]. For instance, critical-tissue and neural-nerve functions are protected during RT using quantitative imaging [113].

The most common approaches of quantitative imaging in radiotherapy are diffusion-weighted magnetic resonance imaging (DW-MRI), MR-Spectroscopic (MRS), Perfusion MRI including dynamic susceptibility contrast (DSC) and dynamic contrast enhanced (DCE), diffusion tensor imaging (DTI) MRI and positron emission tomography (PET)-CT. Among them, DW-MRI allows us to assess in vivo cell density of organs and tissues inside the body [127],[128]. Since tumor cell density is regarded as a significant component that affects the treatment outcome [129-131], DW-MRI is chosen as the quantitative imaging in this thesis. The cellular density, growth rate and permeability can be measured with great accuracy using DW-MRI [114], [115]. DW-MRI can also present microscopic features of healthy and abnormal tissues. The number of diffusion weights,

i.e., b -value, models the sensitised signal [116], [117]. The apparent diffusion coefficients (ADC) indicate how much diffusion is present in the tissue, mostly in the extracellular space [118].

DW-MRI provides image contrast through the measurement of water molecules movement within tissues [119]. It is based on the principle of diffusion, which is the random movement of molecules. In DW-MRI, the movement of water molecules is probed and measured to generate images that reflect the underlying tissue properties. The utilization of diffusion sensitizing gradients in the MR pulse sequence enables the detection of water molecule displacement within a range of 1-20 μm [119]. In order to associate MR signals with motion, there are two magnetic field gradients incorporated in the pulse sequence [119]. The first gradient pulse modifies the phase shift of each proton, which is determined by the spatial position of water molecules relative to the gradient. If the water molecules do not move during the time between the first and second gradient pulses, the second gradient pulse (with the same strength but opposite direction to the first gradient pulse) will reverse this phase shift. However, if water molecules move between the two gradient pulses, the phase shift will not be entirely reversed, resulting in the loss of signal from that spatial position. Le Bihan *et al.* proposed using the “ b factor” to represent all the gradient terms [120]. The sensitivity of diffusion in a DW-MRI sequence characterised by its b -value, can be modified by adjusting the gradient pulse amplitude, the duration for which the gradients are applied, and the diffusion time [119]. In DW-MRI, the higher the b factor, the more sensitive an image is to the diffusion. A diffusion-weighted image can be affected by other MR properties, *e.g.*, T1 and T2 relaxivity contrast. To remove all effects other than that of diffusion, ADC is used, which can be

estimated with the monoexponential model by acquiring MR signals at least twice, typically with (S_b) and without (S_0) diffusion weighting

$$ADC(x, y, z) = \frac{1}{b} \ln \left(\frac{S_0}{S_b} \right). \quad (2.20)$$

An ADC map can be also created following this way by combining two images with two b -values. More images at various b -values can provide a more accurate estimation. Beyond simple ADC calculations, DW-MRI can reflect microvascular perfusion [121], [122]. Le Bihan *et al.* [121] proposed the intravoxel incoherent motion (IVIM) model to separate the diffusion of water molecules to microcapillary perfusion of tissues as low b -values are sensitive to perfusion. Therefore, perfusion-related parameters, such as perfusion fraction and pseudo-diffusion coefficients associated with microcapillary blood flow, can be estimated.

Lower ADC readings imply a slower rate of water infusion if malignant tumors are present and vice versa [123]. As a result, there is an inverse relation between ADC and cellular density. Several studies explored the relationship between ADC and cellular density for different tumor locations. Gupta *et al.* predicted the relationship for GBM [124]. Koh and Collins introduced DW-MRI in cancer in their article [125], while Tsien *et al.* and Leibfarth *et al.* provided reviews of DW-MRI application for radiotherapy [126], [127]. Gurney *et al.* advised readers to adhere to rules, such as those provided by the Quantitative Imaging Biomarkers Alliance (QIBA), when applying DW-MRI [109].

Both Hamstra *et al.* [128] and Moffat *et al.* [129] offered information that was used for tailoring radiation to the specific needs of individual patients. Patients whose ADC values

drastically increased after three weeks of radiation often have a greater overall survival (OS) [128], [129]. The tumor control probability (TCP) may be determined with the use of ADC, which can then be utilized to analyze patient-specific features. MRI-driven cellular density was shown in the recent research to be able to augment TCP value differences in patients [130]. DW-MRI was examined by Buizza *et al.* for the purpose of modelling TCP in skull-base chordomas [131]. The aforementioned techniques make it possible to provide individualized treatments with dose optimization. However, to the best of my knowledge, we are the first study using DW-MRI for the treatment of newly diagnosed GBM. Compared to the PET-CT and MRS imaging, DW-MRI allows us to assess in vivo information of heterogeneous cell density for tumors [132], [133]. Since tumor cell density is regarded as a significant component that affects the treatment outcome [134]–[136]. I choose to use DW-MRI as the functional imaging in this thesis, as will be discussed in Chapters 4 and 5.

2.2.4 Dose Painting

In comparison to surgery or chemotherapy alone, RT technology is still a standard treatment for malignant tumors and has advanced quickly over the past few decades. Modern imaging techniques such as CT and MRI have significantly contributed to the advancement of radiotherapy in recent decades. Conventional GBM tumor targets such as gross tumor volume (GTV) and clinical target volume (CTV) were defined in Radiation Therapy Oncology Group (RTOG) [137] or European Organization for Research and Treatment of Cancer (EORTC) [138] protocols. As a standard practice in radiotherapy, homogeneous radiation doses are delivered to the target area. However, local recurrence after RT is one of the important modes of failure according to Table 2.4. The main reason

would be that the tumor's planning target volume (PTV) is given a homogeneous prescribed dose without taking into account the tumor's heterogeneity in terms of microbiology, time and space. To solve this problem, dose painting was first suggested at European Society Radiation Oncology (ESTRO) conference in 1998 [139]. Ling *et al.* used biological imaging in the 2000s to accomplish "biological conformality", where higher doses are administered to specific sections of a tumor that have higher progression risk and radiation resistance, while lower doses are applied to less aggressive regions [139]. Tumor cells can be eliminated in this manner, and healthy tissues can be recovered more quickly [140], [141]. Recently, a number of quantitative imaging optimizations have been proposed to increase the accuracy of dose painting since many factors, such as hypoxic area, cell proliferation rate, tumor cell density and intratumor blood perfusion, affect the sensitivity of radiotherapy in the tumor [113], [121]. Quantitative images have the potential to strengthen prognostication response to RT, facilitating personalized treatment and clinical trial designs in terms of patient-specific prescription dose and biological target volume (BTV) [142], [143]. Furthermore, heterogeneous dose painting using quantitative functional imaging allows for the spatial redistribution of doses within the target tumor via personalized parameter maps [109].

Considering the biological heterogeneity in tumors, performing supplemental irradiation for the volumes that are comparatively resistant to treatment, it is possible to enhance local control. Given the discussions in Section 2.2.3, the creation of dose painting can be facilitated by modern biological imaging techniques, such as PET-CT and multiparameter MRI [144]. This new radiation technique can provide an optimised non-uniform dose distribution for the treatment of tumors [144]. With respect to three-dimensional (3D) radiobiological analysis, dose painting can also be used to investigate

relationships among important radiotherapy parameters, the inherent ability to identify the relevant target volume, and the therapeutic dose to control the disease. As shown in Table 2.7, at present, quantitative imaging-based dose painting is mostly implemented through PET-CT or MRS imaging technologies.

Recently, dose escalation and dose redistribution have been proposed as a way to provide a more resistant portion of the tumor with a relatively higher dose. There are two primary methods of dose painting: 1) dose painting by contours (DPBC) and 2) dose painting by numbers (DPBN). In DPBC, a tumor's sub-volumes are heterogeneous in the functional images needed to be treated in a differentiated dose level [145]. As for DPBN, each voxel of a tumor receives a prescribed dose in DPBN based on the voxel value in functional images. A dosage-prescription map often depicts such voxel-based dose distributions [145].

The first DPBC approach was proposed by Ling *et al.* in 2005 [146]. A subvolume of the tumor receives a dose boost by a predetermined threshold owing to DPBC techniques. The threshold from the quantitative functional imaging is used to fix the regions with comparatively lower and higher risk for recurrence. When converting an image into a prescription function for dose painting, there exist uncertainties related to imaging modalities [147], [148]. Some major uncertainties, *e.g.*, tumor deformable image registration (DIR) has been investigated by Chen *et al.* [149].

The simultaneous integrated boost (SIB) technique [106], which increases the dose at a subvolume of the tumor, is a popular treatment planning method for DPBC. Better dose tolerance is expected for patients who receive this treatment compared with increasing

the dose to the whole tumor target [150]. There are several clinical studies explored DPBC [151]. PET-based DPBC was used to assess the feasibility of intensity-modulated radiotherapy (IMRT), where the maximum tolerated dose in head and neck cancer can be determined [152]. Treatments for non-small-cell lung cancer (NSCLC) are also being investigated for the similar purpose of raising acceptable doses [153]. Fleckenstein *et al.* proposed a source- to-background contouring algorithm for FDG-PET in the process of RT planning [153]. Kong *et al.* showed that modifying RT by increasing dose via DPBC to the FDG avid region increases the 2-year local-regional tumor control and the overall survival rate [154].

Dose painting by numbers refers to prescribing doses in a voxel-by-voxel manner [142]. The local voxel intensities are used to alter the DPBN technique, which gradually increases the additional dose. The relationship between the voxel values of the functional imaging and the risk of local recurrence is normally characterized using mathematical models [155]. Chen *et al.* [149] analysed how the uncertainties in quantitative FDG-PET CT imaging impact intratumorally dose–response quantification, including those caused by PVE and tumor DIR [149]. By using DPBN approaches, some of these uncertainty-detrimental effects might be minimised [149].

Many technical feasibility and robustness of DPBN studies have been published recently [156]–[158]. Dose prescription with steep gradients can be delivered by numerous subvolumes via a conventional linear accelerator [159]. Additionally, Berwouts *et al.* demonstrated the feasibility of [¹⁸F]-FDG-PET-guided DPBN in a phase I clinical trial for head and neck RT [160]. Grönlund *et al.* investigated the spatial relation between retrospectively observed recurrence volumes and pre-treatment standardized uptake

values (SUV) from FDG-PET [155]. SUV driven dose–response functions have been presented to optimize ideal dose redistributions under the constraint of equal average dose of a tumor volume [155]. DPBN approaches using subvolumes as targets [155], [161], [162] or dose maps with prescription to the voxel as objective function [163], belong to dose-volume based optimization algorithms. Jiménez-Ortega *et al.* presented a new optimization algorithm to implement directly constraints to voxels instead of volumes [145]. This method is implemented in CARMEN, a Monte Carlo (MC) treatment planning system [145].

DPBC mainly refers to the specific function image parameters to set the threshold for the replenishment area. Generally, biomarkers in the high-risk area for recurrence have larger values over the defined threshold, while low-risk recurrence area corresponds to biomarkers having smaller values than the threshold. Advantages of DPBC are that sub-volumes that need to boost dose can be pre-drawn before the treatment plan. Then the sub-volumes can be set to add margins to supplement the geometric uncertainty, and the treatment plan can also be evaluated by conventional DVH. DPBC usually lacks the consensus of the threshold for biomarkers. DPBN assumes that the recurrence risk of a certain pixel in the tumor area is positively correlated with the parameter intensity of its specific function image pixel, and the radiation dose of a certain pixel is directly related to its corresponding functional image pixel information. DPBN has more theoretical advantages than DPBC because it can deliver doses to voxel level. However, it cannot extend the margin of specific voxels and is more sensitive to uncertainty arising in image registration. Therefore, online image-guided treatment is required to clearly show soft tissues. Furthermore, DPBN requires a customized software package to optimize the

irradiation plan, but there is no commercial software directly implementing the optimization of DPBN [164], [165].

2.3 Preliminaries of Proton Therapy Treatment

Photons are electrically neutral and interact with matter in a random way, and do not lose energy when they pass through matter; instead, they travel until they are absorbed or dispersed (*i.e.*, changing direction of travel, with or without loss of energy). As a result, photons do not have a finite penetration depth [1]. When a proton travels through matter, it loses energy largely through ionising and activating the medium's atoms. As shown in Table 2.7, protons interact with matter in three distinct ways. Firstly, protons can slow down by myriad collisions with atomic electrons, called stopping interaction. Secondly, protons are deflected by myriad collisions with atomic nuclei, called scattering interaction. Lastly, protons sometimes have a head-on collision with a nucleus, setting secondary particles in motion, called nuclear interactions [1] [2].

In a single collision with an atomic electron, a heavy charged particle can only transmit a small proportion of its energy, and the deflection is insignificant. As a result, a proton travels practically straight through matter, losing energy in tiny amounts continually. The mass and energy of protons are higher versus photons, therefore proton has less side scatter. After entering human tissue, the proton beam will produce a sharply rising dose at a specific depth, called the Bragg Peak [1]. Before the formation of the Bragg peak, there exists a lower dose flat section. After the Bragg peak, protons react and stop moving so that the energy drops to zero. Due to the finite propagation of protons in tissues, proton

therapy can deliver a much less dose to the healthy tissues around the tumor [166]. Adjusting the energy of the proton beam and superposing the different proton beams can extend the width of the Bragg peak over the dose distribution, which can exactly match the width of the tumor in the direction of the beam with the high dose area [167], guaranteeing the dose beyond the tumor on the direction of the beam is almost zero.

Table 2.8 Proton interactions with matter [1], [2].

Interaction type	Interaction target	Interaction mechanism	Effect
Stopping	Atomic electrons	Protons slow down by myriad collisions with atomic electrons via inelastic coulombic interactions	Energy loss indicates the depth where protons come to rest
Scattering	Atomic nuclei	Protons are deflected by myriad collisions with atomic nuclei via elastic coulomb scattering	Determine lateral penumbral sharpness
Nuclear interactions	Atomic nuclei	Protons have a head-on collision with a nucleus via non-elastic nuclear interaction, setting secondary particles in motion	Generation of neutrons, prompt gammas for in vivo interrogation

Proton radiation therapy uses a proton beam from a synchrocyclotron/cyclotron to pass through the body to the tumor tissue [168]. It releases a large amount of energy and kills the tumor cells for therapeutic purposes. The use of proton beams for radiation therapy leads to a better dose distribution, which can effectively increase the cancer tissue dose and reduce the normal tissue dose as much as possible [169]. Compared to photon and

electron radiotherapy, the advantages of proton radiotherapy are mainly reflected on the unique physical properties of protons, including the shape and finite range of the depth-dose distribution [1].

Figure 2.6 compares the variation of percentage depth dose curve (PDD) for both X-ray and Proton therapy beams [170], which demonstrates that the dose can be primarily delivered to the tumor. This results in the tumor cells being destroyed with only minimal effect on healthy organs nearby. Compared to other existing and developing radiotherapy approaches, proton therapy has been clinically proven to achieve fewer side effects for brain and pediatric tumors particularly. The advantages of proton therapy in the clinical application are as follows:

- The doses to the normal organs and tissues behind and around the tumor are almost zero, which greatly simplifies the angle design of the intensity modulated proton therapy plan.
- The normal organs and tissues in front of the target area at the irradiation direction receive a reduced irradiation dose, and normal tissues within the PTV receive similar doses to photon treatments. Compared with photon radiotherapy, proton radiotherapy can increase the dose of the target area while selecting more irradiation angles.
- When using intensity-modulated proton therapy technology, the dose is more evenly distributed in complex shape target regions. This also ensures that the normal organs and tissues around the tumor are subjected to a smaller dose.
- The number of irradiation fields required for protons are much less than those for photons or electrons, usually the proton RT has 3-5 radiation fields, smaller than

the 5-9 radiation fields for photon's [171]. Smaller number of irradiation fields can greatly reduce the radiation dosage for surrounding normal organs and tissues compared to the use of photons and electrons for the intensity modulated radiation therapy plan.

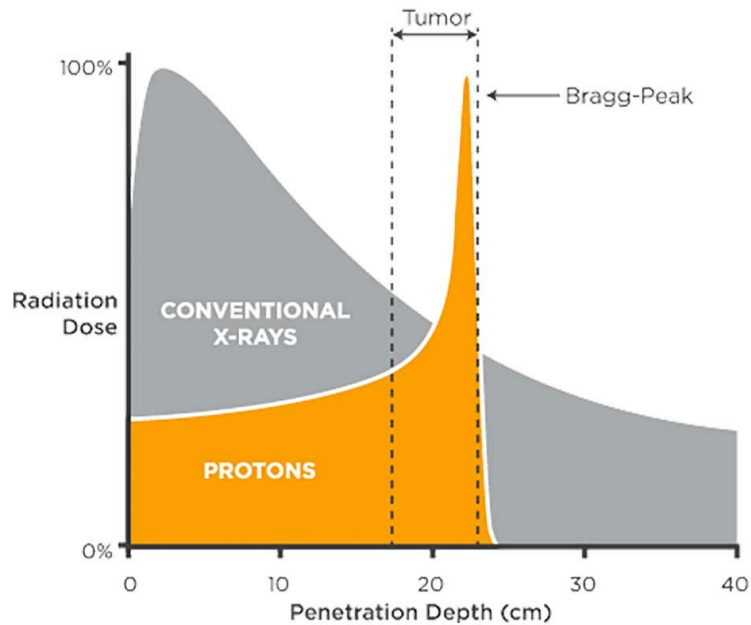


Figure 2.6 PDD of X-ray and Proton beams [157].

The application of protons to radiation therapy was proposed in 1946 [172]. The clinical research of proton radiation therapy was carried out successively at UpPsala University (1957), Harvard Cyclotron Laboratory (1961), and the former Soviet Union Gachina Institute (1968-1975). In 1991, the first particle acceleration device for medical treatment was manufactured in Loma Linda, California, USA. This device is suitable for tumor irradiation in different parts with reduced volume and cost. It is symbolic that proton radiotherapy has entered the field of clinical medicine. In recent years, proton

radiotherapy has been rapidly applied all over the world. According to the latest report of the International Particle Therapy Co-Operative Group (PTCOG) [173], there are already 111 proton centers currently working on proton therapy, including 4 NHS and 2 private proton centers in UK. There are additional over 100 proton centers under construction and in planning stage [173]. In particular, University College London Hospital (UCLH) is one of the largest proton centers in the UK which has been clinically used. Therefore, advanced proton RT technologies and treatment planning techniques are urgently needed. Due to proton therapy delivering radiation with pinpoint accuracy, with little or no dose to tissues beyond the tumor, fewer side effects are led to patients. In certain cases, proton RT leads to less chance of recurrence thanks to the opportunity to deliver higher tumor doses. Even though the proton center cost \$20 million to \$150 million for single- and multi-room facilities [174], proton RT is still a promising advanced technique for cancer treatment.

Many studies have explored the effectiveness and safety of proton therapy for tumors of head and neck cancer, brain cancer, lung cancer, esophageal cancer and liver cancer [5], [55], [58]–[60]. Clinical studies of multiple contrast photons and proton therapy for tumors are in progress. The results of these studies will rationally promote proton heavy ion radiotherapy, leading to a better understanding of the characteristics and advantages of protons therapy.

As mentioned above, since there is little exit dosage beyond the proton Bragg peak, proton can provide reduced integral doses to patients. If the tumor is projected under the Bragg peak, there will be little dose deposited beyond the tumor and delivered to surrounding OARs and healthy tissues. However, a spotless Bragg peak cannot be employed in the

clinical cancer treatment because it is too narrow to the usual size of tumor. Therefore, to evenly irradiate the tumor target, different energies of proton beams are combined to generate a spread-out Bragg peak (SOBP) [167], as shown in Figure 2.7. Even through the energy from a cyclotron is fixed, with the range modulator wheel, different energies are generated.

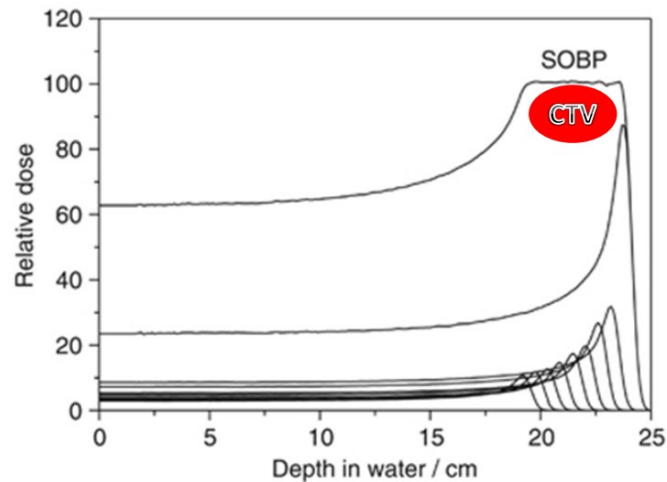


Figure 2.7 An illustration of spread-out Bragg peak (SOBP) [156].

There are two mechanisms, scattering system and pencil beam scanning system, in the proton synchrotrons/cyclotrons gantries to create a SOBP with the required beam width and shape to match the tumor volume. Figure 2.8 shows a schematic of these two proton delivery technologies. Scattering system is also called as double scattering system or passive scattering system. In a scattering system, firstly, the beam is spread out at the depth direction by a series of pristine Bragg peaks at different energies. Then, the beam is spread at the lateral direction by scattering foils. Now there exists the board beam which covers the tumor at 3 dimensions but does not conform the shape of the tumor. Finally, the collimator and the compensator are manufactured per patient per beam to shield the redundant beams and to suit the tumor shape. Scattering system is a relatively

conventional radiotherapy. What clinical treatment usually used is pencil beam scanning system. Rather than spreading out the beam in energy and geometrically, a pristine proton beam is steered by two pairs of scanning magnets to scan the tumor shape at the certain depth of layer. Different depth of layers is scanned using different energies till the entire tumor has been scanned across in any sort of position and combination of intensities. Proton radiotherapy typically utilizes protons with energies ranging from 70 MeV to 250 MeV. In our patients cohort, the energies used for each field are around 90-184 MeV.

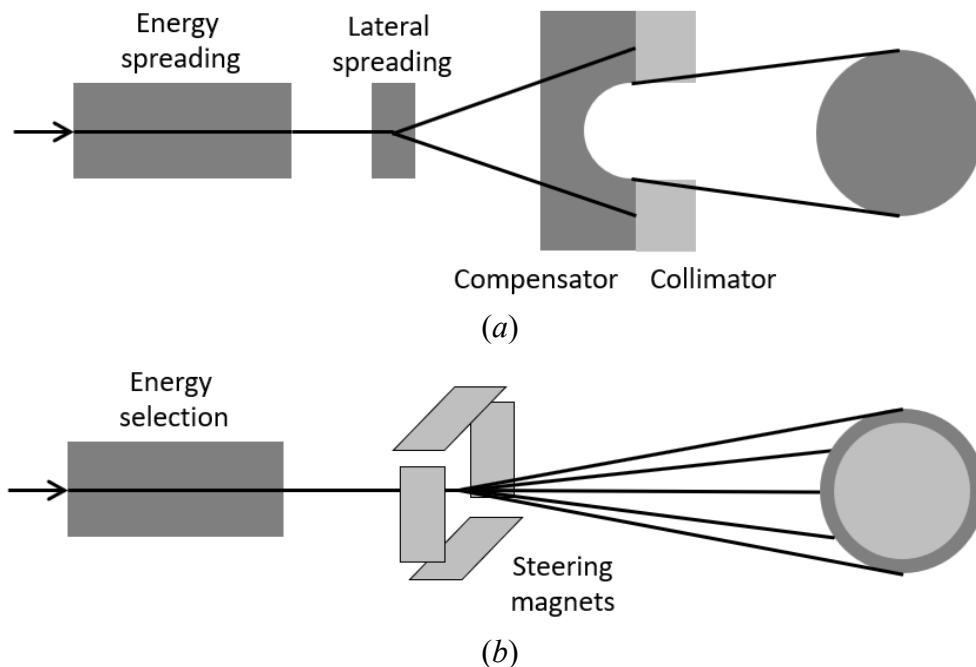


Figure 2.8 A schematic of scattering system (a) and pencil beam scanning (PBS) system (b).

As a pristine proton beam scanning across the tumor, the spot size of a pristine proton beam is just in the level of millimetres, even though it contains millions of protons. In the clinical use, these spots' weights are modulated and arranged to match the size and the shape of tumor. Figure 2.9 is a patient case in the proton treatment plan system for the spot weights at a single layer. On the same layer, all of the spots have the same energy. The greyscale value denotes their relative weighting.

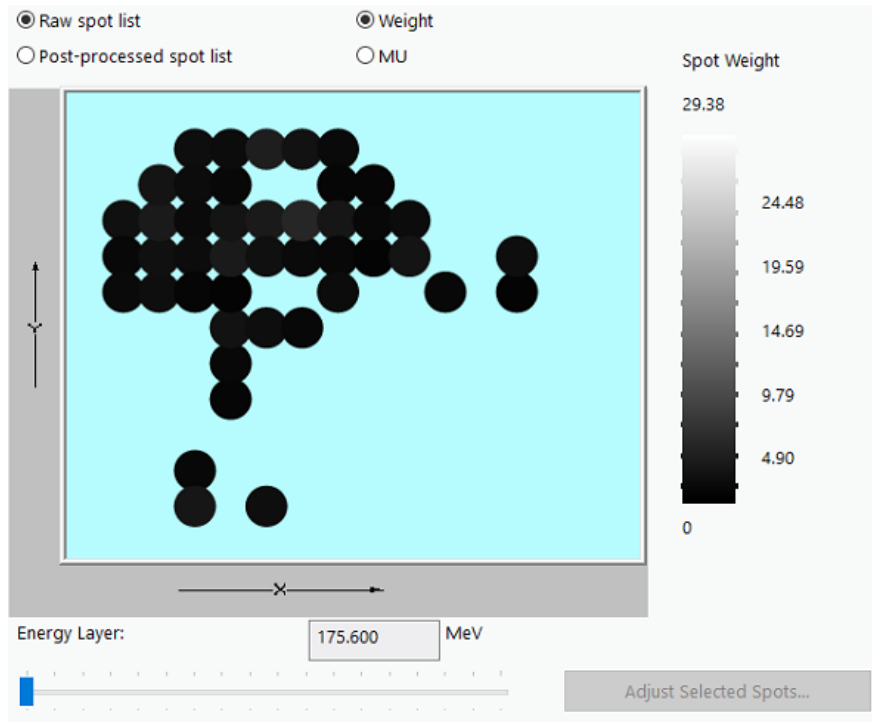


Figure 2.9 The spot weights at a single layer in proton treatment plan system.

With respect to beam scanning techniques, there exist single field optimization (SFO) and multi field optimization (MFO). In SFO, the spot positions and weights of each proton field are optimized individually, therefore, the resultant dose distribution by each field is uniform in the target volume. In MFO, the spots from all the fields are optimized together, generating highly conformal dose distributions. Unlike SFO, the dose from individual MFO fields can be relatively inhomogeneous. MFO is also referred as Intensity Modulated Proton Therapy (IMPT).

The precision of proton therapy is related to the particle involved in the radiotherapy process. The actual dose distribution resulting from IMPT is subject to various uncertainties and often deviates from the planned dose distribution. Studies showed that there are two main sources of uncertainty: one is the proton range uncertainty associated with treatment planning dose calculations, the other is the positional uncertainty

associated with the actual patient treatment [1]. The range uncertainty is caused by errors in the planning CT data and the proton beam dose calculation model. Experiments have shown that proton range has a deviation of 3% to 5% [175], [176]. Proton range uncertainties can also be caused by changes in the patient's tissue structure (*e.g.*, changes in the shape of the tumor volume.). Deviations in patient positioning and beam location during treatment induce positioning uncertainty, resulting in 1 to 3 mm differences between the anticipated and actual irradiation positions [177]. Since the dose distribution of IMPT is created by multifield superposition of several proton Bragg peaks, when a patient moves or proton range deviation exists, the dose distribution in proton radiotherapy is deformed, different from the distribution in photon radiotherapy. The conventional planning target volume (PTV) concept is not sufficient for providing robustness in target coverage in proton therapy because PTV does not consider the range uncertainty [178]. To address this issue, robust optimization has been put forward. Robust optimisation approaches take into account the dose distribution in the uncertainty scenario and optimise a less uncertainty-sensitive exposure scenario. Cubillo-Mesias *et al.* suggested using robust MFO to ensure proton plans' robustness [179]. Therefore, in this thesis, I use the MFO combined with robust optimization in Chapter 5. In proton treatment planning system, robustness optimization methods fall into two main categories: the minimax optimisation and the worst-case scenario optimization. In the minimax optimization, the treatment planning system (TPS) minimises the maximum objective function over all scenarios [180]. In the worst-case scenario optimization, each voxel corresponds to the worst dose value from all the scenario, forming a worst dose distribution into the optimization objective function for minimization. The worst-case dose distribution is unphysical, treating every voxel independently, and does not match

any of the error scenarios. However, the worst-case scenario optimization can serve as a lower bound for the worst quality of the treatment plan under the evaluate conditions, thereby being a more conservative approach than the minimax optimization [181], [182]. In Chapter 5, I use the worst-case scenario optimization, which has been widely used in the Eclipse TPS.

Chapter 3

An In-silico Prescription-dose

Optimisation Method

3.1 Introduction

Radiotherapy (RT) has been demonstrated with significantly increased survival and local control rates for brain tumors [6]. Prescription dosage is one of the main factors that can influence the radiotherapy-associated outcome, and the required dose level should be preferably determined clinically. Many researchers have been working on optimizing the current prescription dose. There have been other works performing the clinical trials to observe the optimized prescription doses. It usually takes one to eight years for researchers to track the outcome of patients' treatment. Many patients usually cannot wait for the best treatment plan due to such a time-consuming process. Therefore, how to obtain an appropriate clinical trial design in terms of prescription dose regimens in an acceptable time period is of high value in clinic radiotherapy. Scott *et al.* proposed an approach to assign personalized prescription doses based on genomic markers of radiosensitivity [29]. Gene expression-based radiosensitivity index (RSI) and genomic-adjusted radiation dose (GARD) formalism were used to calculate a personalized RT prescription dose for each patient. However, this method highly relies on biological

experiments and requires high-end equipment, usually unavailable for many institutions. Su *et al.* calculated the cut-off value of PTV radiotherapy doses by receiver operating characteristic (ROC) analysis [32], where different PTV radiotherapy doses correspond to different survival rates. However, the ROC-based dose optimisation is modelled using a single variable, while the prescription dose optimization is always a multi-variable problem.

Current standard RT focuses on physical optimisations, that is, prescribing and delivering doses to the tumor based on target volumes and positions, with an acceptable dose level exposed to normal tissues using advanced RT techniques, such as IMRT and VMAT. Physical optimisations do not consider the biological features of the tumour and normal tissues. In order to further improve the treatment outcomes, biological effects after irradiation should also be considered. Therefore, biological optimization treatment plans using radiobiological criteria and models have been put forward [183]. Current biological optimization mostly focuses on TCP and NTCP models. Since the TCP and NTCP models contain radiobiological information, they can convert a three-dimensional dose distribution into a biological-effect distribution [184]. As has been discussed in Chapter 2, if TCP and NTCP curves are far apart, a large therapeutic ratio is observed, which is beneficial to the treatment. On the other hand, if TCP and NTCP curves are close, this indicates a small therapeutic ratio, which is unfavourable for a treatment. A proper treatment plan usually has a high TCP-NTCP difference. Its corresponding dose can be considered as a satisfied treatment dose. Therefore, use of TCP and NTCP models enables us to re-optimize the prescription dose in RT. By further investigating the uncertainties within TCP and NTCP models and individual radiobiological differences (*e.g.*, different OARs) among patients, a personalized prescription-dose optimisation method is proposed

in this chapter. Prescription doses following principles herein are able to protect all the OARs within their tolerances and with higher therapeutic ratios.

3.2 Preliminaries of Radiotherapy Treatment Plan

Before patients starting radiotherapy treatment, the radiotherapy team will design external beam radiotherapy plans. According to clinical requirements and many years of clinical dosimetry practice [17], the included patient's radiotherapy treatment plan for the tumor should meet the following three conditions:

- The irradiation field in RT should be aimed at the tumor area, namely the target area. For patients whose tumor area range is difficult to determine, or after surgery, radical radiation therapy must be implemented to potential metastatic areas [17].
- Dose levels in the irradiation field should be increased in the treatment area, and in the area of the tumor to be treated, the dose distribution should be as uniform as possible. The criterion for dose uniformity is to cover the whole tumor with at least 95% of the prescribed dose, with a maximum of 107% [17] [185].
- Important organs or tissues around the tumor should be protected by reducing the dose exposure to them. Radiation received beyond their tolerable dose ranges should be avoided.

In the analysis and comparison of treatment results, not only tumor doses, but also the irradiation technique and detailed dose distribution in the treatment are taken into account. After a treatment plan meets the above dosimetry criteria for the tumor target, isodose

lines are used to analyse the dose distribution. The area that received 50% prescription dose is used to measure the radiation to normal tissues. The smaller area is covered by the isodose line of 50% prescription dose, the better protection for normal tissues can be provided. The presence of OARs should also be considered when determining the planned target area and prescribed dose. OARs refer to the important organs that may inevitably exist in the irradiation field, and their radiosensitivity (tolerable doses) will significantly affect the design of the treatment plan. The tolerated doses of various organs and tissues, *e.g.*, $TD_{5/5}$ and $TD_{50/5}$ are summarized by Emami *et al.* [37]. The size of OAR volumes in the irradiation field and the dose level of radiation are directly related to the possible damage of organs caused by irradiation, that is, the probability of normal tissue complications (NTCP). In this chapter, treatment plans which have been clinically delivered to patients followed the aforementioned principles.

To evaluate treatment plans, dose-volume histograms (DVHs) are employed because they relate the radiation dose to both target and OARs volumes. There are two types of DVHs commonly used, namely differential and cumulative DVHs. Differential DVHs (dDVHs) represent the percentage or absolute volume receiving doses in the corresponding dose bin, whereas the cumulative DVHs (cDVHs) represent the percentage or absolute volume receiving greater than or equal to the value of the corresponding dose bin. Figure 3.1 (top) shows the dDVH for the target in brain tumors, an example from the patients' cohort used in this chapter, where the blue curve is the frequency distribution within the target. The dose values are separated into specific number of dose bins. The frequency shown in Figure 3.1 (top) represents the number of sampling points corresponding to a specific dose value. The narrower the peak of the dDVH, the more homogenous the dose

distributions are within the volume of interest. Figure 3.1 (bottom) presents the cDVH for the same target. The cDVH calculation [186] is characterized as

$$cDVH(D) = \int_D^\infty dDVH(x)dx = 1 - \int_0^D dDVH(x)dx. \quad (3.1)$$

Target coverage as well as dose constraints to OARs can be assessed with cDVHs. Normally, the dose distribution could not be completely homogeneous. dDVHs are necessary in order to understand how doses distribute in the sub-volumes of a tumor or an OAR, which can be used to calculate TCP and NTCP values featuring sub-volume information.

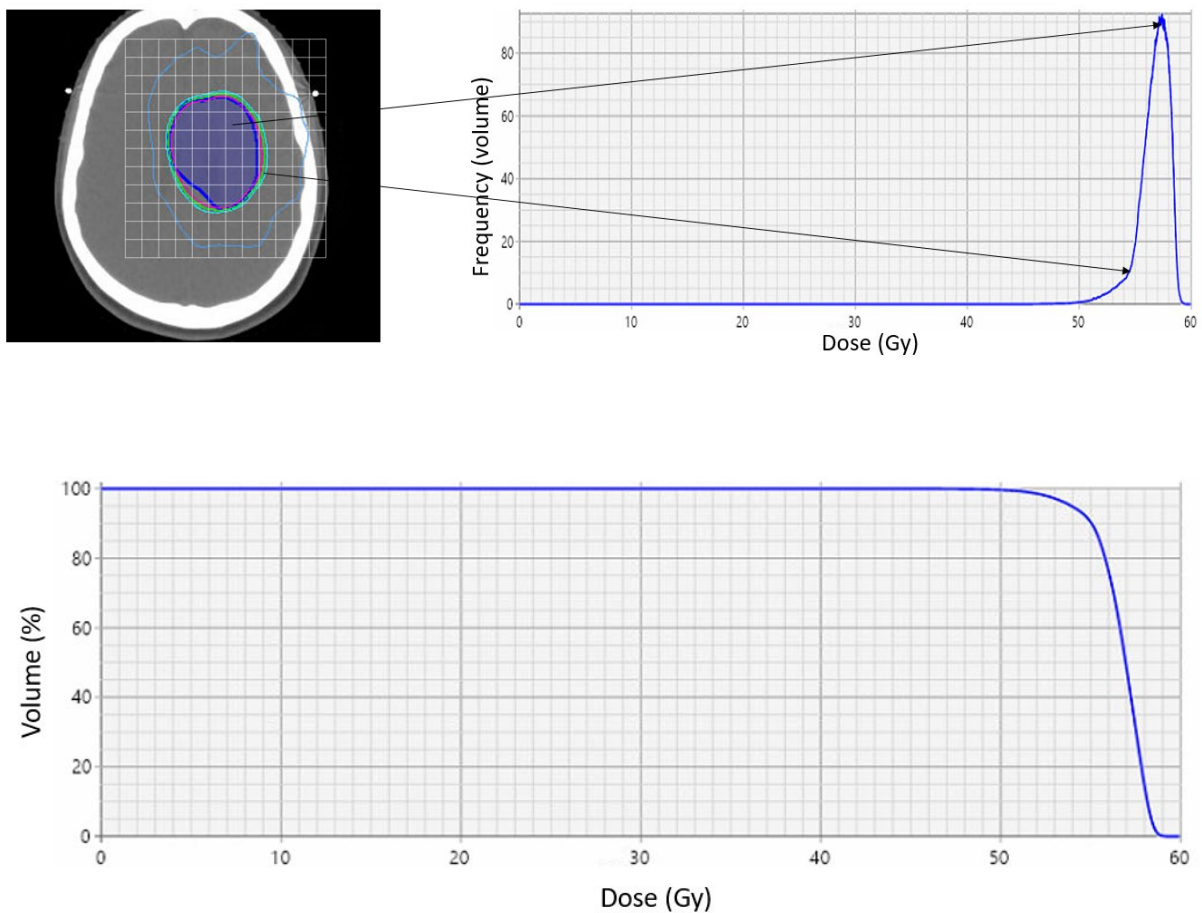


Figure 3.1 Plots of differential and cumulative DVHs.

3.3 Methods and Materials

3.3.1 Data Input and Augmentation

17 sets of data from patients with brain tumors were enrolled in this chapter, who were treated with radiotherapy combined with concurrent chemotherapy and adjuvant radiotherapy, following the standard treatment according to guidelines. Patients were treated by IMRT in 2018 and were selected after validation of the inclusion criteria. The dose was normalized to 100% at target mean according to the International Commission on Radiation Units and Measurements (ICRU) Report No.29 [187] and Report No.50 [188]. The protocol of data use was approved by the institutional ethics committees and all patients had provided written informed consent. Each enrolled patient's feature extraction was performed based on the doses and volumes of the treatment plan. After that, 17 patients' dDVHs were used as the input data. I wrote a Matlab program using dDVHs files including D_i and V_i values to calculate TCP and NTCP values, where D_i and V_i represent the dose bin and the percentage dose volume. Each patient's original prescription dose was extended by multiplying from 0.6 to 1.5 for data augmentation, in order to provide a thorough analysis of TCP distributions.

3.3.2 LQ-Poisson TCP under Inhomogeneous Dose Distribution

In radiotherapy, clinical doses that were delivered to the target have differences in each subvolume with acceptable variations. I first reviewed and evaluated TCP models for

inhomogeneous dose distribution, with a focus on widely used Poisson and Poisson linear-quadratic (LQ) TCP models. Poisson TCP only considers the probability of cancer cells being killed, denoted by α , which represents irreparable radiation damage [189]. Poisson LQ TCP not only includes α , but also considers the repair of the cancer cells after irradiation, denoted by β [189]. The Poisson LQ model is hence used for TCP calculations. Since, in clinical, the dose distribution can never be uniform in the target, as was demonstrated in Figure 3.1, the Poisson LQ model under heterogenous dose distribution is also derived in this chapter.

In the heterogenous dose distribution, there is an array of dose and volume in dDVHs, represented as (D_i, V_i) . The data is discretized such that sub-volume V_i receiving exactly D_i dose. It is implied that $\sum_i V_i$ is the total volume of the tumor. Using the assumption of independent sub-volumes (V_i) in the case of heterogeneous irradiation, the overall probability of tumor control is the product of the probabilities of killing all clonogens in each tumor subvolume, expressed as [190]

$$TCP = \prod_i TCP(D_i, V_i). \quad (3.2)$$

As has been mentioned in Chapter 2, if the dose distribution is homogeneous, the Poisson-LQ TCP model is:

$$TCP = \exp[-N \exp(-(\alpha + \beta d)D)], \quad (3.3)$$

where N is the initial number of clonogens, d is the single dose for one fraction, D is the total dose, α and β are cell radio-sensitivity parameters. Combining Equation 3.3 with

Equation 3.2 and replacing N with NV_i and D to D_i [190], Equation 3.4 is deduced with respect to the discrete dose distribution:

$$TCP = e^{\sum_i V_i [-N e^{-(\alpha + \beta d) D_i}]} \quad (3.4)$$

Furthermore, d in Equation 3.4 is replaced with $\frac{D}{n}$, where n is the number of treatment fractions, then Equation 3.4 can be rewritten as:

$$TCP = e^{\sum_i V_i [-N e^{-(\alpha + \frac{\beta D_i}{n}) D_i}]} \quad (3.5)$$

This analysis provided a derivation from a uniform dose distribution to a non-uniform dose distribution, which is suitable for all Poisson-based TCP models.

3.3.3 Parameter Selection

After selecting the input dDVH files, either a normal tissue or a tumor dDVH file needs to be identified. Then, parameters for TCP/NTCP models that stored in the parameter databases need to be specified for calculating TCP or NTCP values. For tumors, parameters are selected by using Leeuwen *et al.*'s summary [41] as well as other related work in this field [35], [176]. For normal tissues, after selecting the organ type, the Matlab program retrieves all available parameters which are stored in the databases for this organ. The databases include parameters for different complication endpoints. In this chapter, I employed the Poisson LQ model for TCP and the LKB model for NTCP because they are most common used in current commercial TPS.

The selection of LQ parameters α , β and α/β is pivotal for a reliable estimate of radiation response. Leeuwen *et al.* [41] performed a systematic review of α and β values

used in the LQ TCP model. For brain tumors, Leeuwen *et al.* [41] and Pedicini *et al.* [191] summarized different sets of α , β and α/β values. The cohort patients used in this chapter are mainly glioma, a type of malignant tumor and they are treated with radiotherapy combined with concurrent chemotherapy and adjuvant radiotherapy. The parameters that related to the aforementioned treatment protocol are selected for the Poisson LQ TCP model, as are shown in Table 3.1. It is worth noting that the selected parameters are all from the clinical radiotherapy data, their results are therefore more reliable rather than ones from in vitro biological experiments¹.

Table 3.1 The range of α and β for the Poisson LQ TCP model.

Database	α/β [Gy]	$\alpha \times 10^2$ [Gy ⁻¹]	$\beta \times 10^3$ [Gy ⁻²]
Pedicini <i>et al.</i> 2014 [191]	8.0 [5.0, 10.8]	12.0 [10.0, 14.0]	15 [13.0, 20.0]
Qi <i>et al.</i> 2006 [192]	10 [5.1, 25.1]	6.0 [1.0, 11.0]	6.0
Qi <i>et al.</i> 2006 [192]	5.8 [6.0, 17.6]	11.0 [1.0, 21.0]	19.0
Barazzuol <i>et al.</i> 2010 [193]	3.1	9.4	30.0

In Table 3.1, the estimated parameters and their uncertainty intervals (95%) are presented. However, Qi *et al.* did not report the uncertainty intervals for β [192], and Barazzuol *et al.* did not report the uncertainty intervals for α , β and α/β in their analyses [193].

Parameters used for the LKB NTCP model are selected from Emami *et al.*'s study [37] and the guideline from Quantitative Analyses of Normal Tissue Effects in the Clinic

¹ A 2Gy dose of MV photons is thought to typically halve cell survival. Thus, $\alpha(1 + 2\beta/\alpha)$ is typically $\ln 2/2$ or 0.35. Values calculated from Table 3.1 are around 0.16, lower than the value calculated from in-vitro α and β values.

(QUANTEC) [54]. Table 3.2 presents a summary of different parameters values. To investigate the sensitivity of TCP and NTCP models to different parameter sets, values listed in Tables 3.1 and 3.2 have been used in this chapter to increase the robustness of models.

Table 3.2 Parameters used in the LKB NTCP model.

Parameter	Brain stem	Lens	Optical nerves	Chiasma
D50	65.00 [48], 72.00 [51]	18 [48]	65.00 [48], 70.00- 72.00 [194], 72.00-75.00 [195]	65.00 [48], 70.00 [194], 72.00 [196], 72.00-75.00 [195]
m	0.14 [48], 0.10 [51]	0.27 [48]	0.14 [48]	0.14 [48]
n	0.16 [48], 0.25 [51]	0.3 [48]	0.25 [48]	0.25 [48]

3.3.4 Calculations of TCP and NTCP

Using the retrieved parameters and the dDVH (D_i, V_i), TCP and NTCP values using the Poisson LQ model and the LKB model can be calculated by Equation 3.5 and Equation 2.18 presented in Chapter 2. As was mentioned earlier in Section 3.3.3, model parameters related to radiobiological heterogeneity have been found in the Poisson LQ TCP and LKB models. In the TCP model, α and β values range from 0.01 to 0.21 and from 0.013 to 0.03, respectively. In the NTCP model, there are 27 combinations of parameter sets for brainstem, 1 set for lens, 3 sets for optical nerves and chiasma, respectively. All sets of parameters were used for TCP and NTCP calculations with the propagation of their

uncertainties. The distributions of TCP and NTCP values were then generated by each of the sampled parameter sets. After that, the polynomial annealing method was used to produce the curve of TCP and NTCP distributions.

3.3.5 Prescription Dose Optimisation

I now investigate a prescription dose optimisation method based on the above radiobiological models (*i.e.*, TCP and NTCP) in order to increase the tumor's therapeutic ratio. Therapeutic ratio is related to the probability of tumor control and the surrounding normal tissue complication probability undergoing a certain treatment technique. In this chapter, therapeutic ratio (Tr) is defined as

$$Tr = (TCP - NTCP)/(TCP_{ideal} - NTCP_{ideal}) \quad (3.6)$$

The TCP_{ideal} and $NTCP_{ideal}$ in radiotherapy should be 1 and 0, respectively. Therefore, in Equation 3.6, $TCP_{ideal} - NTCP_{ideal}$ equals 1. Conventionally, a rise of TCP about 10%-20% per 10% increase in dose is expected [35]. A good treatment plan is expected to increase the radiation dose of the tumor while not cause normal tissue damage. However, for some tumors the prescription dose cannot be given very high due to the occurrence of possible serious radiation damage. Therefore, I constructed a prescription dose optimisation model, in order to accurately determine the prescription dose of the tumor, so as to achieve tumor control and reduce normal tissue complications.

Since TCP and NTCP curves show the treatment effect with dose changes, in this chapter, I combined cancer-killing and OAR complication probability as a co-optimization objective. The aim of this model is to increase the tumor control probability while

maintaining or reducing the normal tissue complication probability and eventually maximize the therapeutic ratio. The corresponding metric is defined as the target dose (TD), *i.e.*, the dose position with the maximal value of the difference between the TCP and NTCP probability. Since different OARs have their corresponding tolerable radiation dose, named T_{OAR} , I put it as constraints in the dose optimisation model. Table 3.3 shows the dose range of various OARs' tolerances, according to the Emami *et al.*'s review [37] and the guideline from Quantitative Analyses of Normal Tissue Effects in the Clinic (QUANTEC) [54]. For lens, 6Gy and 10Gy have been used as tolerable doses, indicating 1% and 50% risk of cataract, respectively [33], [42]. The uncertainties of model parameters and the tolerable radiation doses to the OARs were adopted in the proposed dose optimization method for a high degree of robustness.

Table 3.3 OARs' tolerance [33], [42]. Dmax means the maximum dose in the corresponding OAR; D0.1cc means the dose received by 0.1 cubic centimeters (cc) of the corresponding OAR; V59 means the volume of the corresponding OAR receiving a dose of 59Gy.

OARs	OARs' tolerance
Brain stem	Dmax <54 Gy, D0.1cc <64Gy, V59 \leq 10cm ³
Chiasm	Dmax<55Gy
Optical nerves	Dmax<54Gy
lens	Dmax<10Gy, Dmax<6Gy

To begin with, a single OAR case is considered in the dose optimisation, which can be characterised in Equation 3.7. The objective of the prescription dose optimisation is to

maximum therapeutic ratio, *i.e.*, the difference between TCP and NTCP values at a specific dose level D , defined as $P(D)$, subject to various uncertainties from TCP and NTCP model parameters and the maximum delivered dose to a specific OAR under dose level D , expressed as $D_{\max}^{\text{OAR}}(D)$. The principles of RT require that $D_{\max}^{\text{OAR}}(D)$ should not exceed the OAR tolerable dose (T_{OAR}) in a proper treatment plan.

$$\text{maximize } P(D) = \text{TCP}(D) - \text{NTCP}(D)$$

$$\text{subject to } \begin{cases} D_{\max}^{\text{OAR}}(D) < T_{\text{OAR}}, \\ \text{TCP uncertainties,} \\ \text{NTCP uncertainties.} \end{cases} \quad (3.7)$$

In Equations 3.7 and 3.8, TCP and NTCP uncertainties represent the variations of parameters (shown in Tables 3.1 and 3.2) used in TCP and NTCP models.

After that, considering most patients' treatment plans involve several OARs, I further extend the single-OAR optimisation model (Equation 3.7) to a multi-OARs optimisation model for the calculation of optimized prescription doses (D_{opt}) considering multiple OARs' constraints. Assume there are N different OARs, maximum delivered doses to OAR_i under the dose level D , $D_{\max}^{\text{OAR},i}(D)$, $i \in [1, N]$, can be calculated based on different OAR tolerances T_{OAR}^i for $i \in [1, N]$. In some cases, even though a $D_{\max}^{\text{OAR},i}(D)$ is satisfied by its corresponding OAR tolerance, if this dose is applied in the treatment, the resultant dose imposed on other OARs may violate their tolerances. Therefore, a multi-OARs optimisation model shown in Equation 3.8 is presented to produce an optimised prescription dose D_{opt} .

$$\text{maximize } P(D) = \text{TCP}^i(D) - \text{NTCP}^i(D), i \in [1, N];$$

$$\text{subject to } \begin{cases} D_{\max}^{\text{OAR},i}(D) < T_{\text{OAR}}^i, \forall i \in [1, N], \\ \text{TCP uncertainties,} \\ \text{NTCP uncertainties.} \end{cases} \quad (3.8)$$

The detailed procedure is shown below. For a dose level D , if it allows all $D_{\max}^{\text{OAR},i}(D)$ to fit their tolerance T_{OAR}^i , $i \in [1, N]$, *i.e.*, the dose delivered to brain stem, eye globes, lens, optical nerves and chiasma are all within their tolerance, D is considered as a valid value and recorded. If there are multiple recorded dose levels, one with the max subtraction between TCP and NTCP is selected as the optimised prescription dose D_{opt} .

Figure 3.2 shows the TCP and NTCP distributions for a single patient as an example. D_{opt} is the optimized prescription dose to satisfy all the OARs' tolerances, and enables the maximum difference between TCPs and NTCPs.

3.3.6 Evaluation

Two metrics are defined in this section to evaluate the optimized prescription dose: 1) OARs tolerance *i.e.*, transferring dDVHs to cDVHs to check whether the radiation dose of OARs is tolerable; 2) therapeutic ratio increase, *i.e.*, comparing the therapeutic ratio under new prescription doses to see whether it is larger than one using the original prescription dose.

The datasets used in my prescription dose prediction model are dDVHs. However, a DVH used for clinically evaluation will always be the cumulative one, *i.e.*, the cDVH which

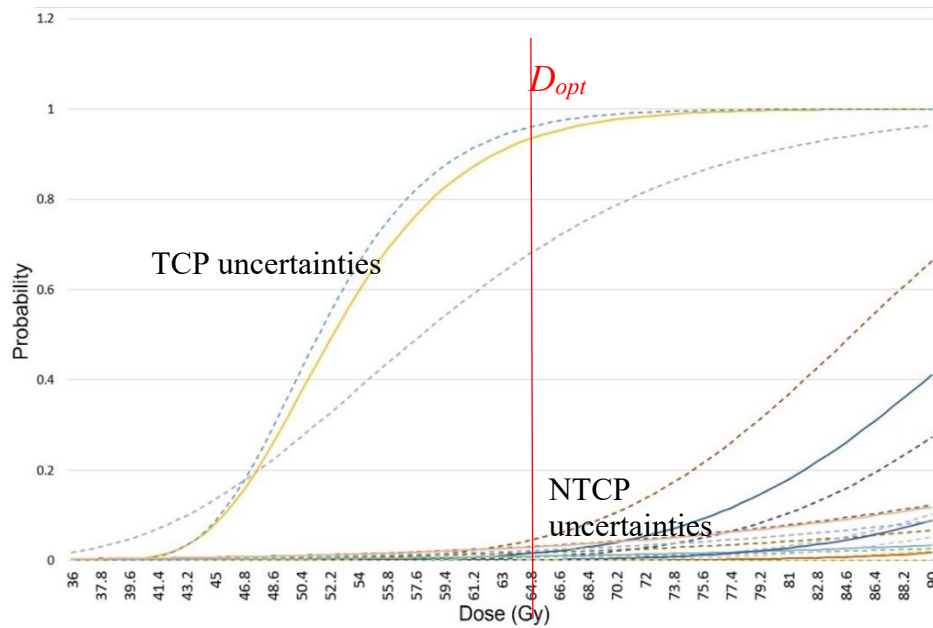


Figure 3.2 TCP and NTCP distributions for one patient. The TCP and OAR's NTCP have a range of uncertainties. Solid lines represent the median value of TCPs and each OAR's NTCPs, and dashed lines represent their lower and upper bound. D_{opt} denotes the optimized prescription dose.

represents the volume of structure receiving greater than or equal to a certain dose. With a cumulative DVH, it is easy to select the volume for dose limits. Therefore, in order to evaluate if the treatment plan implemented with the optimized prescription dose satisfied the OARs tolerance, I need to transfer the differential to cumulative DVH. The dDVH can be transferred from cDVH using the Equation 3.1.

There are four metrics I selected to evaluate treatment plans according to Table 3.3, including the max dose of brain stem, the max dose of lenses, the max dose of optical nerves, the max dose of chiasma. Last but not least, I calculated the therapeutic ratio using

new prescription doses to see whether it is greater than one using the original prescription dose under corresponding model parameters.

3.4 Results and Discussions

3.4.1 TCP and NTCP Values

The detailed dataset of patients regarding to tumor type, prescription dose, tumor stage and therapeutical ratios under initial and optimised prescription doses in this study are explained in Table 3.4. As mentioned in Section 3.3.1, each patient's original prescription dose was extended by multiplying from 0.6 to 1.5 for data augmentation. Thereafter, TCP and NTCP curves considering radiobiological uncertainties for 17 patients with brain tumors can be achieved by polynomial annealing, executed in MATLAB. Figure 3.2 shows TCP and NTCP distributions for one patient as an example, where parameter uncertainties in TCP and NTCP calculations have been demonstrated by multiple curves in top left and bottom right corners, respectively.

3.4.2 Optimized Prescription Doses

Following the principle of the proposed prescription dose prediction model, we calculated the optimised prescription dose for all 17 patients, as is shown in Table 3.4. It is interesting to note that these patients are randomly selected and 7 of them are GBM, accounting for the largest number of tumor types, which is consistent with the epidemiological statistical results, shown in Chapter 2. There are 11 of 17 patients whose optimised dose values are higher than the original ones, shown in bold. The differences

between optimised and the original dose are within $\pm 20\%$. This makes sense since the proposed method is based on a predefined prescription dose. The lower and upper bound in the optimized dose is calculated by considering all the uncertainties in terms of radiobiological parameters and OARs' tolerant doses in the optimization model, as listed in Table 3.4. The prescription dose considered the strict OAR tolerance for lenses are not presented, because most of our patients are glioma, one of the most malignant tumor types, and it is not necessary to comprise the target dose for over-protecting OARs.

Using the radiosensitivity parameters in the Poisson LQ TCP model (*i.e.*, α , β) listed in Table 3.1 lead to different TCP curves. We used γ_{50} derived from each TCP curve to analyse how the change of TCP varies with dose increases, as elaborated in Table 3.5. Combined with parameter uncertainties in the LKB NTCP model (Table 3.2), optimized doses and the corresponding therapeutic ratios were calculated in Table 3.4, where the median, upper bound and lower bound of therapeutical ratios under initial and optimised prescription doses were reported. Table 3.5 also showed the TCP values under the median optimized doses.

Table 3.4 Optimised prescription doses for 17 brain tumor patients. There are 11 of 17 patients whose optimised dose values are higher than the original ones, shown in bold.

Patient	Tumor type	WHO classification	Initial Dose (Gy)	Optimised Dose (Gy)	Therapeutical ratio (%) under initial dose	Therapeutical ratio (%) under optimised dose
					Median [range]	
1	Oligodendroglioma	3	60.00	62.57 [60.47, 75.56]	76.39 [35.74, 83.61]	85.47 [43.18, 89.90]

2	Oligodendroglioma	3	60.00	61.95 [61.35, 74.40]	80.75 [44.48, 86.70]	87.57 [50.44, 91.31]
3	Oligodendroglioma	3	60.00	61.12 [60.24, 64.39]	63.61 [26.17, 73.88]	71.84 [29.55, 78.88]
4	Glioblastoma	4	56.00	57.24 [56.37, 66.47]	77.16 [47.65, 81.57]	89.17 [60.86, 92.67]
5	Astrocytoma	3	59.92	56.63 [52.43, 56.99]	90.25 [73.57, 92.46]	94.80 [79.68, 96.49]
6	Oligodendroglioma	2	54.00	55.02 [54.51, 61.13]	42.68 [12.80, 55.59]	52.38 [15.13, 62.00]
7	Meningioma	3	54.00	52.09 [50.16, 52.76]	52.44 [26.97, 57.89]	66.83 [36.79, 73.01]
8	Glioblastoma	4	56.00	60.87 [56.78, 69.06]	72.01 [39.04, 77.50]	88.52 [55.37, 92.55]
9	Oligodendroglioma	2	54.00	64.55 [60.04, 70.17]	83.12 [56.86, 85.86]	85.88 [68.33, 90.14]
10	Glioblastoma	4	54.00	57.73 [56.11, 64.15]	83.12 [56.86, 85.86]	88.57 [63.01, 91.06]
11	Oligodendroglioma	3	54.00	52.43 [50.73, 53.21]	25.13 [5.52, 31.50]	40.75 [9.61, 50.16]

12	Malignant fibroma	3	54.00	51.84 [49.12, 53.58]	62.21 [41.42, 66.29]	77.84 [54.53, 82.13]
13	Glioblastoma	4	60.00	56.29 [53.05, 59.08]	46.72 [12.50, 51.29]	69.30 [24.04, 75.50]
14	Cerebral hemangiopericytoma	3	60.00	67.13 [65.87, 74.59]	63.23 [17.31, 73.71]	89.94 [39.18, 94.34]
15	Glioblastoma	4	60.00	63.86 [61.16, 64.88]	93.74 [81.03, 94.86]	96.06 [84.47, 97.05]
16	Glioblastoma	3	60.00	58.39 [53.35, 59.41]	81.52 [51.08, 84.83]	85.85 [55.83, 88.90]
17	Glioblastoma	4	60.00	73.89 [70.64, 76.80]	81.13 [47.17, 86.83]	98.87 [80.40, 99.73]

Table 3.5 TCP increases based on different γ_{50} values.

Patient	γ_{50} (min)	γ_{50} (median)	γ_{50} (max)	TCP (%) under the initial doses with			TCP (%) under the median optimized doses with		
				γ_{50} (min)	γ_{50} (median)	γ_{50} (max)	γ_{50} (min)	γ_{50} (median)	γ_{50} (max)
1	1.97	3.48	3.81	41.67	78.32	85.51	47.27	87.54	92.40
2	1.87	3.36	3.69	50.42	84.45	90.02	56.10	91.49	95.24
3	2.10	3.76	4.05	28.02	66.84	76.73	31.82	72.67	81.67
4	1.66	3.18	3.51	59.25	86.99	91.65	62.43	93.39	96.28
5	1.32	2.81	3.08	88.20	97.80	98.84	83.20	96.02	97.67

6	2.12	3.67	3.99	22.97	50.17	61.11	24.62	55.77	66.55
7	1.77	3.28	3.64	46.93	71.09	75.27	40.22	68.55	74.05
8	1.79	3.30	3.61	44.26	76.54	81.71	62.15	94.62	98.21
9	1.38	2.91	3.16	68.33	87.88	88.64	80.06	96.14	99.11
10	1.58	3.10	3.38	64.48	88.53	89.88	72.48	94.07	96.37
11	2.17	3.75	4.07	15.77	55.64	68.66	11.87	44.74	60.14
12	1.53	3.06	3.36	62.54	82.43	85.61	57.05	79.70	83.95
13	2.09	3.65	3.97	42.64	76.52	80.57	35.82	72.00	78.15
14	2.22	3.79	4.09	21.14	63.61	74.09	43.17	90.71	95.09
15	1.19	2.67	2.90	83.07	95.61	96.66	88.98	98.35	99.26
16	1.68	3.22	3.49	60.68	89.53	91.87	57.48	87.23	90.19
17	1.81	3.36	3.62	50.00	81.49	86.89	86.86	99.52	99.84

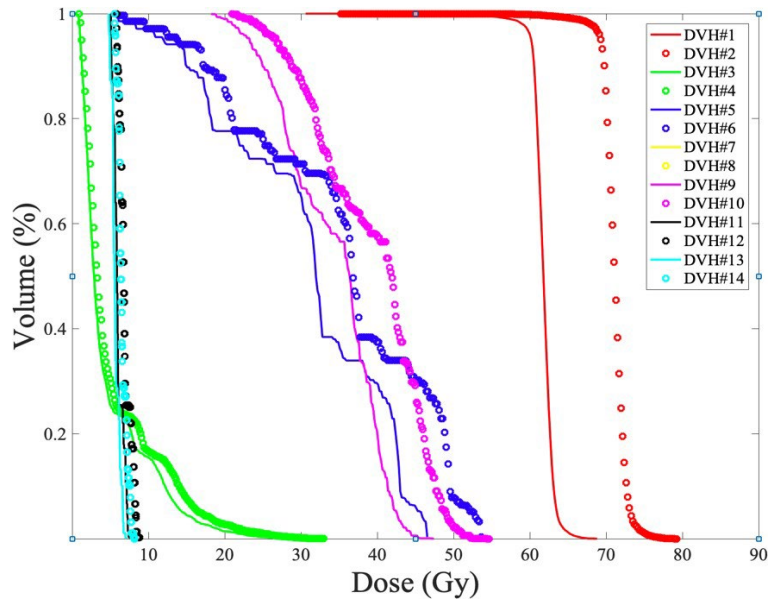
Let us now examine how the doses achieved by the proposed method outperform their original ones used in treatment. A metric called satisfactory rate is defined as the ratio of cases satisfied by new prescription dose versus the total number of patients in target. When the received radiation dose in OARs did not exceed their tolerances according to Table 3.3, this dose is considered as a successful case in this evaluation. In this chapter, the total number of patients is 17. As shown in Table 3.6, the proposed method achieved 100% satisfactory rate for all patients tested. All the OARs are carefully protected under the optimized prescription dose.

Table 3.6 Successful rates of OARs' metrics for 17 brain tumor patients.

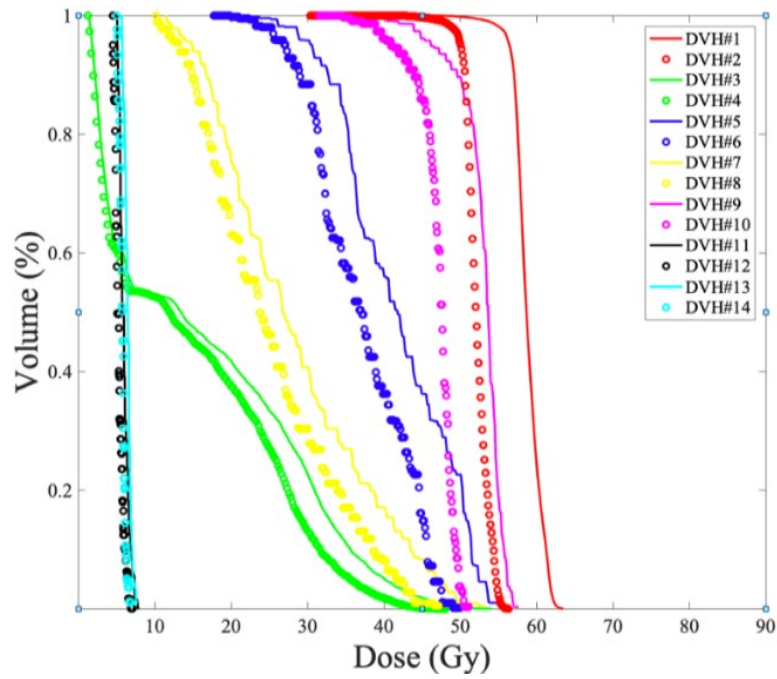
OARs' metrics	Successful rate
Max dose of brainstem	100% (17/17)
Max dose of left lens	100% (17/17)
Max dose of right lens	100% (17/17)
Max dose of left optical nerve	100% (17/17)
Max dose of right optical nerve	100% (17/17)
Max dose of chiasma	100% (17/17)

After inputting the optimized prescription dose into the TPS, a new dose volume histogram can be obtained. Figure 3.3 shows the DVH curves for 2 patients' cases (patient #13 and #17), without loss of generality, where the dotted curves represent new dose volume after optimisation and the solid curves indicating the original ones before optimisations. For patient #17, the optimized prescription dose is greater than the original prescription dose, while the factors in patient #13 shows the opposite.

In the first example case of patient #17, the original prescription dose is 60Gy while the optimized prescription dose is 73.89Gy, which is greater than the original dose level. The whole DVH shifted to the right, shown in Figure 3.3(a). As was shown in Table 3.4, for patient #17, the median therapeutic ratio increased from 81.13% and 98.87%, and the radiation doses to OARs are all increased but still no more than the OARs tolerance, as shown in Table 3.7(a). Therefore, the prescription dose calculated by the proposed dose prediction model protects each OAR and achieves the therapeutic ratio improvement.



(a) Dose volumn histogram of patient #17



(b) Dose volumn histogram of patient #13

Figure 3.3 Dose volume histogram of patient #17 (a) and dose volume histogram of patient #13 (b) under optimized and original prescription doses. The dotted lines represent dose volumes after optimisation and the solid indicating the original dose volumes. For

patient #17, the optimized prescription dose is greater than the original one. For patient #13, the optimized prescription dose is lower than the original one.

Table 3.7 Maximum doses to OARs under optimized and original prescription doses (PDs).

(a) Patient#17

Structures	$D_{\max}^{\text{OAR},i}$ under original PD (60.00Gy)	$D_{\max}^{\text{OAR},i}$ under optimized PD (73.89Gy)
Brain stem	45.38	53.01
Left lens	7.61	8.05
Right lens	7.56	7.99
Left optical nerve	43.39	51.65
Right optical nerve	44.06	52.44
Chiasma	43.12	51.33

(b) Patient#13

Structures	$D_{\max}^{\text{OAR},i}$ under original PD (60.00Gy)	$D_{\max}^{\text{OAR},i}$ under optimized PD (56.29Gy)
Brain stem	56.54	53.06
Left lens	7.98	7.48
Right lens	7.91	7.43

Left optical nerve	47.49	44.56
Right optical nerve	57.56	52.99
Chiasma	57.15	53.62

As for the second case of patient #13, the optimized prescription dose is 56.29Gy, lower than the original dose 60Gy. The whole DVH shifted to the left, as shown in Figure 3.3(b). Moreover, Table 3.7(b) illustrates the maximum dose to OARs using the original and the optimized prescription dose. I remark that some OARs exceeded the tolerance under the original prescription dose, such as brain stem, left optical nerve, and chiasma with the max dose as 56.54Gy, 57.56Gy and 57.15Gy, respectively, exceeding their tolerances. When the optimized prescription dose is applied, it can satisfy the OARs radiation dose tolerance and all the normal tissues can be better spared.

As for the therapeutic ratio for patient #13 when applying the original and the optimized prescription dose into TCP and NTCP models, Table 3.4 showed that the therapeutic ratio was increased to 69.30% versus the original 46.72%. Although doctors and physicists would have their trade-offs about OARs from overdosing at their original prescribed doses, the proposed method can provide a new treatment planning perspective, especially for those cases where the tumor is large and very close to OARs.

It is noted that, the majority of patients recruited in this chapter are diagnosed with high grade brain tumor, *i.e.*, grade III (anaplastic) oligodendroglioma, grade III astrocytoma, grade III meningioma, grade III malignant fibroma, grade III cerebral hemangiopericytoma and grade III & IV GBM. From the RT's perspective, current

completed clinical trials usually employed 54Gy in 27 fractions to 60Gy in 30 fractions for grade III (anaplastic) oligodendroglioma [197] [23], [198]–[200]. 5 years overall survival (OS) ranges from 58% to 59% and progression free survival (PFS) ranges from 47% to 50%. In the clinical trials conducted by Cairncross *et al.* [199], 65% of patients experienced grade 3 or 4 toxicity. In the Karim *et al.*'s study [23], long-term sequelae retrieved from follow-up CT scans were rare happened. For grade III astrocytoma, also called anaplastic astrocytoma, 60Gy is usually employed for RT [13], [201]. According to the statistic analysis in 2021 [13], the 5-years survival rate for grade III astrocytoma ranges from 24.5% to 60.9% corresponding to different age groups. The radiation doses are generally in the range of 54–60 Gy delivered in 1.8–2 Gy daily fractions for grade III meningioma [202]. Rogers *et al.* conducted a clinical trial treating patients with meningioma using 54Gy and 60Gy, respectively [203], [204]. Seidensaal *et al.* summarized 44 treatments from 2009 to 2018 for malignant fibroma [205]. Patients received radiation dose ranging from 39.6Gy to 66.0Gy. The progression-free survival in 3 and 5 years was 72.3 and 58.4% and the overall survival was 97.4 and 97.4%, respectively. Khan *et al.* conducted a systematic review summarizing the external beam radiation dose escalation for high grade glioma [206]. In this review, there was a Phase II study investigating the efficacy and toxicity of delivering radiation dose up to 72.6Gy. This treatment was reasonably tolerated with only grade 1 and 2 toxicities noted [207]. Most trials included in the analysis were published before 2000 and they used outdated radiotherapy techniques such as whole brain radiotherapy rather than local radiotherapy (targeted only to the tumor and not the whole brain), which bring inevitable hazard to normal tissues and OARs. With the development of precise radiotherapy, *e.g.*, IMRT, normal tissues and OARs can be better protected and doses to tumor can have headroom

to increase. As was demonstrated in this chapter, among the patient cohort, the highest doses employed was 75.56Gy for patients with III glioma and 76.68Gy for IV glioma (GBM) with tolerable doses to all OARs. Therefore, it is anticipated that the proposed prescription dose optimization model can be applied to clinical trials design.

Since current dose prescription optimisation methods focus on physical optimisations, such as tumour volumes and positions [208]. In this chapter, I proposed a novel prescription-dose optimization method by investigating biological effects, *i.e.*, use of TCP and NTCP models, with a particular focus on prevailing models used in commercial treatment planning systems (TPS). TCP and NTCP models have been used to evaluate and compare treatment plans [46] and describe tumour control and normal tissue complication probabilities [50]. Compared with previous studies using TCP and NTCP models, this chapter further investigates various uncertainties within TCP and NTCP models to provide a robust prescription-dose prediction. In addition, a personalized treatment framework considering different OARs among patients is finally presented, able to predict a prescription dose based on various constraints for individual patients.

3.5 Conclusion

In this chapter, I have proposed an optimization of prescription doses by investigating radiobiological models, paving the way for personalized optimization and treatment. For a specific patient, the proposed method produces a prescription dose by analysing a set of available constraints, such as tolerance of different OARs, and various radiobiological uncertainties (*e.g.*, parameters used in TCP/NTCP models), *etc.* Results demonstrated a

higher therapeutic ratio while protecting OARs, especially for larger tumors that close to the OARs.

Among 17 patients evaluated in this chapter, 7 of them are with Glioblastoma (GBM), which is considered as one of the most challenging tumors treated in photon radiotherapy. The results show that 5 GBM patient cases can increase the prescription dose to improve the therapeutical ratio. Only 2 of the GBM patients show a decreased prescription dose to increase the therapeutical ratio, because the tumor area is very close to the OARs. The reduced dose to the tumor target sacrificed for the OARs' protection, however, leads to tumor progression which will still bring severe agony for OARs and patients. To address this issue, the next chapter will introduce a heterogeneous dose escalated radiotherapy for GBM, to escalate the dose focally at specific intratumoural areas.

Chapter 4

Isotoxic Dose Escalated Radiotherapy for GBM Based on Diffusion-Weighted MRI and Tumor Control Probability

4.1 Introduction

The work described in the previous chapter predicts the prescription dose for individual patient by the well-established radiobiological models describing the TCP and NTCP, and the prescription dose optimization is preformed to the whole tumor. This may result in a reduced prescription dose versus the original one, when a tumor is very close to OAR, because the doses to tumor target sacrificed for the OARs' protection. For tumors such as Glioblastoma Multiforme (GBM) that are highly malignant, if radiation doses delivered to tumors are not sufficient, the tumor control will be poor. Therefore, a more practical way is to define risk of progression in different parts of tumor by considering the tumor's biological heterogeneity. An increased dose is applied only to some parts of the tumor which are more likely to progress. Dose levels to other area are not increased, avoiding an irradiation dose grow to the surrounding OARs.

Since GBM, a WHO Grade 4 glioma, is the most common malignant primary brain tumor [13], this chapter focuses on a cohort of patients with GBM. The standard GBM treatment for patients younger than 70 years old and Karnofsky Performance Status (KPS) more than 70 is 60Gy radiotherapy delivered in 30 fractions (2Gy per fraction) with concurrent and adjuvant temozolomide chemotherapy [62]. For GBM patients older than 70 years old and/or KPS less than 70, treatment using 40.05Gy in 15 fractions with concurrent and adjuvant temozolomide chemotherapy is considered [62]. However, long term control is hard to achieve with median survival time of 15-18 months and 2-year survival rate of 26-33% [209], [210]. Most recurrences after radiotherapy occur inside the irradiated area, at a rate from 58% to 92% [67]–[75], suggesting that the prescribed radiation dose is not sufficient for tumor control, therefore increasing the radiation dose can reduce local recurrences. However, clinical trials where the dose was escalated uniformly across the tumor have shown an increase in toxicity because of the associated increased dose to the surrounding healthy tissues and organs at risk (OARs) [77], [211]. An alternative strategy is to identify intratumoural areas with a higher risk of progression to escalate the dose isotoxically, *i.e.*, respecting the same dose-volume constraints for OARs as per the standard treatment (of 60Gy in 30 fractions). This is called isotoxic dose escalation, achievable by “dose painting” as proposed by Clifton Ling [139].

TCP models have been theoretically framed to enhance the tumor control prediction by modulating radiobiological parameters, such as α and β , estimated from in-vitro cell-plating experiments to clinical trials. However, α and β still cannot fully describe intra- and inter-patient variabilities or account for tumor heterogeneities. To investigate tumor heterogeneities, medical imaging can be used to bring quantitative information into TCP models, describing tumor heterogeneity at the voxel scale. Among imaging techniques,

magnetic resonance imaging (MRI) has gained a particular relevance in the radiation oncology workflow over the last decade [112], [212]. Various MR techniques can provide 3D spatial maps of anatomical and quantitative information. Many clinical trials have been conducted using quantitative imaging (*e.g.*, PET or MRI) to identify radio-resistant areas within various tumors [103]–[105], [107]. Compared with conventional anatomical imaging modalities such as CT and T1/T2 weighted MRI, functional imaging can provide additional information on tumor heterogeneity by providing information on organ physiological function. In turn, this data could facilitate the planning and delivery of radiotherapy. For GBM, some studies employed quantitative imaging techniques, such as positron emission topography (PET) and magnetic resonance spectrum imaging (MRSI) to define the high-risk areas [103]–[108]. In addition, since tumor cell density is considered as an important factor that determines the treatment outcome [134]–[136]. Diffusion-Weighted Magnetic Resonance Imaging (DW-MRI) allows us to measure *in vivo* the density of cells inside the body [132], [133]. Diffusion-weighted (DW) MRI is a well-established method to characterize oncological lesions in terms of cellular density, proliferation power and cellular permeability, by means of apparent diffusion coefficient (ADC) maps [115], [213]. The inclusion of this information at the voxel level in TCP models is believed to predict voxel-level tumor progress. In Casares-Magaz *et al.*'s study [130], ADC maps were computed from DW-MRI before radiotherapy and from them cancerous cellular density was estimated. This study showed that use of MRI-driven cellular density can enhance TCP differences inside tumor, suggesting a heterogeneous representation of tumor characteristics at the voxel level. Standard radiobiological theory dictates that the radiation dose should increase in proportion with the log number of tumor cells in order to increase the probability to stop a tumor's growth or even eradicate it

[214], [215]. DW-MRI-based dose painting can identify area with insufficient doses to achieve control and then direct dose boosts accordingly. DW-MRI is converted into apparent diffusion coefficient (ADC) maps, which are inversely correlated with tumor cell density [123], [124], [216]–[223].

Since ADC values have been demonstrated as a significant association with overall survival [224], [225], in this chapter, I used ADC maps to calculate tumor cell density and derive voxelised 3D cell distributions. A personalized biological model was employed to calculate the voxel-level tumor control probability (TCP) that corresponds to the planned dose distribution for each patient treatment. This in turn is used to change the radiotherapy plan, by following a dose painting method to escalate the dose focally at specific intratumoural areas, which showed a higher disease burden, in order to increase TCP values.

4.2 Methods

In this chapter, pre-treatment ADC maps were derived from DW-MRI of ten GBM patients treated with radical chemoradiotherapy (60Gy in 30 fractions) and are used to calculate the cell density maps in their gross tumor volumes (GTVs) using an empirical formula, shown in Section 4.2.2. Since GTVs are defined on the radiotherapy planning CT, as per routine clinical practice, to correspond to the macroscopically manifested malignancy based on CT and MRI (contrast-enhanced T1, T2 FLAIR), a rigid registration between ADC maps and the planning CT images was performed to register the GTV structure on the ADC images. A Poisson linear quadratic (LQ) TCP model (with

radiosensitivity parameters of $\alpha = 0.12\text{Gy}^{-1}$, $\beta = 0.015\text{Gy}^{-2}$ [191]) was used to calculate the three-dimensional (voxelated) TCP maps that correspond to the cell density distributions within the GTVs, as determined from the corresponding ADC maps. Those GTV regions with TCPs in the lowest quartile of the TCP range for each patient were designated as the GTV sub-volumes with a higher risk for recurrence after radiotherapy and labeled as the biological target volume (BTV). The BTV dose was escalated using a simultaneous integrated boost (SIB) aiming to increase the TCP within the BTV to the median TCP value for each case in turn. The SIB dose itself was defined, which is required to achieve this objective for each case individually. Finally, radiotherapy treatments were simulated using the clinical plans as a baseline and incorporating the corresponding BTVs and the associated SIB dose derived for each patient case. Dose constraints to the surrounding organs at risk (OARs) were not changed from the baseline standard clinical plans, and personalized SIB plans were created accordingly.

4.2.1 Dataset

I studied 10 patients with GBM who were treated between 2018 to 2019 with standard radical chemoradiotherapy of 60Gy in 30 fractions with concomitant and adjuvant temozolomide. This study was approved by the local ethics committee and written informed consent was obtained by the patients before their treatment. All enrolled patients had CT and anatomical MR imaging acquired before radiotherapy and used for treatment planning purposes. After segmenting the tumor-related target volumes and healthy organs at risk according to standard clinical protocols, volumetric-modulated arc therapy (VMAT) treatments were planned using the Eclipse 13.6 system to be delivered by a True Beam linear accelerator (Varian Medical Systems, Palo Alto, California). All the patients

received prior surgery and the GTV included resection cavities in all cases. The target delineation was based on European Society Radiation Oncology (EORTC) protocol. Doses in the target volume was prescribed by 60Gy in 30 fractions. The GTV was defined from the planning CT data and postoperative images from MRI fusion, and was shown as enhancing tumor and resection cavity on contrast-enhanced T1 weighted MRI. Some tumors may be better visualized on the MRI T2 FLAIR images. The CTV was GTV + 2cm. The volume was trimmed at the bony circumference, tentorium and midline, unless there was a clear route for tumor spread such as the corpus callosum. The PTV was CTV + 0.3cm. DW-MRI was acquired on a 3T scanner (Magnetom Verio, Siemens Medical Systems, Erlangen, Germany) with an echo-planar (EPI) sequence using b -values of 400, 800 and 1000 s/mm^2 as the average diffusion values along three orthogonal axes, repetition times (TR) between 4600s to 13300s, echo time (TE) = 72-95s, flip angle = 90, GRAPPA accelerator factor = 2 and EPI factor = 132. ADC maps were computed using all b -values, with a voxel size of $1.2 \times 1.2 \times 6.5 mm^3$. For the enrolled patients, quantities summarizing dose distributions in the GTV volumes are given in Table 4.1.

Table 4.1 Patients characteristics in terms of dose and gross tumor volume (GTV). D2% means the dose received in at least 2% of the GTV; D50% means the dose received in at least 50% of the GTV; D95% means the dose received in at least 95% of GTV; and D98% means the dose received in at least 98% of the GTV.

Patient	GTV volume(cm^3)	Min Dose (Gy)	Max Dose (Gy)	D2%(Gy)	D50%(Gy)	D95%(Gy)	D98%(Gy)
1	106.3	60.12	62.88	62.52	61.68	60.78	60.6
2	5.7	60.12	62.22	61.86	61.26	60.60	60.48
3	16.7	62.52	63.72	63.64	63.37	63.00	62.92

4	82.1	56.22	65.46	63.35	61.10	60.01	59.73
5	57.6	60.00	62.82	62.28	61.50	60.66	60.54
6	82.0	59.22	63.66	61.68	60.84	60.30	60.16
7	82.9	59.70	63.18	62.22	61.62	66.36	60.72
8	42.6	59.82	64.56	64.07	63.03	61.66	61.32
9	45.5	59.82	64.74	64.20	62.34	60.66	60.36
10	95.3	59.88	66.18	65.04	63.24	61.50	61.20

4.2.2 Cell Density Map

The DWI-derived ADC maps were related to the cell density of the corresponding volume element (voxel). To achieve this, ADC maps were registered to the planning CT scans using rigid registration to anatomical landmarks, *e.g.*, the skull. The voxel size of each CT image is $0.926 \times 0.926 \times 3.000$ mm³. The matrix size for the patient data was $192 \times 192 \times 19$ voxels for the ADC and $512 \times 512 \times 99$ voxels for the CT images, respectively. The NiftyReg software [226] was used to register ADC maps on CT images by resampling ADC voxels using trilinear interpolation in order to match with the CT grid, leading to a $512 \times 512 \times 99$ ADC map. On each CT-ADC registered image plane, cell densities in the matrix of $512 \times 512 \times 99$ are calculated. As mentioned in Section 4.1, there are several studies indicating that there is an inverse correlation between ADC and cell density. Eidel *et al.* [223] included the most GBM specimens and quantified the relationship between ADC and cell density for GBM, as is shown in Figure 4.1. These data can be fitted linearly using the following formula:

$$\text{Cell density } (\rho) = -2.3 \times \text{ADC} + 5889.6, \quad (4.1)$$

where the coefficients are derived by the linear fit strategy. Equation 4.1 was also used to calculate the cell density from the ADC values for patient data in this chapter. Pixels with ADC values from 460 to 1660 mm^2/s to indicate malignancy are considered according to recent studies [227]–[230].

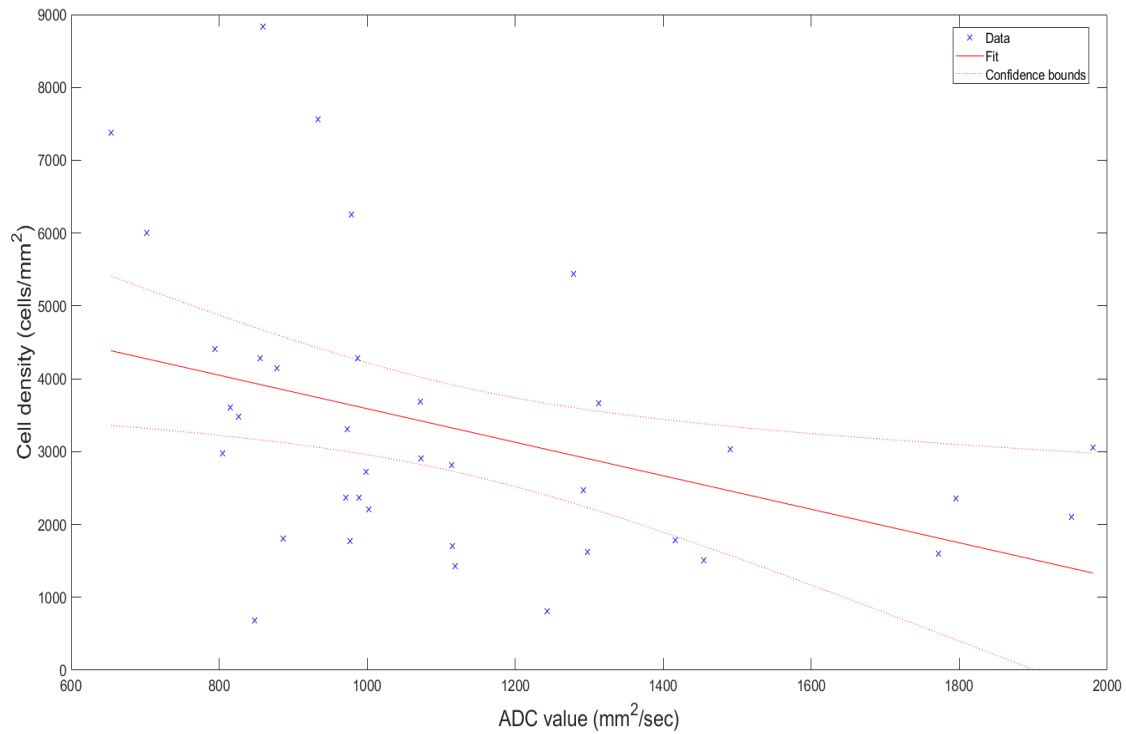


Figure 4.1 Cell density and the corresponding ADC values derived by Eidel *et al.* [181], where the line represents a linear fit performed herein using Equation 4.1, Pearson’s $r = -0.40$, Spearman’s $R_s = -0.48$, and both with p -values less than 0.01. r within $\pm 0.40 - \pm 0.69$ represents a moderate correlation.

4.2.3 TCP Map

A linear-quadratic (LQ) TCP model defined in Equation 4.2 is used to calculate TCP_i values, which is the TCP value of each element in each layer. N_i is the number of tumor

cells per voxel; D_i is the voxelated total treatment dose; d_i is the voxelated dose per fraction; n is the number of fractions; α and β are tissue radiobiological parameters chosen as $\alpha = 0.12 \text{Gy}^{-1}$, $\beta = 0.015 \text{Gy}^{-2}$ [191]; ρ_i is the cell density in the area (A) of $0.926 \times 0.926 \text{ mm}^2$ calculated in Section 4.2.2.

$$\begin{aligned} TCP_i &= \exp(-N_i \exp(-(\alpha + \beta d_i) D_i)) \\ &= \exp(-\rho_i A \exp(-(\alpha + \beta \frac{D_i}{n}) D_i)) \end{aligned} \quad (4.2)$$

The above equation can be used to calculate the TCP_i for a given cell density at each pixel (ρ_i), with the latter derived from the ADC maps. Repeating for all pixels in the ADC image produces a volumetric (3D) TCP map for the available data.

4.2.4 Biological Tumor Volume and Simultaneous Integrated

Boost

The aforementioned TCP map is used to define biological target volume (BTV), where the dose will be escalated by means of a simultaneous integrated boost (SIB), that is increasing the dose per fraction whilst maintaining the same number of fractions (*i.e.*, 30). I calculated the voxelated TCP values in the GTV, and defined the BTV as the volume in which the TCP values are in the lowest 25% of the calculated TCP range for that patient. Each patient's SIB dose is calculated such that the minimum TCP in the BTV (defined as TCP_{low}) is increased to match the median TCP value of the whole tumor (defined as TCP_{high}).

According to Equation 4.2, TCP_{low} and TCP_{high} are written as:

$$TCP_{low} = \exp(-\rho_1 A \exp(-(\alpha + \beta \frac{D_1}{n}) D_1)), \quad (4.3)$$

$$TCP_{high} = \exp(-\rho_2 A \exp(-(\alpha + \beta \frac{D_2}{n}) D_2)), \quad (4.4)$$

where ρ_1 is the cell density corresponding to TCP_{low} and ρ_2 is the cell density corresponding to TCP_{high} . D_1 and D_2 are voxelated doses known from the dose distribution in TPS, which yielded TCP_{low} and TCP_{high} , respectively. Since the escalated dose (D_{SIB}) is used to increase the TCP_{low} with cell density ρ_1 to the TCP_{high} , then TCP_{high} can be expressed as

$$TCP_{high} = \exp(-\rho_1 A \exp(-(\alpha + \beta \frac{D_{SIB}}{n}) D_{SIB})). \quad (4.5)$$

Taking the logarithm of both sides of the Equation 4.5, it leads to

$$\log \frac{\log TCP_{high}}{-\rho_1 A} = -\frac{\beta}{n} D_{SIB}^2 - \alpha D_{SIB} \quad (4.6)$$

In the Equation 4.6, α , β , ρ_1 , A , n and TCP_{high} are all known, therefore, the escalated dose (D_{SIB}) can be calculated by solving this one-variable quadratic function. Taking Patient #1 as an example, the original prescription dose is 60Gy in 30 fractions. TCP_{low} is 70.18% in the BTV, and TCP_{high} is 80.76% in the GTV. Use of Equation 4.6 allows us to calculate SIB dose to be 66.6Gy in 30 fractions.

4.2.5 SIB Isotoxic Dose-escalated Treatment Plans

The SIB isotoxic dose escalation plans were performed on the Varian Eclipse treatment planning system with the VMAT technique, which is used for the original clinical plans. Then, BTV was generated in the TPS for each patient following the proposed method in

Section 4.2.4. The radiation dose to the area of PTV excluding BTV was still 60Gy in 30 fractions. In BTV, the same number of fractions are used, and radiation was delivered as a simultaneous integrated boost with the personalized SIB dose on a case-by-case basis. Mirroring the original clinical plans, the dose-volume optimization objectives for the target and OAR constraints are given in Table 4.2. In our SIB plans, we typically limit the maximum dose (Dmax) to the optic chiasm to <55Gy for the majority of patients in our cohort. However, for patients with tumors situated in close proximity to the optic chiasm, we have chosen to set a slightly higher limit of Dmax<60Gy to ensure adequate toxicities of optic chiasm without compromising the tumor control. To confirm the feasibility of SIB isotoxic dose escalation plans, I evaluated whether the dose in BTV and PTV achieves the requested dose levels, and whether the dose in OARs stays within their tolerance when changing the dose prescription. Once the SIB isotoxic dose escalation plans have been approved by an oncologist, a new dose distribution map was generated. Combined with the cell density map mentioned in Section 4.2.2, a new TCP map was generated. The SIB isotoxic dose escalation plans were compared to the clinical delivered plans with respect to TCP maps. I can then demonstrate how TCP growth behaves in TPS. Figure 4.2 shows the step-by-step operation of the proposed SIB isotoxic dose escalation.

Table 4.2 Critical organs tolerance doses and target dose requirements for GBM [15], [33], [42], [187].

Critical organs / targets	Tolerance doses	Toxicities
Optic chiasm	Dmax 55 Gy	Radiation induced optic neuropathy (RION) negligible

	Dmax 55–60 Gy	RION 3-7%	
	Dmax 60Gy	RION 7-20%	
Optic nerves	Dmax 54Gy		
Lens	Dmax 6Gy	<1% risk cataract	
	Dmax 10Gy	50% risk of cataract	
Retina	Dmax 45 Gy		
Brain stem	Dmax 54Gy to entire brain stem.		
	Absolute volume receiving 59Gy (aV59) $\leq 10\text{cm}^3$	Risk < 5% of brainstem necrosis or neurologic toxicity	
	A point ($\ll 1\text{cc}$) $\leq 64\text{Gy}$		
Target	D99%	$\geq 90\%$ of prescription dose	\
	D95%	$\geq 95\%$ of prescription dose	
	D50%	$\geq 100\%$ of prescription dose	
	D5%	$\leq 105\%$ of prescription dose	
	D2%	$\leq 107\%$ of prescription dose	

4.3 Results

In this section, ADC values of each patient enrolled in this study was first presented. The cell density at the voxel level and number of tumor cells was then calculated based on ADC values. Combing the cell density map and TCP distribution, BTV and SIB doses

were derived. Finally, the results showed that delivering the SIB dose to BTV for individual patient can achieve higher TCP values with the acceptable dose to OARs.

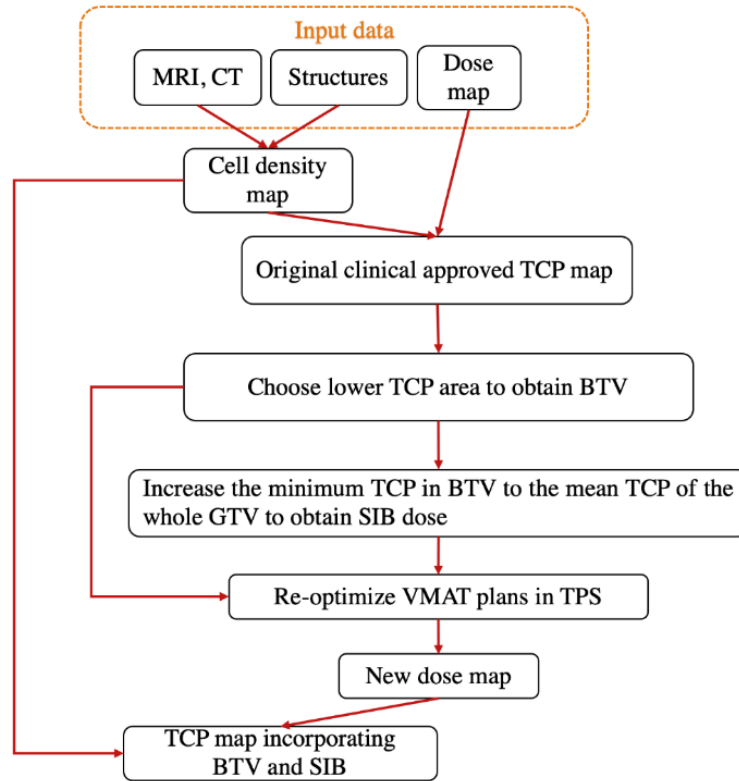


Figure 4.2 A flow chart of the proposed method to obtain escalated SIB isotoxic dose.

Figure 4.3 shows the ADC distribution within the GTV for the 10 patients. Figure 4.4 shows the BTV, and SIB doses calculated for the patient referred in Section 4.2.4 as an example case. Figure 4.4(a) shows a “slice” (axial-plane distribution) of the patient’s ADC map with the corresponding GTV (red line) outlined on the CT images and transferred as a result of the ADC-CT image fusion. Figure 4.4(b) shows the corresponding cell density map, calculated using Equation 4.1, as described in Section 4.2.2. The red and blue colored areas correspond to GTV regions with the higher and lower cell densities, respectively. Using Equation 4.2 in Section 4.2.3, the corresponding TCP map can be derived, which is shown in Figure 4.4(c). For this patient, the TCP ranges

from 0.7018 to 0.9258 with a median of 0.8076. Areas with TCP values between 0.7018 and 0.7578 correspond to the lowest quartile, and were used to define the BTV, as shown in Figure 4.4(d), where ADC values range from 478 to 783 mm²/s. Given the calculated TCP values, the SIB dose (D_{SIB}) was calculated as 66.6Gy using Equation 4.6. The SIB isotoxic dose escalation plans were then performed on the Varian Eclipse dose planning system with the VMAT technique. The radiation dose to the area of PTV excluding BTV was still 60Gy in 30 fractions. After boosting the SIB dose to BTV, the dose map of this layer was shown in Figure 4.4 (e) for this patient. The TCP map of the same layer after SIB isotoxic dose escalation planning was shown in Figure 4.4 (f).

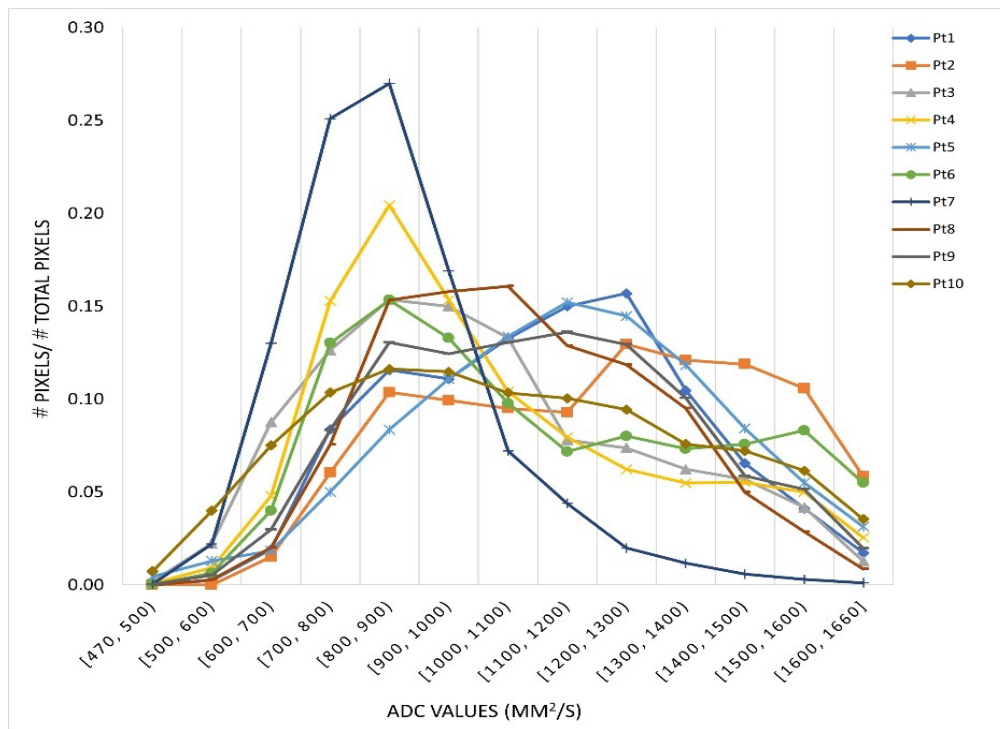
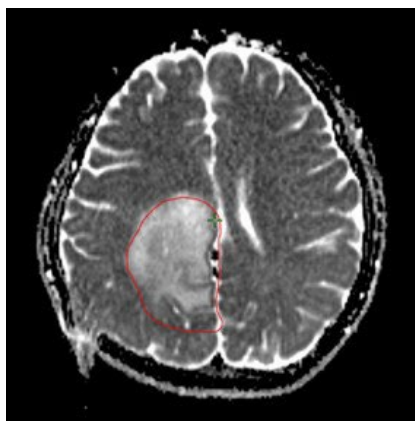
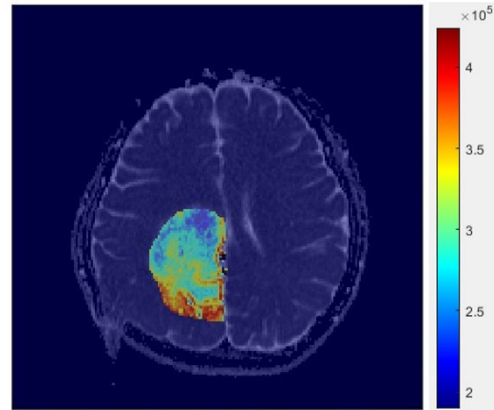


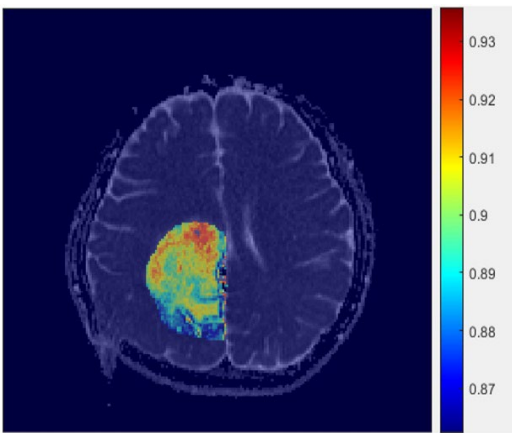
Figure 4.3 Frequency distribution histogram of the ADC values within GTV for 10 patients, where x -axis represents the ADC levels and y -axis represents the proportion of each ADC level.



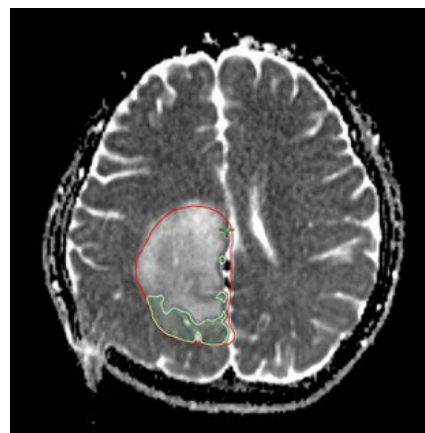
(a) ADC map with the GTV (red line).



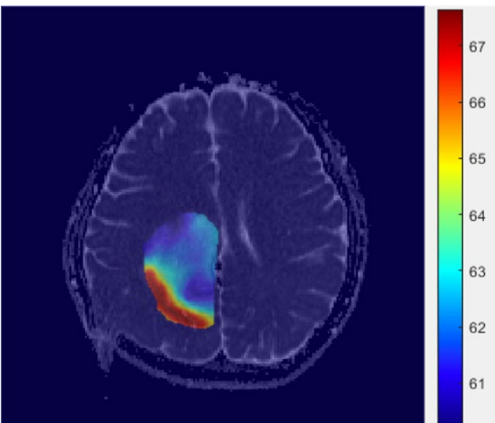
(b) Cell density map (unit: cells/mm²).



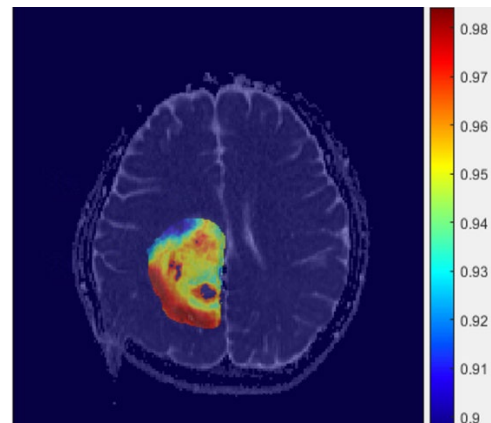
(c) TCP map.



(d) BTV (green contour) on ADC.



(e) Dose map after boosting dose to BTV



(f) TCP map after boosting dose to BTV

Figure 4.4 Stepwise analysis to deduce BTV and SIB doses on the same axial plane of the example patient: (a) ADC image and outlined GTV, (b) the calculated cell density, (c)

the TCP that corresponds to the clinical dose distribution (60 Gy in 30 fractions), (d) the derived BTV, (e) boosted dose distribution and its corresponding TCP map (f).

The histogram distribution with the TCP values from all voxels in the clinical plan (prescribed dose 60Gy, no SIB), for this patient is shown in Figure 4.5 (blue bars). This is produced by the accumulation of maps as per Figure 4.4(c), from all “slices” of the complete 3D image dataset. The TCP values that correspond to the SIB plan are shown in Figure 4.5, orange bars. Comparing the corresponding TCP values of the clinical plans (no SIB) and the SIB, the latter TCP has increased from values ranging between 70.18% and 92.58% to between 87.92% and 99.20%, respectively (Table 4.3, patient 1). Although the treatment objective is to increase doses only within BTV, there is an unavoidable dose increase to the adjacent voxels, because of a finite dose gradient governed by the laws of physics. Therefore, the dose is increased in larger area than the BTV, thereby elevating the TCP in a wider area within the gross tumor volume.

The corresponding results for the ten patients in the cohort is shown in Table 4.3, which also shows the ADC values in GTV and BTV, number of tumor cells, boost doses (*i.e.*, D_{SIB} minus the original prescription dose) and median voxelated TCP increases in clinical dose distributions. The maximum median voxelated TCP increase achieved is 16.84%. Considering the confidence interval in the relationship between ADC values and cell densities, as shown in Figure 4.1, the corresponding SIB doses and TCP ranges have been calculated, and presented in Table 4.3. The volume of BTVs for each patient was shown in Table 4.4. Since BTVs represent high cell density area, we further investigate how much of the relapsed volume overlaps with BTVs. In Table 4.4, Patient #1 relapsed three years after radiotherapy, where this patient’s BTV is 17.31 cm³, and the recurrence area

within the BTV is 10.80 cm³, accounting for 62.39% of the BTV. As for the other nine patients, one patient was died, four patients' status are lost to follow-up, two patients have not progressed, three patients relapsed but two of them went to other medical centers, therefore, their recurrence datasets are not available.

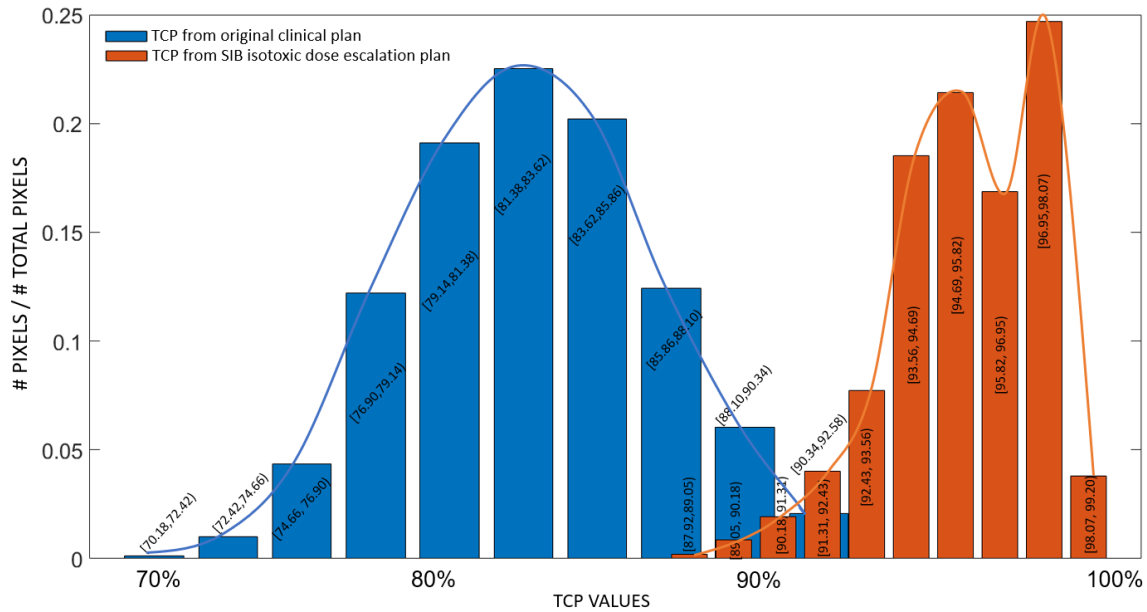


Figure 4.5 TCP distributions with and without using the proposed method, where x -axis represents the TCP levels and y -axis represents the proportion of each TCP level. Blue bars represent the TCP values from all voxels in the clinical plan for this patient, while orange bars represent TCP values that corresponds to the SIB escalated dose to the BTV.

Table 4.3 Results of proposed method for 10 GBM patients.

Patient	ADC in GTV (mm ² /sec)				Number of tumor cells	ADC in BTV (mm ² /sec)	Boosted dose (Gy)	Median voxelated TCP increase (%)
	min	max	mean	std				TCP without BTV V.S. TCP incorporating BTV and SIB dose
1	478	1660	1211.05	236.20	2.88E+10	478-783	6.60 ^a [6.23, 6.89] ^b	13.77 ^a [12.08, 16.09] ^b

2	624	1656	1201	268.93	1.23E+09	624-885	3.60 [3.25, 3.67]	7.19 [6.52, 9.61]
3	493	1660	1011	265.39	5.01E+09	493-794	6.60 [6.21, 6.68]	7.90 [7.12, 10.58]
4	475	1660	1021.8	266.66	1.30E+10	475-689	7.19 [6.83, 7.43]	8.56 [7.95, 11.90]
5	472	1660	1150.8	248.81	1.39E+10	472-798	3.90 [3.40, 4.13]	7.57 [7.25, 11.08]
6	495	1660	1096.8	294.85	1.31E+10	495-813	16.80 [16.28, 18.41]	8.90 [7.98, 11.76]
7	482	1657	856.61	166.92	2.98E+10	482-785	8.02 [7.78, 8.40]	13.64 [12.65, 19.46]
8	512	1657	1075	222.99	7.88E+09	512-806	13.20 [12.97, 13.62]	7.24 [6.96, 10.50]
9	488	1660	1106.6	247.29	1.07E+10	488-808	8.70 [8.31, 8.98]	8.07 [7.63, 11.39]
10	470	1660	1061.7	299.18	2.26E+10	471-797	10.20 [9.88, 10.53]	16.84 [15.46, 23.36]

^a: Values shown at this position for patients 1-10 indicate the SIB dose and TCP increase derived from Equation 4.1.

^b: Ranges shown at this position for patients 1-10 indicate the SIB dose and TCP increase derived from the confidential bound in Figure 4.1.

Table 4.5 shows the comprehensive OAR dose-volume statistics for the original clinical plan (labeled “old”) and the one with the SIB isotoxic dose escalation plan (labeled “new”) for each patient. The radiation dose to OARs did not exceed their tolerances, which are shown underneath each OAR. This demonstrates that the generated SIB doses assigned in BTV, should keep the toxicity to the surrounding OARs to levels that are deemed acceptable as per routine clinical practice. For patients #2, #5 and #6, the doses to brainstem in the SIB plan are less than those in the original clinical plan. This makes

sense because in the treatment planning optimization procedure, the brainstem was given higher priority than the original clinical plan to not exceed the objective values.

Table 4.4: The volume of BTVs for each patient.

Patient	GTV volume (cm^3)	BTV volume (cm^3)
1	106.3	17.31
2	5.7	0.4
3	16.7	3.63
4	82.1	6.27
5	57.6	1.82
6	82.0	20.50
7	82.9	5.30
8	42.56	8.14
9	45.48	2.82
10	95.25	8.24

I also investigated the correlation between the TCP increase and the original TCP values, as well as the number of tumor cells. In Figure 4.6(a), x -axis represents the minimum voxelated TCP values, and y -axis represents the TCP increase for the whole tumor. It shows a negative correlation between TCP increase and original TCP. It indicates that patients with the worse prognosis (*i.e.*, lower original TCP) will have a higher potential for TCP increases using the proposed method. In Figure 4.6(b), x -axis represents the number of tumor cells, and y -axis represents the TCP increase for the whole tumor. It shows a positive correlation between the number of tumor cells and the TCP increase, indicating that tumors with a larger number of cells will benefit more in terms of TCP increases.

4.4 Discussions

For GBM, some studies employed quantitative imaging techniques, such as positron emission topography (PET) and magnetic resonance spectrum imaging (MRSI) to define the high-risk areas [86-91]. Since tumor cell density is known as an important factor to determine the treatment outcome [134]–[136], diffusion-weighted magnetic resonance imaging (DW-MRI) can be used to allow us to measure in vivo the density of cells inside the body [132], [133]. This chapter presented the first DW-MRI based dose painting method by investigating the voxel-level cell density for newly diagnosed GBM.

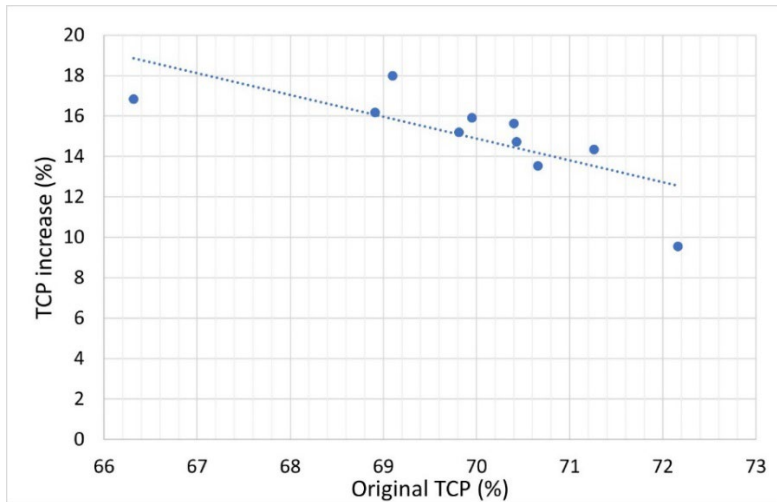
This study used ADC values derived from quantitative imaging DW-MRI as imaging biomarkers, following the observation that lower ADC values indicate higher cell density [223]. I then built an MRI-based TCP model to develop a personalized ADC-based dose painting for GBM. Since higher doses increase tumor cell kill [214], [215], through escalating the dose to personalized levels by means of a SIB to each patient's BTV, an up-to 16.84% increase of TCP has been achieved for the patient cohort, without exceeding the dose tolerance of the OARs. The proposed method increased doses by 6%-28%, *i.e.*, 63.60Gy-76.80Gy, among the patient cohort, in the area within the tumor with the high cell density. I remark that most of patients in current clinical trials have been prescribed with over 70Gy and even 79.4Gy for GBM RT. Such dose escalations were well tolerated, as summarized in Table 2.6 and Table 2.7 in Section 2.2. The optimized dose levels presented herein work accordingly with the reported GBM clinical trials.

Table 4.5 Doses of the OARs for the ten patients, expressed in terms of maximum doses in optic nerves, optic chiasm, eyes and lens and D0.1cc in brainstem. The dose tolerance indicated by the QUANTEC or RTOG 0825 protocols for those organs are also presented.

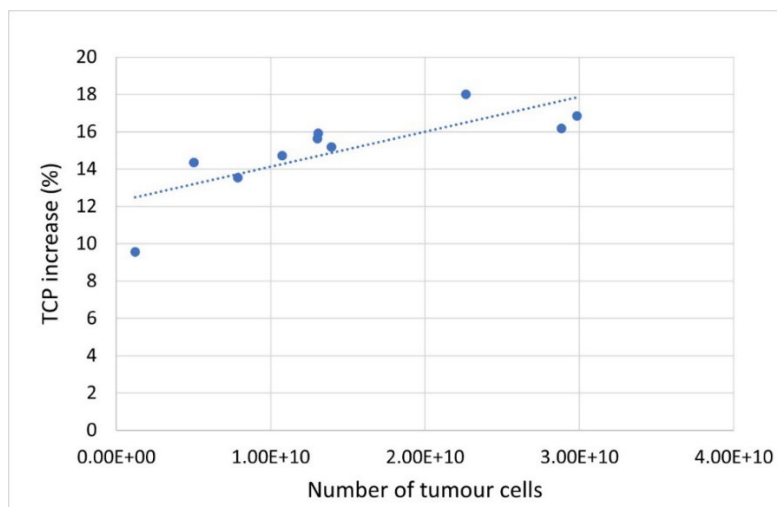
Patient	Brain Stem	Optic Nerve Left		Optic Nerve Right		Optic Chiasm		Eye globe Left		Eye globe Right		Lens Left		Lens Right	
		D0.1cc≤5Gy	Dmax≤50Gy	Dmax≤50Gy	Dmax≤50Gy	Dmax≤55Gy	Dmax≤55Gy	Dmax≤45Gy	Dmax≤45Gy	Dmax≤45Gy	Dmax≤45Gy	Dmax≤10Gy	Dmax≤10Gy	Dmax≤10Gy	Dmax≤10Gy
1	53.44	53.19	12.23	14.64	14.72	16.63	19.31	21.30	9.70	14.01	15.16	16.72	7.27	7.18	7.18
2	24.74	5.12	3.33	2.62	2.78	1.43	5.72	2.78	16.04	6.44	14.42	4.93	3.04	1.22	3.69
3	7.28	6.89	2.31	2.43	2.70	2.76	3.47	3.60	1.96	2.06	2.05	2.60	1.07	0.95	1.13
4	57.00	51.66	21.43	23.91	52.63	45.93	54.37	49.10	13.17	13.83	25.58	28.45	6.25	4.05	6.84
5	56.00 ^b	54.82	46.93	34.31	33.67	32.93	52.61	53.98	23.50	23.10	21.04	20.56	8.33	5.87	8.21
6	53.85	50.30	11.67	12.26	18.54	14.33	40.32	33.98	54.48	44.42	60.91 ^b	44.03	7.92	8.31	7.10
7	53.92	51.95	31.06	29.36	22.56	25.74	46.07	49.88	18.95	17.01	16.58	24.30	6.85	4.02	6.78
8	6.12	7.10	2.45	2.35	2.14	2.16	4.38	4.20	5.68	5.26	2.95	2.11	1.66	1.36	1.51
9	54.06	51.73	28.38	28.35	52.85	48.46	53.46	54.82	13.97	24.15	24.63	29.46	7.26	4.52	7.65
10	3.48	4.52	1.30	1.83	1.28	1.57	1.91	2.67	1.21	1.78	1.11	1.30	0.69	0.85	0.73

^a old: standard clinical plans; new: SIB plans, where the doses were calculated by Equation 4.1.

^b In the original clinical plans, radiation doses to the brainstem of patient 5 and the eye globes of patient 6 exceeded their tolerance, which would not be clinically acceptable. However, in our proposed SIB isotoxic dose escalation plans, all OARs are within their tolerance.



(a) TCP increases per patient by the dose painting prescriptions vs. the TCP from the original clinical GTV dose (60Gy). *x*-axis represents the minimum voxelated TCP values, and *y*-axis represents the TCP increase for the whole tumor.



(b) TCP increases per patient resulting from the optimized dose painting prescriptions vs. the number of tumor cells in GTV. *x*-axis represents the number of tumor cells, and *y*-axis represents the TCP increase for the whole tumor.

Figure 4.6 Relationships between TCP increases and the original TCP, and the number of tumor cells, respectively.

Other ADC-guided dose painting studies have been conducted for patients with head and neck or prostate cancer [155], [161], [164]. Gronlund et al. [231] proposed an optimization method via the dose painting for prostate cancer, where the mean dose after optimization equals the original prescription dose. This redistributes the dose over the entire tumor, resulting in some areas getting a lower dose than what was originally prescribed [231]. This method may not be suitable for GBMs or other tumors with poor prognosis, because decreasing the dose in the high TCP areas may reduce the overall TCP, resulting in unfavorable outcomes.

To our knowledge, the only approach using ADC-based dose painting for GBM was published by Orlanri *et al.* [232]. However, their study was designed for recurrent GBM, not for newly diagnosed GBM [232]. Their optimized prescription dose was only related to ADC values, however, the number of tumor cells was not considered. In addition, even though many dose painting studies used logistic TCP models, which have not elucidated the mechanistic interpretations about the dose-response of cell survival, the tumor cells repair related to the dose-response of cell survival is not considered. Since the number of tumor cells and tumor cells repair (*i.e.*, radiation sensitivity factors α and β) have been incorporated in linear-quadratic (LQ) TCP models [191], [233], a generalized version of the LQ TCP model was used, with parameters (α and β) corresponding to GBM in this study for planning RT in a personalized way to improve treatment outcomes. I remark that the developed formalism could be used widely and transferable to calculations using different TCP parameters for specific types of tumors, different formulations (*e.g.*, including cell repopulation), or even different TCP models corresponding to a different endpoint (*e.g.*, time to progression). Moreover, the proposed approach, albeit utilizing a generalized TCP model, allows for personalized RT, since the level of dose escalation

differs between patients. The values of radiation sensitivity parameters α and β used in this study were derived from clinical trials and were smaller than from in vitro biological experiments. As mentioned in Section 2.1.3.2, lower values of α may cause the overestimation of doses. Nevertheless, the surrounding OARs did not exceed their tolerances. Furthermore, the radiosensitivity parameters derived from clinical trials is more practical than the α obtained from in vitro biological experiments.

In contrast to what have been done in other studies, this study combined ADC maps with the voxelated TCP map to achieve the personalized SIB isotoxic dose escalation for GBM. DW-MRI is a well-established method to characterize oncological lesions in terms of cellular density by means of ADC. The inclusion of this information at the cellular level in TCP models can increase the accuracy of tumor control prediction, paving the way towards personalized and optimized treatments.

Since the original prescription dose was the same for each patient, the main factor contributing to TCP is the number of tumor cells. Therefore, for patients with a higher number of tumor cells, a lower TCP is expected. From the results shown in Figure 4.6, the trendline shows that patients with a higher number of tumor cells can lead to a higher TCP increase. This indicates that patients with higher disease burden and worse original prognosis would benefit more from the proposed method.

We remark that the selection of b -values used in DW-MRI leads to a potential bias in ADC values. However, ADC maps of the patients cohort were provided by the hospital, where b -values were chosen as 400, 800, 1000 s/mm^2 , and directly employed in the proposed method. The ADC to cell density translation is based on data from Eidel *et al.*

[181]. The 95% confidence interval between ADC values and cell density has been analyzed in Figure 4.1. Taking this confidence interval into account, boosted dose ranges and TCP ranges have been discussed in Table 4.3. It is noted that uncertainties related to ADC quantification and cell density derivation, could affect the values of TCP. However, this should not affect the main findings of the proposed method because only relative TCP values are employed in the proposed method, moreover with the lowest quartile of the TCP range to define the BTV, where the dose would be escalated to increase the overall TCP.

Nakagawa *et al.* [77] and Fitzek *et al.* [211] conducted clinical trials and their results showed that escalated radiation doses to the whole PTVs did not improve survival for GBM patients. This was because toxicity was increased due to higher doses to OAR and normal tissues, caused by escalating the dose to the whole tumor. A novel method was proposed in this chapter to produce voxel-level TCP maps based on voxel-level cell density analysis, where boosted doses are assigned into tumor area with lower TCP values (*i.e.*, area with higher cell density) for overall tumor control improvement, whilst keeping the doses to OARs and normal tissues within the established tolerance levels as per the routine clinical practice.

However, one limitation of this study lies in lack of clinical trials to verify whether our proposed method can actually increase the prospects for GBM patients. It is foreseeable that the proposed method can be used for the design of clinical trials. As for the recurrence of the data set, most of patients' outcome data are not available due to the patients being treated at a centralized oncology center, with their ongoing care managed by different

teams. We are going to continue enrolling more recurrence GBM patients with DW-MRI, to investigate the correlation of progression regions with pre-radiotherapy ADC values.

In this work, the dose was escalated uniformly to the high risk volume, *i.e.*, BTV, following the concept of dose painting by contours (DPBC). However, our methodology lends itself to dose painting by numbers (DPBN) techniques, each voxel with low TCP values can be assigned to a corresponding escalated dose, leading to better matching of the escalated dose distribution to the high risk voxels for further TCP increase. To the best of our knowledge, there are no commercial treatment planning systems (TPS) facilitating the planning of DPBN. We will study this in the future.

Given that some early-stage trials showed promising outcomes using proton therapy for GBM patients compared with photon therapy [234]–[236]. It is expected that proton therapy has the potential to widen the therapeutic window compared with photon therapy and can be considered as an interesting radiation modality for dose painting. In the next chapter, I will investigate the potential to further increase TCP values by applying our proposed method using proton beam therapy (PBT), since PBT, which may offer more headroom for SIB dose-escalation due to the decrease in integral dose outside the target.

4.5 Conclusions

This study used ADC-driven SIB dose painting to escalate the dose to a certain area in the GTV for GBM patients. The results showed that TCP increases can be achieved without exceeding the baseline OAR tolerances. Patients with higher number of tumor

cells, in other words, lower TCP, showed a higher potential for TCP increase with this methodology. In addition, ADC has been demonstrated as an imaging biomarker with a higher cell density for the selection of patients and is able to guide the escalation of the dose in a personalized way. In the next chapter, I will investigate the potential to further increase TCP values by applying the proposed method using proton beam therapy (PBT), since PBT offers more headroom for SIB dose escalation due to the decrease in integral doses outside the target.

Chapter 5

Proton Dose Painting for GBM

5.1 Introduction

The previous chapter has discussed RT treatment intensification protocols using radiation dose painting to increase the treatment efficacy for patients with GBM, and optimized the tumor control for patients with GBM. An increased dose was given to specific areas defined by biomarkers from functional images within the tumor for personalised photon radiotherapy, leading to an increase in TCP, and the dose of OARs did not exceed their dose limits. In comparison to photon radiotherapy, proton therapy can deliver a much less dose to healthy tissues around the tumor due to its characteristic “Bragg” peak [166]. The danger of radiation damage to surrounding healthy tissues can be reduced. Early-phase trials showed promising outcomes using proton therapy for brain tumor patients compared with photon therapy [5], [234]. Studies have shown that low organ at risk (OAR) doses are achievable in GBM proton plans, while maintaining the same dose level to the target as that in photon therapy [235]–[237]. Consequently, use of proton radiotherapy enables us to achieve a higher therapeutic ratio.

In order to escalate the dose to regions of presumed high risk of local failure, dose painting techniques have been employed in proton therapy, where a non-uniform dose is prescribed within the clinical target volume [238] [239]. Gondi *et al.* have conducted a

clinical trial for proton dose painting (NRG BN001) for GBM [240]. This trial still needs to accrue patients, and the corresponding results have not been announced yet. Some hypotheses from this trial suggested that the increased conformality of proton therapy may result in fewer toxicities, particularly related to lymphopenia which is associated with overall survival in GBM [240]. Gondi *et al.* escalated the dose of 75Gy to the GTV area and remained the standard dose (60Gy) to the rest of the tumor target [240]. However, this dose painting approach delivered the boosted dose to the GTV area, which was contoured on the contrast-enhanced T1-MRI. Such conventional anatomical imaging techniques cannot provide sufficient biological information of tumors. To address this, quantitative imaging such as multi-parameter MRI can be employed to define the high-risk areas, thereby guiding a precise dose escalation to tumor targets.

I have investigated how to combine DW-MRI imaging with radiobiological models for GBM dose painting. The ADC map from DW-MRI imaging was applied as an imaging biomarker to calculate cell density. Thereafter, the cell density was employed to calculate TCP maps for each patient, and the TCP value was used as a metric to guide the boost area and the dose boost level in the escalation RT for personalized treatment. Mirroring the principles introduced for personalized photon dose painting radiotherapy, in this chapter, proton therapy is implemented to investigate the benefits from the proton technique, with comparisons against photon therapy in terms of target dose coverage, doses to OARs and therapeutic ratios. The same cohort of GBM patients in the previous chapter are included in this chapter for dose painting with proton. The results collected from photon plans are used as the baseline. The proposed photon dose painting and proton dose painting plans and the probabilities of tumor control of the photon and proton plans have also been analyzed. The purpose of the study is to evaluate the outperformance of

proton dose painting to meet the dosage restrictions and targets versus photon dose painting plans. Moreover, the robustness and the therapeutic ratio of proton radiotherapy has been investigated in this chapter. Proton dose painting plans are expected to reduce the non-target dose and consequently protect the healthy tissues and increase the therapeutic ratio.

5.2 Materials and Methods

5.2.1 Patients

The same patient cohort used in Chapter 4 (*i.e.*, 10 patients with GBM) were enrolled in this section, eligible for proton and photon plan comparisons. The original clinically used photon plans (non-dose-painting photon plans) were approved by the local ethics committee. The written informed consent was obtained by the patients before their treatment.

5.2.2 Photon Dose Painting Plans

The photon dose painting plans of the 10 patients were designed in Chapter 4, and the prescribed doses were 63.60-76.80 Gy (in 30 fractions, 5 days/week) to BTV (ADC avid volume with a 5mm margin), 60 Gy to PTV (gross tumor volume (GTV) with a 20mm margin). The GTVs, CTVs and PTVs were delineated according to standard protocols, and the details of the BTV delineation can be found in the previous chapter. The prescription was given as a mean dose to the targets, with the aim of reaching the prescription dose plus/minus one Gy [8]. Note that each dosage level permitted a heterogeneous dose, as

long as the 95% dose coverage was guaranteed for each target volume. The planning constraints to targets and organs at risk (OARs) are shown in Table 4.2, and the dose was normalized to 100% at target mean in BTV. In the case of overlap between BTV and the serial organs, such as brainstem, optical nerves and optical chiasma, the dose constraints to such OARs were prioritized, and then the dose was instead normalized in BTV minus such OAR volumes. Planning risk volume (PRV) expansions of 3mm were used for brainstem to ensure that dose limits were not exceeded in case of positioning errors. Plans were approved by a neuro-oncologist and a physicist in the local hospital. Planning was performed in Eclipse version 16.1 (Varian Medical Systems, Palo Alto, California). Volumetric arc therapy (VMAT) with two full arcs was used.

5.2.3 Proton Dose Painting Plans

Since the number of tumor cells is one of the important metrics to dictate the radiation doses according to the standard radiobiological theory [214], [215], the DW-MRI is employed to produce apparent diffusion coefficient (ADC) maps, which are inversely correlated with tumor cell density [223]. After the 3D cell distribution of the tumor has been derived from the ADC maps, a personalized biological model is employed to calculate the 3D tumor control probability (TCP) in the voxel level. The TCP maps can indicate which area has higher disease burden and needs an escalated radiation dose. Finally, the proton dose painting is implemented to deliver the simultaneous integrated boost (SIB) dose to the lower TCP area (*i.e.*, BTV_proton), defined as pixels for which the expected pre-boost TCP was in the lower quartile of the TCP range for each patient. An SIB dose was applied so that the lowest TCP in the BTV is increased to match the

average TCP of the whole tumor. Figure 5.1 shows the flow chart of how proton dose painting plan generates.

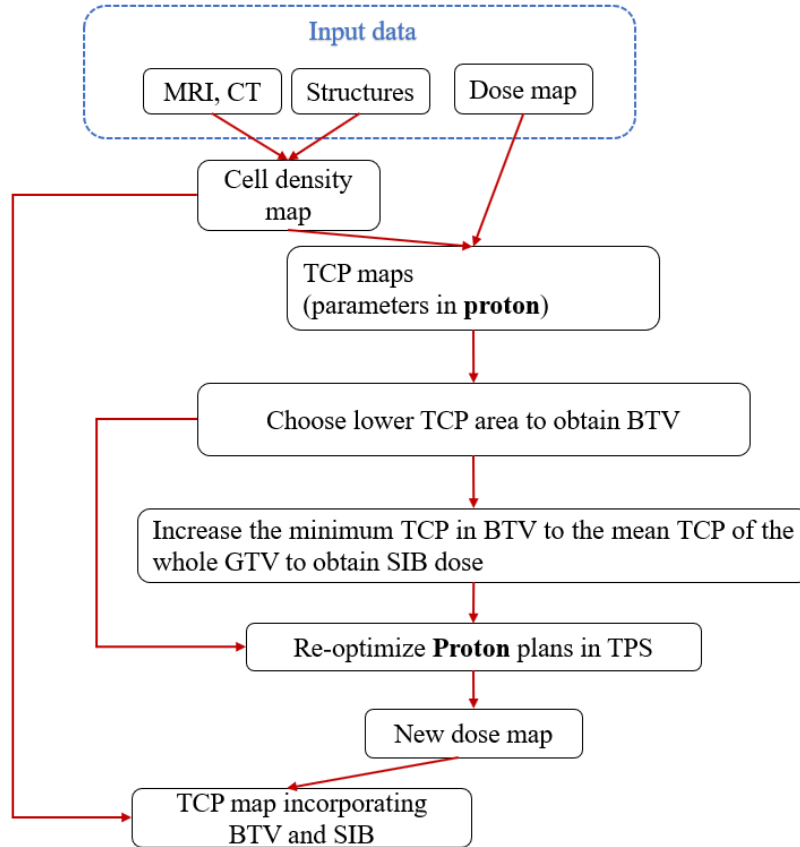


Figure 5.1 A flow chart of proton dose painting plan generation.

As for the cell density calculation, it is not impacted by treatment techniques, that is, proton RT employs the same the procedure with photon RT to calculate cell densities, since the same patient’s dataset and DW-MRI and ADC maps produced from DW-MRI are used.

As for the TCP maps, the Poisson linear-quadratic (LQ) TCP model expressed in Equation 4.2 was employed for the proton treatment. However, the tissue radiobiological

parameters are different from photon radiotherapy. In 2019, Cammarata *et al.* estimated the α and β values in proton irradiation by fitting the cell survival to the Poisson-LQ model. They found $\alpha = 0.292\text{Gy}^{-1}$ and $\beta = 0.010\text{Gy}^{-2}$ under proton radiation [241]. The BTV in proton radiotherapy (BTV_proton) is defined as the volume in which the TCP values are in the lowest quartile of the calculated TCP range for that patient. A simultaneous integrated boost (SIB) dose is then calculated to enable the minimum TCP in the BTV to be the median TCP value of the whole tumor. Equation 4.6 was applied in this chapter for the SIB dose calculation.

As for the proton plans, in this chapter, I used the pencil beam scanning technique of multi field optimization (MFO), *i.e.*, Intensity Modulated Proton Therapy (IMPT). The dose from individual MFO field can be relatively heterogeneous. To prescribe different dose levels to a tumor, the technique of MFO will be superior to single field optimization (SFO) for dose painting. However, MFO is more sensitive to the uncertainties [180], [242], [243]. As described in the Section 2.3, there are two main sources of uncertainty when performing proton plans: one is the proton range uncertainty associated with treatment planning dose calculations, the other is the positional or setup uncertainty associated with the actual patient treatment [1]. To consider both of them, the proton plans are performed with the robust optimization. The function of robust optimization is built in the TPS, *i.e.*, Eclipse version 13 (Varian Medical Systems, Palo Alto, California), using the algorithm of worst-case scenario optimization, which has been described in Section 2.3.

The proton plans were optimized according to the dose constraints suggested by QUANTEC and Emami *et al.* [37], [54]. Robust optimization on the proton plan was

performed for the target dose coverage requirements and OARs constraints. In particular, the max doses to the brainstem are used in proton plans instead of the PRVs used in the photon plans. For robust optimization in brain IMPT, $\pm 3.5\%$ range and $\pm 3\text{mm}$ setup uncertainties are recommended [244]–[246].

Patients' setup error indicates the change in isocenter position in X/Y/Z direction, *i.e.*, six different shifts (3mm, 0mm, 0mm), (-3mm, 0mm, 0mm) (0mm, 3mm, 0mm) (0mm, -3mm, 0mm), (0mm, 0mm, 3mm) and (0mm, 0mm, -3mm), and estimates how these changes in patient setup may affect the dose distribution. The range uncertainty in proton RT represents the variations in the calibration curve for the CT number to relative stopping power [247]. If the value is positive, the proton stopping power value increases and the range becomes shorter compared to the range of the nominal plan, thereby moving closer to the source. If the value is negative, the stopping power value decreases and the range moves further from the source. Hahn *et al.* studied the impact of range uncertainty on clinical LET distribution and biological effectiveness in proton therapy [248]. Combining setup and range uncertainties results in 12 dose distributions for each proton plan.

According to the aforementioned discussions, treatment planning was performed for a spot scanning technique in Eclipse, using the Nonlinear Universal Proton Optimizer (NUPO) optimization algorithm with multi-field optimization and a proton convolution superposition (PCS, version 13.7.14) volume dose algorithm. Doses were normalized to 100% at target (*i.e.*, BTV_proton) mean. The doses reported for proton plans are given in Gy. Relative biological effectiveness (RBE) is set as a constant value of 1.1 [249]. Three or four fields were used for each patient. Figure 5.2 shows a patient case as an example

for proton fields arrangement. The area around the targets, where beam spots were allowed, was laterally set to 10mm, while proximal and distal margins for beam spots were set to be 3-4mm and 6.5 mm, respectively, based on the water equivalent depth between energy layers in the direction of the beam. The body structure was expanded by 1 cm from patient skin to allow the optimizer to put spots at the surface of the patient and to improve accuracy of dose calculation to the skin. The minimum air gap between snout (including range shifter) and body structure was set to 8 cm for oblique anterior fields and 15 cm for oblique posterior fields.

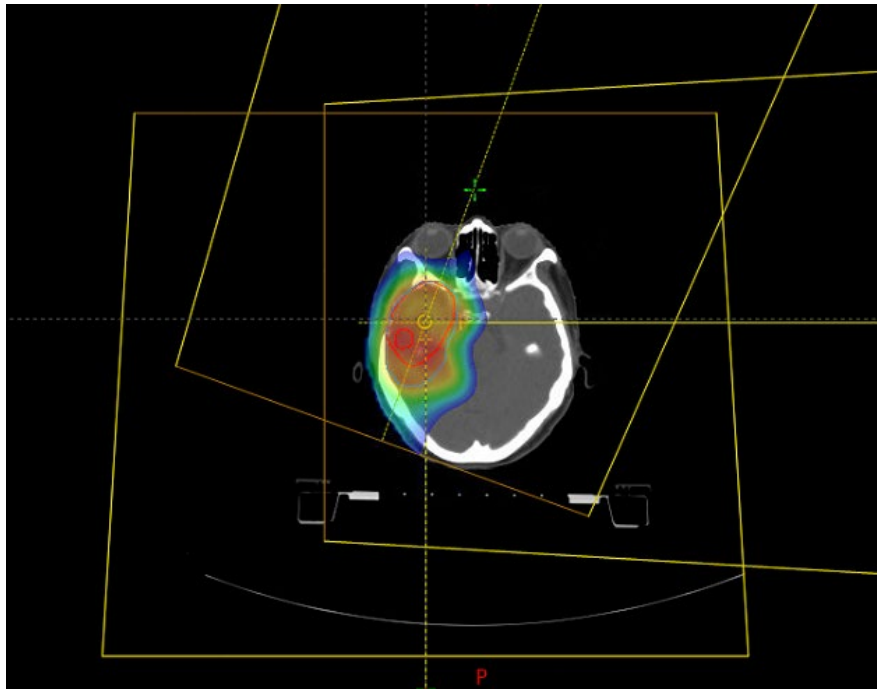


Figure 5.2 Proton fields arrangement, a patient case study. This proton plan comprises three fields: 200 degree of gantry, 270 degree of gantry with 30 degree of couch, and 50 degree of gantry with 270 degree of couch.

5.2.4 Robust Evaluation

For the robustness evaluation, the same uncertainty scenarios (*i.e.*, 3mm and $\pm 3.5\%$) in robustness optimization have been employed. DVHs were calculated for all proton plans, where 12 different uncertainty scenarios have been involved herein, *i.e.*, the range uncertainty of $\pm 3.5\%$ for proton plans and ± 3 mm setup error in three dimensions. Using a Matlab script built in-house, the robustness of each proton dose painting plan was then evaluated. I generated all potential error scenarios for both setup and range uncertainties and examined the perturbed dose distribution of the nominal plans.

Hakansson *et al.* employed the width of the DVHs variation from all uncertainty scenarios, defined as R , to evaluate the robustness of proton plans [250].

$$R = |D_{\text{highest}} - D_{\text{lowest}}| \quad (5.1)$$

where D_{highest} and D_{lowest} means the highest and lowest dose values of different dose metrics among 12 scenarios. For example, the highest and lowest value for the CTV $D_{95\%}$ among 12 scenarios is used as an indicator to compare the robustness of different plans. The smaller the value of the robustness (R) is, the lower the variation will be in DVH under uncertainty, leading to a more robust plan [181], [251].

5.3 Results

Following the proposed proton dose painting method, the SIB doses were delivered to BTV, where the high-risk area of tumor were defined by functional imaging and the TCP model. I then evaluated whether the dose in targets achieved the requested dose levels,

and how much the dose was delivered to OARs after performing proton treatment. TCP maps were then calculated by combining the dose distribution maps generated from proton dose painting plans with the cell density maps generated from ADC maps. In addition, quantitative comparisons in terms of SIB doses, TCP improvement and OAR dose levels were discussed. Finally, robustness evaluation of the proposed proton dose painting treatment has been presented.

5.3.1 SIB Doses and TCP Improvements

Table 5.1 shows the boosted doses using in proton dose painting plans, and TCP increases in both photon and proton dose painting plans, using the regression line (*i.e.*, Equation 4.1) and 95% confidence interval between ADC values and cellularity shown in Figure 4.1. We first use radiosensitivity parameters based on in-vitro biological experiments ($\alpha = 0.292$, $\beta = 0.010$) [241] to analyse proton dose painting plans (ProtonDP_{bio}). To the best of our knowledge, there appears to be a lack of proton radiosensitivity parameters from clinical trials. However, in the previous chapters, the radiosensitivity parameters for photon RT are from clinical trials. Since the typical relative biological effect (RBE) of protons relative to photons is 1.1 [1], we simply use the α and β as photon RT ($\alpha = 0.12$, $\beta = 0.015$) to further analyse proton dose painting plans with radiosensitivity parameters from clinical trials (ProtonDP_{cli}). The SIB doses derived from the regression line for ProtonDP_{cli} are from 63.60Gy to 76.80Gy, which are the same with the SIB doses for photon dose-painting plans. This is because SIB doses are defined as doses capable of improving the minimum TCP in the BTV to the median TCP value of the entire tumor. When using the same α and β values, the TCP distributions remain the same as those in the original clinical plans. The SIB doses derived from the regression line for ProtonDP_{bio}

are from 64.18Gy to 77.67Gy for the patients' cohort, which was generally higher than the SIB dose for photon dose painting plan. The TCP increases are comparable between the ProtonDP_{cli} and photon dose painting plans versus the original clinically delivered photon plans, although ProtonDP_{cli}'s are slightly inferior. This makes sense since less doses are delivered outside of the BTVs in ProtonDP_{cli} than those in photon dose painting plans due to proton's Bragg Peak. As for TCP increases of ProtonDP_{bio}, compared with the original clinically delivered photon plan, the TCP values are increased up to 34.25%. Figure 5.3 is the histogram distribution with the TCP values from all voxels in the photon (in green) and proton (in blue) dose painting plans for one patient as an example case. The purple part in Figure 5.3 indicates the TCP histogram distribution of the original clinical photon plan. For this patient, TCP values in each pixel are from 70.18% to 92.58%. Purple columns represent the TCP distribution from the original clinical photon plans. Using the proposed method, the TCP values are increased to the range between 87.92% and 99.20%, plotted in green columns. Blue columns represent TCP values in ProtonDP_{bio}, where TCP values ranging between 99.15% to 99.98%. Light blue columns represent TCP values in ProtonDP_{cli}, where TCP values ranging between 87.24% to 99.05%.

Table 5.1 Results of SIB doses and TCP increases for photon and proton dose painting plans, respectively.

Patient	SIB dose for proton dose painting ($\alpha=0.12$, $\beta=0.015$)	SIB dose for proton dose painting ($\alpha=0.292$, $\beta=0.010$)	TCP increase (%)		
			Photon dose painting ($\alpha=0.12$, $\beta=0.015$) vs. original clinical plan	Proton dose painting ($\alpha=0.12$, $\beta=0.015$) vs. original clinical plan	Proton dose painting ($\alpha=0.292$, $\beta=0.010$) vs. original clinical plan
1	66.60 ^a [66.23, 66.89] ^b	67.96 ^a [67.28, 68.49] ^b	13.77 ^a [12.08, 16.09] ^b	13.24 ^a [11.67, 15.29] ^b	17.63 ^a [15.30, 22.29] ^b
2	63.60 [63.25, 63.64]	64.18 [63.54, 64.25]	7.19 [6.52, 9.61]	6.28 [5.63, 8.27]	14.39 [14.01, 15.69]
3	66.60 [66.21, 66.68]	67.39 [66.68, 67.54]	7.90 [7.12, 10.58]	7.87 [6.89, 10.17]	13.62 [13.29, 14.77]
4	67.19 [66.83, 67.43]	68.43 [67.77, 68.88]	8.56 [7.95, 11.90]	6.37 [6.06, 7.76]	15.37 [14.48, 16.08]
5	63.90 [63.40, 64.13]	65.10 [64.18, 65.51]	7.57 [7.25, 11.08]	6.95 [6.00, 7.25]	12.16 [10.33, 12.33]
6	76.80 [76.28, 76.85]	77.67 [76.71, 77.76]	8.90 [7.98, 11.76]	8.32 [7.45, 10.98]	14.99 [13.85, 17.45]
7	68.02 [67.79, 68.40]	69.51 [69.09, 70.23]	13.64 [12.65, 19.46]	17.82 [16.54, 29.65]	34.25 [32.10, 35.36]
8	73.20 [72.98, 73.62]	74.71 [74.31, 75.49]	7.24 [6.96, 10.50]	6.01 [5.87, 6.99]	11.39 [10.97, 15.39]
9	68.70 [68.31, 68.98]	70.08 [69.36, 70.60]	8.07 [7.62, 11.39]	7.03 [7.00, 9.41]	11.99 [11.95, 14.59]
10	70.20 [69.89, 70.53]	71.62 [71.05, 72.22]	16.84 [15.46, 23.36]	16.84 [15.47, 23.36]	24.44 [22.90, 29.51]

^a: Values shown at this position for patients 1-10 indicate the SIB dose and TCP increase derived from Equation 4.1.

^b: Ranges shown at this position for patients 1-10 indicate the SIB dose and TCP increase derived from the confidential bound in Figure 4.1.

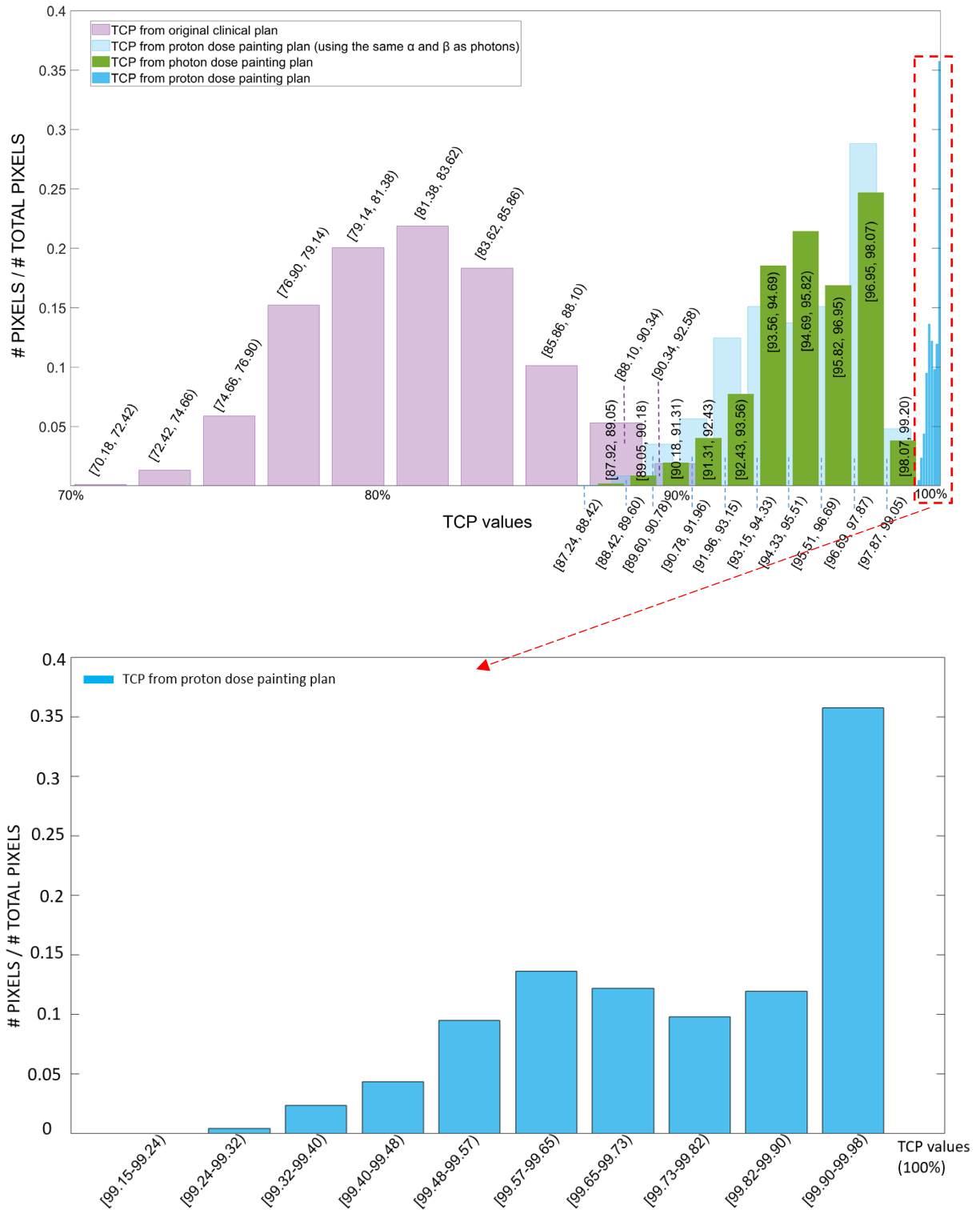
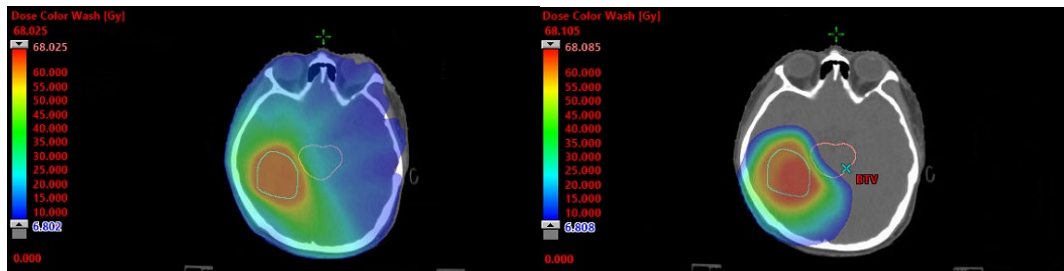


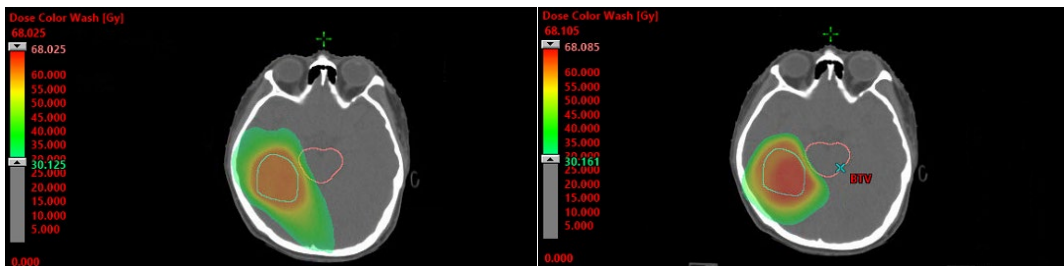
Figure 5.3 TCP distributions with different optimisation strategies in photon and proton radiotherapy.

5.3.2 Doses to Target and OARs

Dose color wash images of a patient illustrated the typical qualitative difference in dose distribution between photon and proton dose-painting plans, as are shown in Figure 5.4. Large normal tissue volumes in the proton plans could be spared from the low dose bath.



(a) Dose > 0Gy



(b) Dose > 30Gy



(c) Dose > 60Gy

Figure 5.4 Dose distributions of photon dose painting plan (left column) and proton dose painting plan (right column) for an example patient case.

The target coverage and constraints for OARs were reachable in proton dose painting plans. For the dose to target, several dose/volume metrics (*e.g.*, $D_{98\%}$, $D_{95\%}$, mean and $D_{2\%}$) were used to evaluate the treatment plans, where the target coverage was reported with regards to the percentage of the prescription dose to a certain volume. Taking $D_{98\%}$ as an example, it means dose levels exposed on 98% of BTV volume should be over 90% of the prescription dose. Other metrics' requirements have been elaborated in Table 5.2. It is demonstrated that all the doses' levels to targets are satisfied. As was shown in Table 5.1, SIB doses for proton dose painting using different α and β are reported separately. As for CTV, since both proton and photon dose painting plans were performed with the same standard prescription dose (60Gy), dose levels to CTV in both techniques were compared, with almost the same dose coverage.

For the doses to OARs, the maximum dose to all OARs were reported in Table 5.2. In addition, another dose metric $D_{0.1cc}$ representing the dose level corresponding to 0.1 cm³ of the brainstem was also evaluated. Table 5.2 demonstrated a significant drop in terms of radiation doses to all OARs in the proton dose painting plan among 10 patients, particularly for OARs related to visual pathway, almost zero doses exposed. Moreover, the mean dose levels in non-tumor tissues have been evaluated, leading to around 2 times dose reduction versus photon dose painting plans.

Table 5.2 Results of dose coverage in original plan and does painting plans (the range shown the table represents the median, lowest and highest values among 10 patients).

Structure	Dose/volume metric	Required dose	Original clinical plan	Photon Dose painting plan	Proton dose painting plan
			Median [range]		
BTV_photon	D _{98%}	>90%	\	97.98% [95.13%, 99.82%]	\
	D _{95%}	>95%	\	98.52% [96.60%, 100.29%]	\
	mean	=100%	\	100.00% [99.52%, 101.41%]	\
	D _{2%}	<110%	\	101.37% [100.26%, 102.60%]	\
BTV_proton	D _{98%}	>90%	\	\	97.87% [95.80%, 99.34%]
	D _{95%}	>95%	\	\	98.34% [97.20%, 99.55%]
	mean	=100%	\	\	100.00% [99.12%, 100.34%]
	D _{2%}	<110%	\	\	101.35% [100.17%, 102.70%]

CTV	D _{98%}	>90%	101.05% [99.46%, 104.45%]	99.68% [97.41%, 102.58%]	98.77% [91.50%, 99.79%]
	D _{95%}	>95%	101.45% [100.00%, 104.76%]	100.66% [98.08%, 103.44%]	99.20% [97.02%, 100.54%]
PTV	D _{98%}	>90%	97.65% [95.90%, 100.80%]	98.26% [92.10%, 99.22%]	\
	D _{95%}	>95%	100.05% [98.59%, 101.09%]	99.20% [97.75%, 101.09%]	\
Brainstem (Gy)	max	60Gy	53.94 [3.48, 58.68]	52.40 [4.44, 56.17]	37.08 [3.89, 49.20]
	D0.1cc	55Gy	53.65 [3.48, 57.00]	50.98 [4.52, 54.82]	26.24 [2.78, 43.89]
Optic nerve left (Gy)	max	50Gy	11.95 [1.30, 46.93]	13.45 [1.83, 34.31]	0.03 [0.00, 20.50]
Optic nerve Right (Gy)	max	50Gy	16.63 [1.28, 52.85]	15.48 [1.43, 48.46]	0.23 [0.00, 29.85]
Optic chiasm (Gy)	max	55Gy	29.82 [1.91, 54.37]	27.64 [2.67, 54.82]	2.39 [0.05, 49.62]
Eye left (Gy)	max	45Gy	13.57 [1.21, 54.48]	13.92 [1.78, 44.42]	0.00 [0.00, 38.64]
Eye right (Gy)	max	45Gy	15.87 [1.11, 60.91]	18.64 [1.30, 44.03]	0.00 [0.00,38.51]
Lens left (Gy)	max	10Gy	6.55 [0.69, 8.33]	4.04 [0.85, 8.31]	0.00 [0.00, 3.09]
Lens right (Gy)	max	10Gy	6.81	6.40	0.00

			[0.73, 8.21]	[0.75, 9.65]	[0.00, 4.67]
Non-tumor tissue			6.81	7.23	3.92
(body minus	mean	reported			
PTV) (Gy)			[3.24, 12.65]	[4.55, 16.64]	[2.35, 7.72]

5.3.3 Robustness Evaluation

In this section, robust evaluation for proton dose painting plans has been investigated, which is a necessary approach to evaluate proton plans since the technique of proton treatment is susceptible to range and set-up uncertainties. Table 5.3 represents the dose levels in nominal plans and the dose range arising from 12 robust evaluation scenarios, where the lowest and highest values are defined as D_{robust}^{min} and D_{robust}^{max} , respectively. Dose values to BTV_proton and CTV have been collected. The results demonstrated that doses to targets have been satisfied by the requirement of dose/volume metrics (*e.g.*, D_{98%}, D_{95%}, mean and D_{2%}) in 12 uncertainty scenarios. Table 5.4 represents the results of robust evaluation for selected OARs, including brainstem, optic chiasma, optic nerves, eye globes and lenses. All nominal treatment plans and 12 uncertainty scenario plans demonstrated that in OAR doses were within the prescribed tolerance limits. These make sense since the proposed proton dose painting plan followed the principle of robust optimization by adopting range and positional uncertainties, as discussed in Section 5.3.3.

Table 5.3 Dose coverage for BTV and CTV from the complete proton dose painting plans of all patients.

Dose levels in nominal plans and [D_{robust}^{min} , D_{robust}^{max}] (Gy)						
Patient	BTV_Proton				CTV	
	D _{98%}	D _{95%}	mean	D _{2%}	D _{98%}	D _{95%}
1	67.24	67.45	67.95	68.67	59.60	61.02
	[66.63, 67.14]	[66.94, 67.96]	[67.79, 68.05]	[68.57, 69.08]	[59.31, 59.72]	[60.82, 61.12]
2	63.68	63.78	64.23	64.58	59.64	60.35
	[63.27, 63.57]	[63.37, 63.68]	[63.93, 64.24]	[64.38, 64.68]	[59.24, 59.64]	[60.14, 60.35]
3	66.88	66.98	67.44	67.90	59.45	60.75
	[65.96, 66.88]	[66.27, 67.08]	[67.13, 67.60]	[67.70, 68.21]	[59.25, 59.45]	[60.55, 60.75]
4	67.73	67.83	68.49	69.25	58.87	60.70
	[66.91, 67.52]	[67.32, 67.73]	[68.24, 68.45]	[68.95, 69.25]	[55.40, 60.19]	[60.19, 60.80]
5	64.49	64.61	65.11	66.32	59.79	60.21
	[62.25, 64.59]	[63.78, 64.69]	[64.84, 65.23]	[65.41, 66.32]	[57.28, 63.79]	[58.09, 66.13]
6	74.84	75.65	77.13	79.29	58.96	59.36
	[69.68, 74.23]	[72.51, 75.24]	[76.42, 76.99]	[78.48, 79.79]	[52.49, 59.06]	[58.25, 59.57]
7	68.88	68.98	69.65	70.31	59.20	59.40
	[68.16, 68.57]	[68.57, 68.88]	[68.68, 69.61]	[70.10, 71.94]	[58.00, 59.30]	[59.20, 59.50]
8	73.66	73.97	74.73	75.50	60.19	60.50
	[71.52, 73.05]	[72.33, 73.46]	[74.25, 74.64]	[75.39, 75.70]	[59.48, 60.30]	[50.40, 60.70]

9	68.86	59.06	70.13	71.00	58.35	60.29
	[67.12, 68.65]	[67.94, 69.16]	[69.68, 70.31]	[70.69, 71.20]	[55.39, 59.88]	[58.55, 60.59]
10	70.80	70.94	71.63	72.84	62.20	62.75
	[70.09, 70.80]	[70.40, 71.01]	[71.28, 71.79]	[72.23, 73.25]	[59.80, 61.80]	[60.50, 62.50]

Table 5.4 Dose levels to OARs from the complete proton dose painting plans of all patients.

Dose levels in nominal plans and [D_{robust}^{min} , D_{robust}^{max}] (Gy)										
Patient	Brain stem	Optic nerve left	Optic nerve right	Optic chiasm	Eye left	Eye right	Lens left	Lens right	Non- tumor tissue (body minus PTV)	
										D_{max}
1	48.00	38.90	0.00	0.00	0.00	0.00	0.00	0.00	0.00	6.47
	[34.70, 59.35]	[26.60, 53.30]	[0.00, 0.00]	[0.00, 0.00]	[0.00, 0.00]	[0.00, 0.00]	[0.00, 0.00]	[0.00, 0.00]	[0.00, 0.00]	[6.01, 7.01]
2	6.40	4.40	0.00	0.00	1.80	0.30	0.00	0.00	0.00	2.38
	[1.60, 17.64]	[1.00, 13.60]	[0.00, 0.40]	[0.00, 0.00]	[0.30, 6.10]	[0.00, 0.80]	[0.00, 0.00]	[0.00, 0.00]	[0.00, 0.00]	[2.26, 2.51]
3	9.00	7.10	0.00	0.40	0.20	0.00	0.00	0.00	0.00	3.58
	[3.40, 22.30]	[1.40, 18.30]	[0.00, 0.00]	[0.00, 2.50]	[0.00, 1.50]	[0.00, 0.00]	[0.00, 0.00]	[0.00, 0.00]	[0.00, 0.00]	[0.53, 3.86]
4	48.40	46.10	0.80	47.92	47.80	0.00	6.30	0.00	0.20	4.90
	[44.90, 52.30]	[43.50, 50.30]	[0.20, 2.50]	[43.40, 52.00]	[41.00, 52.70]	[0.00, 0.00]	[2.90, 22.50]	[0.00, 0.00]	[0.10, 0.50]	[4.52, 5.28]
5	53.40	52.13	15.67	7.99	47.00	0.11	0.34	0.00	0.00	3.92
	[52.60, 55.20]	[52.29, 57.41]	[7.50, 27.30]	[3.60, 14.60]	[43.80, 52.00]	[0.00, 0.40]	[0.10, 0.70]	[0.00, 0.00]	[0.00, 0.00]	[3.67, 4.14]

	51.70	46.70	14.20	16.20	26.40	22.30	39.40	3.00	3.30	2.40
6	[39.82, 58.00]	[32.87, 56.00]	[6.90, 28.20]	[7.30, 30.00]	[17.90, 49.00]	[14.50, 33.10]	[29.00, 49.50]	[1.20, 6.70]	[2.10, 5.90]	[2.19, 2.65]
	50.70	44.15	5.30	0.00	22.10	0.00	0.00	0.00	0.00	7.25
7	[42.90, 55.90]	[34.80, 52.30]	[2.70, 9.90]	[0.00, 0.00]	[13.00, 35.70]	[0.00, 0.10]	[0.00, 0.00]	[0.00, 0.00]	[0.00, 0.00]	[6.54, 8.01]
	13.30	10.70	0.00	0.10	6.20	0.00	0.80	0.00	0.00	1.94
8	[5.63, 26.10]	[4.33, 21.98]	[0.00, 0.50]	[0.00, 0.70]	[2.10, 14.90]	[0.00, 0.00]	[0.11, 2.43]	[0.00, 0.00]	[0.00, 0.00]	[0.29, 2.09]
	51.70	49.12	0.10	49.11,	50.90	0.00	8.33	0.00	0.30	4.28
9	[8.10, 56.42]	[7.00, 53.39]	[0.00, 0.30]	11.70, 50.60]	[6.70, 51.52]	[0.00, 0.10]	[3.90, 17.23]	[0.00, 0.00]	[0.00, 1.40]	[0.59, 4.59]
	2.92	2.16	0.00	0.30	0.04	0.00	0.00	0.00	0.00	3.50
10	[1.00, 10.00]	[0.60, 8.00]	[0.00, 0.00]	[0.00, 0.00]	[0.00, 0.50]	[0.00, 0.00]	[0.00, 0.00]	[0.00, 0.00]	[0.00, 0.00]	[3.29, 3.91]

Treatment planning and delivery in proton and photon RT are susceptible to inevitable uncertainties, set-up and range uncertainties in proton plans while only set-up uncertainties in photon plans. I now investigate the robustness comparison between proton and photon dose painting plans by using the width of the DVHs variation, R , as has been introduced in Equation 5.1.

In Table 5.5, for doses to targets, the R values related to CTV were smaller in the proton dose painting plans in terms of $D_{98\%}$ with the statistical difference ($P < 0.05$), resulting in higher robustness compared to photon dose painting plans. As for $D_{95\%}$, there is no statistical difference between proton and photon plans.

For doses to OARs, since the extremely low dose levels were delivered to OARs related to visual pathway, their R values were smaller in the proton plans with the significant statistical difference ($P < 0.001$). Therefore, proton dose painting plans are more robust than photon dose painting plans for OARs on the visual pathways. However, the R values for brainstem is larger than in proton dose painting plan with $P < 0.001$. This is because if

an OAR is close to the tumor target, a significant dose variation will be observed in such OAR due to the range uncertainty in proton therapy, and for the patients' cohort enrolled in this chapter, most patients' tumors are close to brain stem.

Table 5.5 The comparison of robust evaluation between the photon dose painting plans and the proton dose painting plans (lower R values with statistical difference are displayed as bold; and the range shown the table represents the median, lowest and highest values among 10 patients).

Structure	Dose/volume metric	Photon robustness	Proton robustness	p-value
		Median [range]		
BTV_photon	D _{98%}	4.33 [4.06, 5.24]	\	\
	D _{95%}	3.01 [2.46, 4.42]	\	\
	mean	1.72 [1.39, 2.52]	\	\
	D _{2%}	1.18 [0.96, 1.74]	\	\
BTV_proton	D _{98%}	\	1.22 [0.30, 4.55]	\
	D _{95%}	\	0.97 [0.30, 2.73]	\
	mean	\	0.43 [0.21, 0.63]	\
	D _{2%}	\	0.51 [0.30, 1.31]	\
CTV	D _{98%}	4.53 [3.31, 7.51]	3.24 [0.20, 6.57]	0.015
	D _{95%}	1.08 [0.88, 1.59]	1.31 [0.20, 10.30]	0.58
PTV	D _{98%}	7.59 [7.11, 9.18]		\
	D _{95%}	2.57 [2.09, 3.78]		\
Brainstem	max	1.09 [0.89, 1.61]	14.50 [5.30, 24.60]	<0.001
	D0.1cc	2.07 [1.31, 2.37]	14.75 [4.80, 26.70]	<0.001

Optic nerve left	max	16.45 [15.03,18.74]	0.45 [0.00, 21.30]	<0.001
Optic nerve right	max	18.99 [17.21,21.64]	1.60 [0.00, 22.70]	<0.001
Optic chiasm	max	30.40 [26.62,37.48]	9.75 [0.00, 31.10]	<0.001
Eye left	max	12.51 [11.43,14.25]	0.05 [0.00, 18.60]	<0.001
Eye right	max	10.85 [9.34, 12.36]	0.30 [0.00, 20.50]	<0.001
Lens left	max	7.62 [7.15, 9.22]	0.00 [0.00, 5.50]	<0.001
Lens right	max	7.18 [6.74, 8.69]	0.00 [0.00, 3.80]	<0.001
Non-tumor tissue (body minus PTV)	mean	0.15 [0.10, 0.20]	0.56 [0.25, 1.47]	<0.001

5.4 Discussion

GBMs are difficult to manage because of the complex anatomy and sometimes they are close to sensitive OARs. A proper RT treatment is necessitated, where higher dose levels can be delivered to tumor area while low dose levels to OARs. Proton therapy has the potential to address this issue for GBM due to its Bragg peak characteristic. Several studies have conducted clinical trials and reported that proton beam therapy could control GBM pathogenesis if the treatment area completely covers tumor infiltration [252]. However, to the best of our knowledge, there is no quantitative imaging-based proton dose painting plan for GBM. In this chapter, the dose painting technique described in the previous chapter was combined with the proton therapy to further optimise the dose distribution for proton. I presented the first dose painting method for GBM in proton

therapy which combines DW-MRI and voxel-level TCP maps for the improvement of tumor control and OARs protection. 10 newly diagnosed GBM patients were enrolled in this chapter to illustrate proton dose painting. The results showed that proton dose artworks were superior to photon treatment in terms of the constraints placed on the OARs' dosage and the TCP increase. Extensive discussions have been provided for the robustness evaluation of both photon and proton dose painting plans.

Compared with the photon dose painting plans, ProtonDP_{bio} have higher tumor control probability. This is because SIB doses to BTV_{proton} are slightly higher than those used in photon plans, and radiobiological characteristics of proton beam leads to high TCP in proton therapy, which are characterised by α and β in proton TCP models. On the other hand, TCP increases in the ProtonDP_{cli} are slightly inferior than photon dose painting plans although the SIB doses are the same. This is because less doses are delivered outside of the BTVs in ProtonDP_{cli} than those in photon dose painting plans due to proton's Bragg Peak. Lower doses to OARs, especially in visual pathway, were demonstrated in proton dose painting plans. Moreover, the doses to non-tumor tissue (body-minus-PTV) were reduced by about 40% in the ProtonDP_{bio} compared with photon dose-painting plans. Therefore, the normal tissue complication probability and toxicities related to radiation therapy of GBM, *e.g.*, nausea and vomiting due to brain radiation damage, can be reduced. There is, however, for small number of patients, no significant difference between photon and proton dose painting plans in terms of the delivered doses in OARs close to the target, such as the brain stem, due to the tradeoff necessary to obtain robust coverage of target structures. Securing fair comparison of photon and proton dose plans, in terms of target coverage in the presence of clinically relevant uncertainties, is a general issue in dose plan comparisons. The target coverage doses ($D_{98\%}$ to BTV_{proton} and BTV_{photon})

were higher in the photon plans. However, it is important to note that all proton plans had the required dose coverage of BTV and CTV (60Gy) in all uncertainty scenarios considered (Table 5.2).

Gondi *et al.* conducted a clinical trial for proton dose painting (NRG BN001) for GBM [240] and escalated the dose of 75Gy to the GTV area. The results of this trial have not been released yet, however, some hypotheses suggested that the increased conformality may result in fewer toxicities, particularly related to lymphopenia which is associated with overall survival in GBM [240]. Mirroring current photon clinical trials that have employed over 70Gy and even 80Gy for GBM RT, as summarized in Table 2.6 and Table 2.7 in Section 2.2. The optimized proton and photon dose levels presented herein work accordingly with the reported GBM clinical trials.

In the current practice of photon RT, only set-up error uncertainties are considered and dealt by providing margins around the CTV and critical organs, thus creating PTV and PRV, as recommended by the International Commission on Radiation Units and Measurements (ICRU) report 83 [17]. However, treatment planning and delivery in proton RT are susceptible to both range and set-up uncertainties. To mitigate such uncertainties, CTV-based robust optimization incorporating both set-up and range uncertainties, has been widely adopted in the procedure of plan optimisation. Compared to PTV-based optimisation, robust optimisation not only improves the robustness of the treatment plan, but also reduces the dose to normal tissues [245], [253]. There are several reasons for this phenomenon: (1) the robust optimisation integrated range uncertainties specific to protons to better exploit the clinical potential for proton therapy; (2) the conventional optimised prescription dose covers the PTV, whereas the robust optimised

prescription dose covers the CTV in the presence of deviations, and the volume of the PTV is larger than the CTV, therefore, robust optimisation provides better protection to normal tissues. Consequently, robustness evaluation is considered as an integral component of decision making in proton treatment plan. In this chapter, the robust optimisation and evaluation integrated range and position uncertainties specific to protons have been presented to better exploit the clinical potential for proton therapy. The results demonstrated that doses to targets and OARs are all satisfied by dose/volume requirements, providing a complete approach to find the right balance between target coverage and OAR sparing.

The robustness evaluation has been compared between proton and photon dose painting plans by using the width of the DVHs variation, R . The robustness of proton dose painting plans in terms of CTV $D_{98\%}$ and OARs related to visual pathway are better than photon dose painting plans, with statistical differences. However, the brainstem's robustness of proton plans is lower than photon plans. It is because, for OARs sparing, the compromise is required between doses to OARs close to the target and the robustness of target dose.

The combination of the observed uncertainty and the sensitivity of proton max doses to anatomical changes, urge for great care if pursuing proton dose-painting for GBM. Daily imaging, preferably in 3D, would be warranted, as well as adaptive robust optimization during the course of treatment.

5.5 Conclusion

In conclusion, this chapter showed that proton dose-painting plans can be optimized with a quality comparable to photon dose-painting plans, but with different merits. The results are in line with expectations considering the physical properties of the proton beams. Applying SIB doses to BTV defined by quantitative imaging and proton TCP model, up to 34.25% increase in TCPs have been observed, compared with the original clinical delivered photon plans. Doses to OARs and non-tumor tissues have been decreased, almost 0Gy to OARs related to visual pathway. The robustness was generally higher in the proton plans in terms of target dose and most OARs.

Chapter 6

Conclusion and Future Work

6.1 Summary of Contributions

Brain tumor treatments requiring novel dose assigning techniques especially those featuring personalised optimisations that can be applied to an individual patient, have been increasingly popular. Personalised prescribed doses used for treatment planning can be varied owing to the radiobiological characteristics and radiotherapy technologies (*e.g.*, photon or proton). To solve this problem, in Chapter 2, I summarize the current research status and consequently propose three techniques for prescription dose optimization in Chapters 3-5. In this thesis, I first ask:

- Can a personalised prescription dose be calculated by investigating the biological models, *i.e.*, TCP and NTCP models, achieving higher therapeutic ratios while protecting the normal organs at risk within the radiation thresholds?

In Chapter 3, I have proposed an optimization of prescription dose based on a radiobiological model, paving the way for personalized optimization and treatment. Since TCP and NTCP models can transfer the physical dose to biological effect, they are employed to construct a dose-optimization model. Among 17 patients, the results show that the prescription doses to 11 patients have been increased to improve the therapeutical

ratio, and the radiation doses to OARs are all increased but still within their tolerance. The prescription doses to the remaining 6 patients are decreased for the improvement of therapeutic ratios. For these patients, some OARs exceed the tolerance under the original prescription dose, while OARs' tolerances are satisfied, and all the normal tissues can be better spared when the optimized prescription dose is applied. By use of the optimized dose, a higher therapeutic ratio is achieved, and OARs are protected, which is especially meaningful for larger tumors and tumors close to OARs. This proposed method can be used as a design scheme for clinical trials.

I have studied different types of brain tumors. The results reveal that to increase the therapeutic ratio, there will be a reduced prescription dose versus the original one, when a tumor is extremely near to OAR. However, since highly aggressive tumors such as GBM are resistant to insufficient radiation doses, their tumor control will be poor. Therefore, a more practical way is to define risk of progression within the tumor by considering the tumor's heterogeneity. Only boosting doses to the high-risk area can avoid dose increasing to the surrounding OARs. Since GBM accounts for the largest proportion (46.6%) of all types of brain tumors [254], I study the optimization of prescription doses for GBM patients. The proposed dose prescription prediction method features a heterogeneous irradiation analysis by using quantitative medical imaging and the TCP model. Even though the whole-tumor-based TCP values has been calculated for dose optimization, the radiobiological variabilities amongst and within patients can affect the treatment outcome of radiotherapy. Medical imaging can bring patient-specific information into the models, as presented in Section 2.2, describing intra-patient heterogeneity at the voxel scale. I therefore asked:

- Can medical imaging-based biomarker be introduced to enable a personalized radiobiological model to calculate the voxel-level TCP that corresponds to the planned dose distribution for each patient treatment?

In Chapter 4, I have proposed a personalised dose painting method to escalate the dose focally at specific intratumoural areas, which indicate a higher disease burden according to the quantitative medical imaging, in order to increase TCP values. For the enrolled 10 GBM patients, ADC-driven dose painting is used to increase the dose to a specific location in the GTV. TCP increases can be obtained without violating OAR tolerances. In the proposed method, patients with a higher number of tumor cells, *i.e.*, lower TCP values, have a higher possibility for TCP rise. Furthermore, ADC has been shown to be an imaging cellularity biomarker that can be used to select patients and guide dose escalation in a personalised manner. The proposed method is able to achieve an up to 16.84% increase in TCP for the patient cohort by increasing the prescription doses to tailored levels using a SIB to each patient's BTV without exceeding the dose tolerance of the OARs. This is feasible due to the fact that higher doses increase the death of tumor cells [214], [215]. The proposed technique boosts the prescription doses by 6.50% to 28.00% in the portion of the tumor that has a higher cell density in the patient group.

Studies presented in Chapter 4 have demonstrated that for personalised photon irradiation a greater dose is delivered to certain parts of the tumor, resulting in an increase in TCP, and that the dose of OARs does not exceed their dose limits. Proton radiotherapy treatment can deliver a far lower dose to healthy tissues around the tumor than photon radiotherapy because of its characteristic "Bragg" peak. The risk of radiation damage to healthy tissues in the surrounding area is lowered. As a result, we can attain a higher

therapeutic ratio by using proton radiotherapy. This observation leads to the third research question I aim to address:

- How is it possible to perform personalised proton dose painting by using proton radiotherapy properties in the treatment of brain tumor patients?

In Chapter 5, proton dose-painting plans have been optimised, along with quality comparison with photon dose-painting plans, by using distinct features in proton radiotherapy. Given the physical properties of proton and photon beams, the experimental results are in accordance with expectations. Proton plans are generally more robust in terms of target dosage, resulting in lower doses to most OARs and non-tumor tissue than photon plans. The expected advantages of proton therapy compared to photon therapy are higher tumor control probability and lower the complication probability of OARs in terms of brainstem and visual pathway. The doses are boosted up to 21.6% to the high-risk area. Up to 34.25% increase in TCP values have been demonstrated compared with the original clinically delivered photon plans. In most cases of my patient's cohort, the doses to visual pathway are almost 0Gy. The known toxicities related to radiation therapy of GBM, *e.g.*, nausea and vomiting due to brain radiation damage, are reduced.

6.2 Future Work

I have identified several promising directions for future work based on my research conducted in this thesis.

- 1) Adaptive dose painting techniques incorporated with machine learning

To precisely deliver the RT treatment, patients' anatomy and biology knowledge during treatment is necessitated, as uncalculated deviations may affect the treatment success. Adaptive radiotherapy is a framework that modifies variations during the treatment course [255]. At RT planning stage, DW-MRI can be used to assess the tumor areas that are easy or hard to control. Apart from DW-MRI, there are other quantitative imaging techniques to measure tumor or tissue functions. For GBM, some studies have employed magnetic resonance spectrum imaging (MRSI) to define the high-risk areas by measuring chemical composition and metabolic activity of tissues [86-91]. Moreover, perfusion imaging can provide information about tissue viability, vascularization and responses to treatment by measuring blood flow within tissues [256]. Through perfusion imaging, we can gain insights into the oxygenation levels and nutrient supply to tumors. This information can facilitate identifying hypoxic regions within tumors, which are often associated with resistance to RT. Personalized radiotherapy plans can then be tailored to target these hypoxic regions, either by modifying the treatment regimen or by integrating techniques (*e.g.*, hypoxia-specific radiosensitizers). If the patients perform the same MRI modality scanning after 1-2 weeks of radiotherapy, the change of corresponding biomarkers after several fractions of radiotherapy could be used to define radio sensitivity and radio resistance. With the help of machine learning, the automatic contouring of high-risk area can be implemented on the new series of MRI modalities, and fast automatic treatment planning can be realized for the adaptive RT.

2) Linear energy transfer (LET)-painting proton therapy based on functional imaging

LET values indicate the ability of eliminating cells, higher LET values lead to more irreparable damage [257]. Compared with photon beams, proton beams have high LET

values. Therefore, how to guarantee the high LET proton beams onto the tumor volume is a hot research topic in proton therapy. Current intensity-modulated proton therapy (IMPT) plan may cause high LET in normal tissues instead of target volumes due to the range uncertainty and position uncertainty of proton beams. To address this issue, researchers from the MD Anderson Cancer Center have studied the impact of incorporating LET management directly into treatment planning [104]. Their results showed that LET has been increased in target volumes and reduced in critical structures compared with a conventional IMPT plan [104]. As has been mentioned in the previous chapters of this thesis, using functional imaging can define the tumor area with high risk of progression. Delivering the higher LET to such high-risk area would be feasible to increase the treatment outcome and protect normal tissues.

3) Dose painting by numbers (DPBN) technique incorporated in standard TPS

Dose painting by numbers, also known as DPBN, is a technique that may give a heterogeneous dose to a tumor voxel-by-voxel using a prescription dose derived from biological medical imaging. However, current commercial treatment planning systems (TPS) do not facilitate the planning of DPBN. In the future, it is worth exploring the possibility of developing a planning system for clinical implementation of DPBN. In particular, how to assign doses to the voxel level needs to be investigated. In this way, an effective strategy for dose escalation based on biological optimizations can be presented for further TCP improvement.

6.3 Final Remarks

Through the work presented in this thesis, I have achieved significant advancement in the combination of radiobiological mathematical models, quantitative imaging, photon and proton radiotherapy dose painting techniques to enable personalised brain tumor treatment planning. Several novel techniques for analysing the radiobiological uncertainties and treatment planning optimisations are introduced and evaluated on brain tumor patients. I have demonstrated a personalised radiotherapy plan, following a dose painting method to escalate the dose focally at specific intratumoural areas, which [shows](#) a higher disease burden, in order to increase the TCP. Proton radiotherapy properties have also been investigated and employed for a personalised proton tumor treatment planning along with robustness evaluation. The contributions of this thesis have the potential to open up new research avenues in brain tumor radiotherapy, such as more adaptive dose painting techniques, combined with machine learning and dose painting by numbers.

References

- [1] H. Paganetti, *Proton Therapy Physics, Second Edition*. CRC Press, 2018.
- [2] W. D. Newhauser and R. Zhang, ‘The physics of proton therapy’, *Phys. Med. Biol.*, vol. 60, no. 8, pp. R155–R209, 2015, doi: 10.1088/0031-9155/60/8/R155.
- [3] F. Bray, J. Ferlay, I. Soerjomataram, R. L. Siegel, L. A. Torre, and A. Jemal, ‘Global cancer statistics 2018: GLOBOCAN estimates of incidence and mortality worldwide for 36 cancers in 185 countries’, *CA. Cancer J. Clin.*, vol. 68, no. 6, pp. 394–424, Nov. 2018, doi: 10.3322/caac.21492.
- [4] D. Capper *et al.*, ‘DNA methylation-based classification of central nervous system tumours’, *Nature*, 2018, doi: 10.1038/nature26000.
- [5] R. Mohan and D. Grosshans, ‘Proton therapy - Present and future’, *Adv. Drug Deliv. Rev.*, vol. 109, pp. 26–44, Jan. 2017, doi: 10.1016/j.addr.2016.11.006.
- [6] M. S. Linet, L. A. G. Ries, M. A. Smith, R. E. Tarone, and S. S. Devesa, ‘Cancer Surveillance Series: Recent Trends in Childhood Cancer Incidence and Mortality in the United States’, *JNCI J. Natl. Cancer Inst.*, vol. 91, no. 12, pp. 1051–1058, Jun. 1999, doi: 10.1093/jnci/91.12.1051.
- [7] R. Singh *et al.*, ‘Dose Escalated Radiation Therapy for Glioblastoma Multiforme: An International Systematic Review and Meta-Analysis of 22 Prospective Trials’, *Int. J. Radiat. Oncol. Biol. Phys.*, vol. 111, no. 2, pp. 371–384, 2021, doi: 10.1016/j.ijrobp.2021.05.001.
- [8] A. Gajjar *et al.*, ‘Risk-adapted craniospinal radiotherapy followed by high-dose chemotherapy and stem-cell rescue in children with newly diagnosed medulloblastoma (St Jude Medulloblastoma-96): long-term results from a prospective, multicentre trial’, *Lancet Oncol.*, vol. 7, no. 10, pp. 813–820, Oct. 2006, doi: 10.1016/S1470-2045(06)70867-1.
- [9] P. M. Zeltzer *et al.*, ‘Metastasis Stage, Adjuvant Treatment, and Residual Tumor Are Prognostic Factors for Medulloblastoma in Children: Conclusions From the Children’s Cancer Group 921 Randomized Phase III Study’, *J. Clin. Oncol.*, Sep. 2016, doi: 10.1200/JCO.1999.17.3.832.
- [10] T. E. Merchant, C. Li, X. Xiong, L. E. Kun, F. A. Boop, and R. A. Sanford, ‘Conformal radiotherapy after surgery for paediatric ependymoma: a prospective study’, *Lancet Oncol.*, vol. 10, no. 3, pp. 258–266, Mar. 2009, doi: 10.1016/s1470-2045(08)70342-5.
- [11] S. N. Chi *et al.*, ‘Intensive Multimodality Treatment for Children With Newly Diagnosed CNS Atypical Teratoid Rhabdoid Tumor’, *J. Clin. Oncol.*, vol. 27, no. 3, pp. 385–389, Jan. 2009, doi: 10.1200/JCO.2008.18.7724.
- [12] B. W. Fischer-Valuck *et al.*, ‘Assessment of the treatment approach and survival outcomes in a modern cohort of patients with atypical teratoid rhabdoid tumors using the National Cancer Database’, *Cancer*, vol. 123, no. 4, pp. 682–687, Feb. 2017, doi: 10.1002/cncr.30405.
- [13] Q. T. Ostrom, G. Cioffi, K. Waite, C. Kruchko, and J. S. Barnholtz-Sloan, ‘CBTRUS Statistical Report: Primary Brain and Other Central Nervous System Tumors Diagnosed in the United States in 2014–2018’, *Neuro-Oncol.*, vol. 23, no. Supplement_3, pp. iii1–iii105, Oct. 2021, doi: 10.1093/neuonc/noab200.

- [14] A. Korshunov, A. Golanov, R. Sycheva, and V. Timirgaz, ‘The histologic grade is a main prognostic factor for patients with intracranial ependymomas treated in the microneurosurgical era: an analysis of 258 patients’, *Cancer*, vol. 100, no. 6, pp. 1230–1237, Mar. 2004, doi: 10.1002/cncr.20075.
- [15] R. G. Grundy *et al.*, ‘Primary postoperative chemotherapy without radiotherapy for treatment of brain tumours other than ependymoma in children under 3 years: results of the first UKCCSG/SIOP CNS 9204 trial’, *Eur. J. Cancer Oxf. Engl. 1990*, vol. 46, no. 1, pp. 120–133, Jan. 2010, doi: 10.1016/j.ejca.2009.09.013.
- [16] T. Kron, ‘Special Delivery Techniques: Dedicated to Michael Sharpe’, in *Clinical 3D Dosimetry in Modern Radiation Therapy*, CRC Press, 2017.
- [17] ‘ICRU Report 83, Prescribing, Recording, and Reporting Intensity-Modulated Photon-Beam Therapy (IMRT) – ICRU’. <https://www.icru.org/report/prescribing-recording-and-reporting-intensity-modulated-photon-beam-therapy-imrticru-report-83/> (accessed Aug. 26, 2022).
- [18] E. Shaw *et al.*, ‘Single dose radiosurgical treatment of recurrent previously irradiated primary brain tumors and brain metastases: final report of RTOG protocol 90-05’, *Int. J. Radiat. Oncol. Biol. Phys.*, vol. 47, no. 2, pp. 291–298, May 2000, doi: 10.1016/s0360-3016(99)00507-6.
- [19] *Perez and Brady’s principles and practice of radiation oncology*, 6th ed. Philadelphia: Wolters Kluwer health - Lippincott Williams & Wilkins, 2013.
- [20] W. Roa *et al.*, ‘Abbreviated course of radiation therapy in older patients with glioblastoma multiforme: a prospective randomized clinical trial’, *J. Clin. Oncol. Off. J. Am. Soc. Clin. Oncol.*, vol. 22, no. 9, pp. 1583–1588, May 2004, doi: 10.1200/JCO.2004.06.082.
- [21] A. Malmström *et al.*, ‘Temozolomide versus standard 6-week radiotherapy versus hypofractionated radiotherapy in patients older than 60 years with glioblastoma: the Nordic randomised, phase 3 trial’, *Lancet Oncol.*, vol. 13, no. 9, pp. 916–926, Sep. 2012, doi: 10.1016/S1470-2045(12)70265-6.
- [22] F. Pignatti *et al.*, ‘Prognostic Factors for Survival in Adult Patients With Cerebral Low-Grade Glioma’, *J. Clin. Oncol.*, vol. 20, no. 8, pp. 2076–2084, Apr. 2002, doi: 10.1200/JCO.2002.08.121.
- [23] A. B. M. F. Karim *et al.*, ‘A randomized trial on dose-response in radiation therapy of low-grade cerebral glioma: European Organization for Research and Treatment of Cancer (EORTC) study 22844’, *Int. J. Radiat. Oncol.*, vol. 36, no. 3, pp. 549–556, Oct. 1996, doi: 10.1016/S0360-3016(96)00352-5.
- [24] E. Shaw *et al.*, ‘Prospective Randomized Trial of Low- Versus High-Dose Radiation Therapy in Adults With Supratentorial Low-Grade Glioma: Initial Report of a North Central Cancer Treatment Group/Radiation Therapy Oncology Group/Eastern Cooperative Oncology Group Study’, *J. Clin. Oncol.*, vol. 20, no. 9, pp. 2267–2276, May 2002, doi: 10.1200/JCO.2002.09.126.
- [25] D. Zierhut, ‘EXTERNAL RADIOTHERAPY OF PITUITARY ADENOMAS’. <https://reader.elsevier.com/reader/sd/pii/0360301695000716?token=A99839C52A07EE57DC1A2B6C2350077A5D3ABA98E376F6575BDB8D5E854BC25F031BECDB1CB16959388E2BA7CFA857AB&originRegion=eu-west-1&originCreation=20220828101306> (accessed Aug. 28, 2022).
- [26] W. M. McCollough, R. B. Marcus, A. L. Rhoton, W. E. Ballinger, and R. R. Million, ‘Long-term follow-up of radiotherapy for pituitary adenoma: The absence of late

- recurrence after ≥ 4500 cGy', *Int. J. Radiat. Oncol. Biol. Phys.*, vol. 21, no. 3, pp. 607–614, Aug. 1991, doi: 10.1016/0360-3016(91)90677-V.
- [27] P. R. M. Thomas *et al.*, 'Low-Stage Medulloblastoma: Final Analysis of Trial Comparing Standard-Dose With Reduced-Dose Neuraxis Irradiation', *J. Clin. Oncol.*, vol. 18, no. 16, pp. 3004–3011, Aug. 2000, doi: 10.1200/JCO.2000.18.16.3004.
- [28] C. Carrie *et al.*, 'Conformal radiotherapy, reduced boost volume, hyperfractionated radiotherapy, and online quality control in standard-risk medulloblastoma without chemotherapy: Results of the French M-SFOP 98 protocol', *Int. J. Radiat. Oncol.*, vol. 63, no. 3, pp. 711–716, Nov. 2005, doi: 10.1016/j.ijrobp.2005.03.031.
- [29] J. G. Scott *et al.*, 'Personalizing Radiotherapy Prescription Dose Using Genomic Markers of Radiosensitivity'. Rochester, NY, Apr. 15, 2019. doi: 10.2139/ssrn.3372429.
- [30] M. M. Santos and U. P. C. Neves, 'ROC Analysis in Radiotherapy : A TCP Model-Based Test', vol. 2013, no. June, pp. 186–193, 2013, doi: 10.4236/ojapps.2013.32025.
- [31] K. Yang *et al.*, 'A multidimensional nomogram combining overall stage , dose volume histogram parameters and radiomics to predict progression-free survival in patients with locoregionally advanced nasopharyngeal carcinoma', *Oral Oncol.*, vol. 98, no. June, pp. 85–91, 2019, doi: 10.1016/j.oraloncology.2019.09.022.
- [32] S. Su *et al.*, 'Pemetrexed plus cisplatin versus docetaxel plus cisplatin for stage IV lung adenocarcinoma based on propensity score matching', *Anticancer. Drugs*, vol. 30, no. 3, pp. 295–301, Mar. 2019, doi: 10.1097/CAD.0000000000000729.
- [33] A. Ajdari, M. Niyazi, N. H. Nicolay, C. Thieke, R. Jeraj, and T. Bortfeld, 'Towards optimal stopping in radiation therapy', *Radiother. Oncol.*, vol. 134, pp. 96–100, May 2019, doi: 10.1016/j.radonc.2019.01.010.
- [34] H. Rodney Withers, J. M. G. Taylor, and B. Maciejewski, 'Treatment volume and tissue tolerance', *Int. J. Radiat. Oncol.*, vol. 14, no. 4, pp. 751–759, Apr. 1988, doi: 10.1016/0360-3016(88)90098-3.
- [35] P. Okunieff, D. Morgan, A. Niemierko, and H. D. Suit, 'Radiation dose-response of human tumors', *Int. J. Radiat. Oncol. Biol. Phys.*, vol. 32, no. 4, pp. 1227–1237, 1995, doi: 10.1016/0360-3016(94)00475-Z.
- [36] E. J. Hall and A. J. Giaccia, *Radiobiology for the Radiologist*. Lippincott Williams & Wilkins, 2006.
- [37] B. Emami, 'Tolerance of Normal Tissue to Therapeutic Radiation', *Rep. Radiother. Oncol.*, vol. 1, no. 1, pp. 36–48, 2013, doi: 10.1016/0360-3016(91)90171-Y.
- [38] R. Pacelli and L. Mansi, 'Eric Hall and Amato J. Giaccia: Radiobiology for the radiologist, 6th edn.', *Eur. J. Nucl. Med. Mol. Imaging*, vol. 34, no. 6, pp. 965–966, Jun. 2007, doi: 10.1007/s00259-007-0383-8.
- [39] H. A. Gay and A. Niemierko, 'A free program for calculating EUD-based NTCP and TCP in external beam radiotherapy', *Phys. Med.*, vol. 23, no. 3–4, pp. 115–125, 2007, doi: 10.1016/j.ejmp.2007.07.001.
- [40] S. Webb, *The Physics of Conformal Radiotherapy: Advances in Technology (PBK)*. CRC Press, 1997.
- [41] C. M. van Leeuwen *et al.*, 'The alfa and beta of tumours: A review of parameters of the linear-quadratic model, derived from clinical radiotherapy studies', *Radiat. Oncol.*, vol. 13, no. 1, pp. 1–11, 2018, doi: 10.1186/s13014-018-1040-z.
- [42] S. Webb and A. E. Nahum, 'A model for calculating tumour control probability in radiotherapy including the effects of inhomogeneous distributions of dose and

- clonogenic cell density', *Phys. Med. Biol.*, vol. 38, no. 6, pp. 653–666, Jun. 1993, doi: 10.1088/0031-9155/38/6/001.
- [43] J. D. Fenwick, 'Predicting the radiation control probability of heterogeneous tumour ensembles: data analysis and parameter estimation using a closed-form expression', *Phys. Med. Biol.*, vol. 43, no. 8, pp. 2159–2178, Aug. 1998, doi: 10.1088/0031-9155/43/8/012.
- [44] S. A. Roberts and J. H. Hendry, 'A realistic closed-form radiobiological model of clinical tumor-control data incorporating intertumor heterogeneity', *Int. J. Radiat. Oncol.*, vol. 41, no. 3, pp. 689–699, Jun. 1998, doi: 10.1016/S0360-3016(98)00100-X.
- [45] T. E. Schultheiss, C. G. Orton, and R. A. Peck, 'Models in radiotherapy: Volume effects', *Med. Phys.*, vol. 10, no. 4, pp. 410–415, 1983, doi: 10.1118/1.595312.
- [46] J. T. Lyman, 'Complication Probability as Assessed from Dose-Volume Histograms', *Radiat. Res. Suppl.*, vol. 8, pp. S13–S19, 1985, doi: 10.2307/3583506.
- [47] G. J. Kutcher, C. Burman, L. Brewster, M. Goitein, and R. Mohan, 'Histogram reduction method for calculating complication probabilities for three-dimensional treatment planning evaluations', *Int. J. Radiat. Oncol. Biol. Phys.*, vol. 21, no. 1, pp. 137–146, May 1991, doi: 10.1016/0360-3016(91)90173-2.
- [48] C. Burman, G. J. Kutcher, B. Emami, and M. Goitein, 'Fitting of normal tissue tolerance data to an analytic function', *Int. J. Radiat. Oncol. Biol. Phys.*, vol. 21, no. 1, pp. 123–135, 1991, doi: 10.1016/0360-3016(91)90172-Z.
- [49] J. P. Kirkpatrick, A. J. van der Kogel, and T. E. Schultheiss, 'Radiation Dose–Volume Effects in the Spinal Cord', *Int. J. Radiat. Oncol. Biol. Phys.*, vol. 76, no. 3, pp. S42–S49, Mar. 2010, doi: 10.1016/j.ijrobp.2009.04.095.
- [50] N. Bhandare *et al.*, 'Radiation Therapy and Hearing Loss', *Int. J. Radiat. Oncol. Biol. Phys.*, vol. 76, no. 3, pp. S50–S57, Mar. 2010, doi: 10.1016/j.ijrobp.2009.04.096.
- [51] C. Mayo, E. Yorke, and T. E. Merchant, 'Radiation Associated Brainstem Injury', *Int. J. Radiat. Oncol.*, vol. 76, no. 3, Supplement, pp. S36–S41, Mar. 2010, doi: 10.1016/j.ijrobp.2009.08.078.
- [52] C. Mayo, M. K. Martel, L. B. Marks, J. Flickinger, J. Nam, and J. Kirkpatrick, 'Radiation Dose–Volume Effects of Optic Nerves and Chiasm', *Int. J. Radiat. Oncol. Biol. Phys.*, vol. 76, no. 3, pp. S28–S35, Mar. 2010, doi: 10.1016/j.ijrobp.2009.07.1753.
- [53] Y. R. Lawrence *et al.*, 'Radiation Dose–Volume Effects in the Brain', *Int. J. Radiat. Oncol. Biol. Phys.*, vol. 76, no. 3, pp. S20–S27, Mar. 2010, doi: 10.1016/j.ijrobp.2009.02.091.
- [54] 'Table of Contents page: International Journal of Radiation Oncology, Biology, Physics'. [https://www.redjournal.org/issue/S0360-3016\(10\)X0002-5](https://www.redjournal.org/issue/S0360-3016(10)X0002-5) (accessed Aug. 30, 2022).
- [55] D. Freund, R. Zhang, M. Sanders, and W. Newhauser, 'Predictive Risk of Radiation Induced Cerebral Necrosis in Pediatric Brain Cancer Patients after VMAT Versus Proton Therapy', *Cancers*, vol. 7, no. 2, Art. no. 2, Jun. 2015, doi: 10.3390/cancers7020617.
- [56] A. J. Cole *et al.*, 'Investigating the Potential Impact of Four-dimensional Computed Tomography (4DCT) on Toxicity, Outcomes and Dose Escalation for Radical Lung Cancer Radiotherapy', *Clin. Oncol.*, vol. 26, no. 3, pp. 142–150, Mar. 2014, doi: 10.1016/j.clon.2013.11.024.

- [57] A. Ajdari, Z. Liao, R. Mohan, X. Wei, and T. Bortfeld, ‘Personalized mid-course FDG-PET based adaptive treatment planning for non-small cell lung cancer using machine learning and optimization’, *Phys. Med. Biol.*, vol. 67, no. 18, p. 185015, Sep. 2022, doi: 10.1088/1361-6560/ac88b3.
- [58] S. Gaito *et al.*, ‘Normal Tissue Complication Probability Modelling for Toxicity Prediction and Patient Selection in Proton Beam Therapy to the Central Nervous System: A Literature Review’, *Clin. Oncol.*, vol. 34, no. 6, pp. e225–e237, Jun. 2022, doi: 10.1016/j.clon.2021.12.015.
- [59] G. Palma *et al.*, ‘Modelling the risk of radiation induced alopecia in brain tumor patients treated with scanned proton beams’, *Radiother. Oncol.*, vol. 144, pp. 127–134, Mar. 2020, doi: 10.1016/j.radonc.2019.11.013.
- [60] M. Dell’Oro, P. Wilson, M. Short, C.-H. Hua, T. E. Merchant, and E. Bezak, ‘Normal tissue complication probability modeling to guide individual treatment planning in pediatric cranial proton and photon radiotherapy’, *Med. Phys.*, vol. 49, no. 1, pp. 742–755, 2022, doi: 10.1002/mp.15360.
- [61] J. Schuster *et al.*, ‘A phase II, multicenter trial of rindopepimut (CDX-110) in newly diagnosed glioblastoma: the ACT III study’, *Neuro-Oncol.*, vol. 17, no. 6, pp. 854–861, Jun. 2015, doi: 10.1093/neuonc/nou348.
- [62] R. Stupp *et al.*, ‘Radiotherapy plus Concomitant and Adjuvant Temozolomide for Glioblastoma’, *N. Engl. J. Med.*, vol. 352, no. 10, pp. 987–996, Mar. 2005, doi: 10.1056/NEJMoa043330.
- [63] D. G. Brachman *et al.*, ‘Phase 1/2 trials of Temozolomide, Motexafin Gadolinium, and 60-Gy fractionated radiation for newly diagnosed supratentorial glioblastoma multiforme: final results of RTOG 0513’, *Int. J. Radiat. Oncol. Biol. Phys.*, vol. 91, no. 5, pp. 961–967, Apr. 2015, doi: 10.1016/j.ijrobp.2014.12.050.
- [64] A. Shergalis, A. Bankhead, U. Luesakul, N. Muangsin, and N. Neamati, ‘Current Challenges and Opportunities in Treating Glioblastoma’, *Pharmacol. Rev.*, vol. 70, no. 3, pp. 412–445, Jul. 2018, doi: 10.1124/pr.117.014944.
- [65] M. Patel *et al.*, ‘Salvage reirradiation for recurrent glioblastoma with radiosurgery: radiographic response and improved survival’, *J. Neurooncol.*, vol. 92, no. 2, pp. 185–191, Apr. 2009, doi: 10.1007/s11060-008-9752-9.
- [66] M. Weller, T. Cloughesy, J. R. Perry, and W. Wick, ‘Standards of care for treatment of recurrent glioblastoma--are we there yet?’, *Neuro-Oncol.*, vol. 15, no. 1, pp. 4–27, Jan. 2013, doi: 10.1093/neuonc/nos273.
- [67] M. T. Milano, A. W. Katz, and P. Okunieff, ‘Patterns of recurrence after curative-intent radiation for oligometastases confined to one organ’, *Am. J. Clin. Oncol.*, vol. 33, no. 2, pp. 157–163, Apr. 2010, doi: 10.1097/COC.0b013e3181979238.
- [68] M. W. McDonald, H.-K. G. Shu, W. J. Curran, and I. R. Crocker, ‘Pattern of Failure After Limited Margin Radiotherapy and Temozolomide for Glioblastoma’, *Int. J. Radiat. Oncol. Biol. Phys.*, vol. 79, no. 1, pp. 130–136, Jan. 2011, doi: 10.1016/j.ijrobp.2009.10.048.
- [69] K. Petrecca, M.-C. Guiot, V. Panet-Raymond, and L. Souhami, ‘Failure pattern following complete resection plus radiotherapy and temozolomide is at the resection margin in patients with glioblastoma’, *J. Neurooncol.*, vol. 111, no. 1, pp. 19–23, Jan. 2013, doi: 10.1007/s11060-012-0983-4.
- [70] J. Sherriff *et al.*, ‘Patterns of relapse in glioblastoma multiforme following concomitant chemoradiotherapy with temozolomide’, *Br. J. Radiol.*, vol. 86, no. 1022, p. 20120414, Feb. 2013, doi: 10.1259/bjr.20120414.

- [71] B. J. Gebhardt, M. C. Dobelbower, W. H. Ennis, A. K. Bag, J. M. Markert, and J. B. Fiveash, 'Patterns of failure for glioblastoma multiforme following limited-margin radiation and concurrent temozolomide', *Radiat. Oncol.*, vol. 9, no. 1, p. 130, Jun. 2014, doi: 10.1186/1748-717X-9-130.
- [72] J. Paulsson and P. Micke, 'Prognostic relevance of cancer-associated fibroblasts in human cancer', *Semin. Cancer Biol.*, vol. 25, pp. 61–68, Apr. 2014, doi: 10.1016/j.semcancer.2014.02.006.
- [73] S. H. Choi *et al.*, 'Impact of Including Peritumoral Edema in Radiotherapy Target Volume on Patterns of Failure in Glioblastoma following Temozolomide-based Chemoradiotherapy', *Sci. Rep.*, vol. 7, no. 1, Art. no. 1, Feb. 2017, doi: 10.1038/srep42148.
- [74] P. Tini *et al.*, 'Epidermal Growth Factor Receptor Expression Predicts Time and Patterns of Recurrence in Patients with Glioblastoma After Radiotherapy and Temozolomide', *World Neurosurg.*, vol. 109, pp. e662–e668, Jan. 2018, doi: 10.1016/j.wneu.2017.10.052.
- [75] M. Gromeier *et al.*, 'Very low mutation burden is a feature of inflamed recurrent glioblastomas responsive to cancer immunotherapy', *Nat. Commun.*, vol. 12, no. 1, Art. no. 1, Jan. 2021, doi: 10.1038/s41467-020-20469-6.
- [76] M. Tanaka, Y. Ino, K. Nakagawa, M. Tago, and T. Todo, 'High-dose conformal radiotherapy for supratentorial malignant glioma: a historical comparison', *Lancet Oncol.*, vol. 6, no. 12, pp. 953–960, Dec. 2005, doi: 10.1016/S1470-2045(05)70395-8.
- [77] K. Nakagawa *et al.*, 'High-dose conformal radiotherapy influenced the pattern of failure but did not improve survival in glioblastoma multiforme', *Int. J. Radiat. Oncol. Biol. Phys.*, vol. 40, no. 5, pp. 1141–1149, Mar. 1998, doi: 10.1016/s0360-3016(97)00911-5.
- [78] G. Minniti *et al.*, 'Patterns of failure and comparison of different target volume delineations in patients with glioblastoma treated with conformal radiotherapy plus concomitant and adjuvant temozolomide', *Radiother. Oncol.*, vol. 97, no. 3, pp. 377–381, 2010, doi: 10.1016/j.radonc.2010.08.020.
- [79] R. Stupp *et al.*, 'Effects of radiotherapy with concomitant and adjuvant temozolomide versus radiotherapy alone on survival in glioblastoma in a randomised phase III study: 5-year analysis of the EORTC-NCIC trial', *Lancet Oncol.*, vol. 10, no. 5, pp. 459–466, May 2009, doi: 10.1016/S1470-2045(09)70025-7.
- [80] J. R. Perry *et al.*, 'Short-Course Radiation plus Temozolomide in Elderly Patients with Glioblastoma', *N. Engl. J. Med.*, vol. 376, no. 11, pp. 1027–1037, Mar. 2017, doi: 10.1056/NEJMoa1611977.
- [81] C. Thilmann, A. Zabel, K. H. Grosser, A. Hoess, M. Wannemacher, and J. Debus, 'Intensity-modulated radiotherapy with an integrated boost to the macroscopic tumor volume in the treatment of high-grade gliomas', *Int. J. Cancer*, vol. 96, no. 6, pp. 341–349, 2001, doi: 10.1002/ijc.1042.
- [82] K. Sultanem *et al.*, 'The use of hypofractionated intensity-modulated irradiation in the treatment of glioblastoma multiforme: preliminary results of a prospective trial', *Int. J. Radiat. Oncol. Biol. Phys.*, vol. 58, no. 1, pp. 247–252, Jan. 2004, doi: 10.1016/s0360-3016(03)00819-8.
- [83] N. S. Floyd *et al.*, 'Hypofractionated intensity-modulated radiotherapy for primary glioblastoma multiforme', *Int. J. Radiat. Oncol.*, vol. 58, no. 3, pp. 721–726, Mar. 2004, doi: 10.1016/S0360-3016(03)01623-7.

- [84] A. M. Monjazez *et al.*, ‘A PHASE I DOSE ESCALATION STUDY OF HYPOFRACTIONATED IMRT FIELD-IN-FIELD BOOST FOR NEWLY DIAGNOSED GLIOBLASTOMA MULTIFORME’, *Int. J. Radiat. Oncol. Biol. Phys.*, vol. 82, no. 2, p. 743, Feb. 2012, doi: 10.1016/j.ijrobp.2010.10.018.
- [85] M. F. Chan, K. Schupak, C. Burman, C.-S. Chui, and C. C. Ling, ‘Comparison of intensity-modulated radiotherapy with three-dimensional conformal radiation therapy planning for glioblastoma multiforme’, *Med. Dosim.*, vol. 28, no. 4, pp. 261–265, Dec. 2003, doi: 10.1016/j.meddos.2003.08.004.
- [86] M. Suzuki, ‘Feasibility Study of the Simultaneous Integrated Boost (SIB) Method for Malignant Gliomas Using Intensity-modulated Radiotherapy (IMRT)’, *Jpn. J. Clin. Oncol.*, vol. 33, no. 6, pp. 271–277, Jun. 2003, doi: 10.1093/jjco/hyg053.
- [87] T. Iuchi *et al.*, ‘Phase 2 trial of hypofractionated high-dose intensity modulated radiation therapy with concurrent and adjuvant temozolomide for newly diagnosed glioblastoma’, *Int. J. Radiat. Oncol. Biol. Phys.*, vol. 88, no. 4, pp. 793–800, Mar. 2014, doi: 10.1016/j.ijrobp.2013.12.011.
- [88] K. Nakamatsu *et al.*, ‘Treatment outcomes and dose-volume histogram analysis of simultaneous integrated boost method for malignant gliomas using intensity-modulated radiotherapy’, *Int. J. Clin. Oncol.*, vol. 13, no. 1, pp. 48–53, Feb. 2008, doi: 10.1007/s10147-007-0722-6.
- [89] K. H. Cho *et al.*, ‘Simultaneous integrated boost intensity-modulated radiotherapy in patients with high-grade gliomas’, *Int. J. Radiat. Oncol. Biol. Phys.*, vol. 78, no. 2, pp. 390–397, 2010, doi: 10.1016/j.ijrobp.2009.08.029.
- [90] V. Panet-Raymond *et al.*, ‘Accelerated Hypofractionated Intensity-Modulated Radiotherapy With Concurrent and Adjuvant Temozolomide for Patients With Glioblastoma Multiforme: A Safety and Efficacy Analysis’, *Int. J. Radiat. Oncol.*, vol. 73, no. 2, pp. 473–478, Feb. 2009, doi: 10.1016/j.ijrobp.2008.04.030.
- [91] K. Reddy *et al.*, ‘Phase II Trial of Hypofractionated IMRT With Temozolomide for Patients With Newly Diagnosed Glioblastoma Multiforme’, *Int. J. Radiat. Oncol.*, vol. 84, no. 3, pp. 655–660, Nov. 2012, doi: 10.1016/j.ijrobp.2012.01.035.
- [92] C. Chen *et al.*, ‘Phase I trial of hypofractionated intensity-modulated radiotherapy with temozolomide chemotherapy for patients with newly diagnosed glioblastoma multiforme’, *Int. J. Radiat. Oncol. Biol. Phys.*, vol. 81, no. 4, pp. 1066–1074, Nov. 2011, doi: 10.1016/j.ijrobp.2010.07.021.
- [93] M. Massacesi *et al.*, ‘Accelerated intensity-modulated radiotherapy plus temozolomide in patients with glioblastoma: a phase I dose-escalation study (ISIDE-BT-1)’, *Int. J. Clin. Oncol.*, vol. 18, no. 5, pp. 784–791, Oct. 2013, doi: 10.1007/s10147-012-0462-0.
- [94] D. E. Ney *et al.*, ‘Phase II trial of hypofractionated intensity-modulated radiation therapy combined with temozolomide and bevacizumab for patients with newly diagnosed glioblastoma’, *J. Neurooncol.*, vol. 122, no. 1, pp. 135–143, Mar. 2015, doi: 10.1007/s11060-014-1691-z.
- [95] G. Truc *et al.*, ‘A phase I dose escalation study using simultaneous integrated-boost IMRT with temozolomide in patients with unifocal glioblastoma’, *Cancer/Radiotherapie*, vol. 20, no. 3, pp. 193–198, 2016, doi: 10.1016/j.canrad.2015.12.005.
- [96] G. Shenouda *et al.*, ‘A Phase 2 Trial of Neoadjuvant Temozolomide Followed by Hypofractionated Accelerated Radiation Therapy With Concurrent and Adjuvant

- Temozolomide for Patients With Glioblastoma’, *Int. J. Radiat. Oncol.*, vol. 97, no. 3, pp. 487–494, Mar. 2017, doi: 10.1016/j.ijrobp.2016.11.006.
- [97] S. Scoccianti *et al.*, ‘Hypofractionated radiotherapy with simultaneous integrated boost (SIB) plus temozolomide in good prognosis patients with glioblastoma: a multicenter phase II study by the Brain Study Group of the Italian Association of Radiation Oncology (AIRO)’, *Radiol. Med. (Torino)*, vol. 123, no. 1, pp. 48–62, Jan. 2018, doi: 10.1007/s11547-017-0806-y.
- [98] S. Mallick *et al.*, ‘Hypofractionated accelerated radiotherapy (HART) with concurrent and adjuvant temozolomide in newly diagnosed glioblastoma: a phase II randomized trial (HART-GBM trial)’, *J. Neurooncol.*, vol. 140, no. 1, pp. 75–82, Oct. 2018, doi: 10.1007/s11060-018-2932-3.
- [99] N. Jastaniyah *et al.*, ‘Phase I study of hypofractionated intensity modulated radiation therapy with concurrent and adjuvant temozolomide in patients with glioblastoma multiforme’, *Radiat. Oncol. Lond. Engl.*, vol. 8, p. 38, Feb. 2013, doi: 10.1186/1748-717X-8-38.
- [100] M. Azoulay *et al.*, ‘A phase I/II trial of 5-fraction stereotactic radiosurgery with 5-mm margins with concurrent temozolomide in newly diagnosed glioblastoma: primary outcomes’, *Neuro-Oncol.*, vol. 22, no. 8, pp. 1182–1189, Aug. 2020, doi: 10.1093/neuonc/noaa019.
- [101] R. Cardinale *et al.*, ‘A phase II trial of accelerated radiotherapy using weekly stereotactic conformal boost for supratentorial glioblastoma multiforme: RTOG 0023’, *Int. J. Radiat. Oncol.*, vol. 65, no. 5, pp. 1422–1428, Aug. 2006, doi: 10.1016/j.ijrobp.2006.02.042.
- [102] A. Omuro *et al.*, ‘Phase II Study of Bevacizumab, Temozolomide and Hypofractionated Stereotactic Radiotherapy for Newly Diagnosed Glioblastoma’, *Clin. Cancer Res. Off. J. Am. Assoc. Cancer Res.*, vol. 20, no. 19, pp. 5023–5031, Oct. 2014, doi: 10.1158/1078-0432.CCR-14-0822.
- [103] J. G. Douglas *et al.*, ‘[F-18]-fluorodeoxyglucose positron emission tomography for targeting radiation dose escalation for patients with glioblastoma multiforme: Clinical outcomes and patterns of failure’, *Int. J. Radiat. Oncol. Biol. Phys.*, vol. 64, no. 3, pp. 886–891, Mar. 2006, doi: 10.1016/j.ijrobp.2005.08.013.
- [104] M. D. Piroth *et al.*, ‘Integrated boost IMRT with FET-PET-adapted local dose escalation in glioblastomas’, *Strahlenther. Onkol.*, vol. 188, no. 4, pp. 334–339, Apr. 2012, doi: 10.1007/s00066-011-0060-5.
- [105] C. I. Tsien *et al.*, ‘Concurrent Temozolomide and Dose-Escalated Intensity Modulated Radiation Therapy in Newly Diagnosed Glioblastoma’, *Clin. Cancer Res.*, vol. 18, no. 1, pp. 273–279, Jan. 2012, doi: 10.1158/1078-0432.CCR-11-2073.
- [106] S. Ken *et al.*, ‘Integration method of 3D MR spectroscopy into treatment planning system for glioblastoma IMRT dose painting with integrated simultaneous boost’, *Radiat. Oncol.*, vol. 8, no. 1, pp. 1–9, 2013, doi: 10.1186/1748-717X-8-1.
- [107] A. Laprie *et al.*, ‘Dose-painting multicenter phase III trial in newly diagnosed glioblastoma: The SPECTRO-GLIO trial comparing arm A standard radiochemotherapy to arm B radiochemotherapy with simultaneous integrated boost guided by MR spectroscopic imaging’, *BMC Cancer*, vol. 19, no. 1, pp. 1–10, 2019, doi: 10.1186/s12885-019-5317-x.
- [108] R. Kosztyła, S. Raman, V. Moiseenko, S. Reinsberg, B. Toyota, and A. Nichol, ‘Dose-painted volumetric modulated arc therapy of phenylalanine positron emission tomography’, *Br. J. Radiol.*, vol. 92, no. april 2019, pp. 1–9, 2019.

- [109] O. J. Gurney-Champion *et al.*, ‘Quantitative imaging for radiotherapy purposes’, *Radiother. Oncol.*, vol. 146, pp. 66–75, 2020, doi: 10.1016/j.radonc.2020.01.026.
- [110] V. S. Khoo and D. L. Joon, ‘New developments in MRI for target volume delineation in radiotherapy’, *Br. J. Radiol.*, vol. 79, no. special_issue_1, pp. S2–S15, Sep. 2006, doi: 10.1259/bjr/41321492.
- [111] ‘Imaging-Based Treatment Adaptation in Radiation Oncology | Journal of Nuclear Medicine’. <https://jnm.snmjournals.org/content/56/12/1922> (accessed Dec. 30, 2022).
- [112] U. A. van der Heide, A. C. Houweling, G. Groenendaal, R. G. H. Beets-Tan, and P. Lambin, ‘Functional MRI for radiotherapy dose painting’, *Magn. Reson. Imaging*, vol. 30, no. 9, pp. 1216–1223, 2012, doi: 10.1016/j.mri.2012.04.010.
- [113] Y. Wang *et al.*, ‘Quantitative MRI: Defining repeatability, reproducibility and accuracy for prostate cancer imaging biomarker development’, *Magn. Reson. Imaging*, vol. 77, pp. 169–179, 2021, doi: 10.1016/j.mri.2020.12.018.
- [114] T. Welzel *et al.*, ‘Diagnostic accuracy of DW MR imaging in the differentiation of chordomas and chondrosarcomas of the skull base: A 3.0-T MRI study of 105 cases’, *Eur. J. Radiol.*, vol. 105, pp. 119–124, Aug. 2018, doi: 10.1016/j.ejrad.2018.05.026.
- [115] A. Surov, G. Hamerla, H. J. Meyer, K. Winter, S. Schob, and E. Fiedler, ‘Whole lesion histogram analysis of meningiomas derived from ADC values. Correlation with several cellularity parameters, proliferation index KI 67, nucleic content, and membrane permeability’, *Magn. Reson. Imaging*, vol. 51, pp. 158–162, Sep. 2018, doi: 10.1016/j.mri.2018.05.009.
- [116] A. van der Toorn *et al.*, ‘Dynamic changes in water ADC, energy metabolism, extracellular space volume, and tortuosity in neonatal rat brain during global ischemia’, *Magn. Reson. Med.*, vol. 36, no. 1, pp. 52–60, 1996, doi: 10.1002/mrm.1910360110.
- [117] Y. Lu, L. Liu, S. Luan, J. Xiong, D. Geng, and B. Yin, ‘The diagnostic value of texture analysis in predicting WHO grades of meningiomas based on ADC maps: an attempt using decision tree and decision forest’, *Eur. Radiol.*, vol. 29, no. 3, pp. 1318–1328, 2019, doi: 10.1007/s00330-018-5632-7.
- [118] R. Bammer, ‘Basic principles of diffusion-weighted imaging’, *Eur. J. Radiol.*, vol. 45, no. 3, pp. 169–184, Mar. 2003, doi: 10.1016/S0720-048X(02)00303-0.
- [119] E. M. Charles-Edwards, ‘Diffusion-weighted magnetic resonance imaging and its application to cancer’.
- [120] D. L. Bihan and E. Breton, ‘Imagerie de diffusion in-vivo par résonance magnétique nucléaire’, *Comptes-Rendus Académie Sci.*, vol. 93, no. 5, p. 27, 1985.
- [121] D. Le Bihan, E. Breton, D. Lallemand, M. L. Aubin, J. Vignaud, and M. Laval-Jeantet, ‘Separation of diffusion and perfusion in intravoxel incoherent motion MR imaging.’, *Radiology*, vol. 168, no. 2, pp. 497–505, Aug. 1988, doi: 10.1148/radiology.168.2.3393671.
- [122] D.-M. Koh, D. J. Collins, and M. R. Orton, ‘Intravoxel incoherent motion in body diffusion-weighted MRI: reality and challenges’, *AJR Am. J. Roentgenol.*, vol. 196, no. 6, pp. 1351–1361, Jun. 2011, doi: 10.2214/AJR.10.5515.
- [123] T. Sugahara *et al.*, ‘Usefulness of diffusion-weighted MRI with echo-planar technique in the evaluation of cellularity in gliomas’, *J. Magn. Reson. Imaging*, vol. 9, no. 1, pp. 53–60, 1999, doi: 10.1002/(SICI)1522-2586(199901)9:1<53::AID-JMRI7>3.0.CO;2-2.
- [124] R. K. Gupta *et al.*, ‘Relationships between choline magnetic resonance spectroscopy, apparent diffusion coefficient and quantitative histopathology in

- human glioma’, *J. Neurooncol.*, vol. 50, no. 3, pp. 215–226, 2000, doi: 10.1023/A:1006431120031.
- [125] D.-M. Koh and D. J. Collins, ‘Diffusion-Weighted MRI in the Body: Applications and Challenges in Oncology’, *Am. J. Roentgenol.*, Nov. 2012, doi: 10.2214/AJR.06.1403.
- [126] S. Leibfarth, R. M. Winter, H. Lyng, D. Zips, and D. Thorwarth, ‘Potentials and challenges of diffusion-weighted magnetic resonance imaging in radiotherapy’, *Clin. Transl. Radiat. Oncol.*, vol. 13, pp. 29–37, Nov. 2018, doi: 10.1016/j.ctro.2018.09.002.
- [127] C. Tsien, Y. Cao, and T. Chenevert, ‘Clinical Applications for Diffusion Magnetic Resonance Imaging in Radiotherapy’, *Semin. Radiat. Oncol.*, vol. 24, no. 3, pp. 218–226, Jul. 2014, doi: 10.1016/j.semradonc.2014.02.004.
- [128] D. A. Hamstra *et al.*, ‘Evaluation of the functional diffusion map as an early biomarker of time-to-progression and overall survival in high-grade glioma’, *Proc. Natl. Acad. Sci.*, vol. 102, no. 46, pp. 16759–16764, Nov. 2005, doi: 10.1073/pnas.0508347102.
- [129] B. A. Moffat *et al.*, ‘Functional diffusion map: A noninvasive MRI biomarker for early stratification of clinical brain tumor response’, *Proc. Natl. Acad. Sci.*, vol. 102, no. 15, pp. 5524–5529, Apr. 2005, doi: 10.1073/pnas.0501532102.
- [130] O. Casares-Magaz, U. A. Van Der Heide, J. Rørvik, P. Steenbergen, and L. P. Muren, ‘A tumour control probability model for radiotherapy of prostate cancer using magnetic resonance imaging-based apparent diffusion coefficient maps’, *Radiother. Oncol.*, vol. 119, no. 1, pp. 111–116, Apr. 2016, doi: 10.1016/j.radonc.2016.02.030.
- [131] G. Buizza, ‘MRI-based tumour control probability model in particle therapy PV-0311 Poster viewing 6: Radiobiological modelling and quantitative imaging’, *J. Roentgenol.*, vol. 198, no. 6, pp. 597–601, 2012, doi: 10.3252/pso.eu.ESTRO38.2019.
- [132] A. Doskaliyev *et al.*, ‘Lymphomas and glioblastomas: differences in the apparent diffusion coefficient evaluated with high b-value diffusion-weighted magnetic resonance imaging at 3T’, *Eur. J. Radiol.*, vol. 81, no. 2, pp. 339–344, Feb. 2012, doi: 10.1016/j.ejrad.2010.11.005.
- [133] B. M. Ellingson *et al.*, ‘Validation of functional diffusion maps (fDMs) as a biomarker for human glioma cellularity’, *J. Magn. Reson. Imaging JMRI*, vol. 31, no. 3, pp. 538–548, Mar. 2010, doi: 10.1002/jmri.22068.
- [134] O. Lindvall and Z. Kokaia, ‘Stem cells for the treatment of neurological disorders’, *Nature*, vol. 441, no. 7097, pp. 1094–1096, Jun. 2006, doi: 10.1038/nature04960.
- [135] C. E. Eyler and J. N. Rich, ‘Survival of the fittest: cancer stem cells in therapeutic resistance and angiogenesis’, *J. Clin. Oncol. Off. J. Am. Soc. Clin. Oncol.*, vol. 26, no. 17, pp. 2839–2845, Jun. 2008, doi: 10.1200/JCO.2007.15.1829.
- [136] J. A. Gallaher *et al.*, ‘From cells to tissue: How cell scale heterogeneity impacts glioblastoma growth and treatment response’, *PLoS Comput. Biol.*, vol. 16, no. 2, p. e1007672, Feb. 2020, doi: 10.1371/journal.pcbi.1007672.
- [137] A. R. Cabrera *et al.*, ‘Radiation therapy for glioblastoma: Executive summary of an American Society for Radiation Oncology Evidence-Based Clinical Practice Guideline’, *Pract. Radiat. Oncol.*, vol. 6, no. 4, pp. 217–225, Jul. 2016, doi: 10.1016/j.prro.2016.03.007.
- [138] M. Niyazi *et al.*, ‘ESTRO-ACROP guideline “target delineation of glioblastomas”’, *Radiother. Oncol. J. Eur. Soc. Ther. Radiol. Oncol.*, vol. 118, no. 1, pp. 35–42, Jan. 2016, doi: 10.1016/j.radonc.2015.12.003.

- [139] C. C. Ling *et al.*, ‘Towards multidimensional radiotherapy (MD-CRT): Biological imaging and biological conformality’, *Int. J. Radiat. Oncol. Biol. Phys.*, vol. 47, no. 3, pp. 551–560, 2000, doi: 10.1016/S0360-3016(00)00467-3.
- [140] C. N. Johnson-Hart, G. J. Price, C. Faivre-Finn, M. C. Aznar, and M. van Herk, ‘Residual Setup Errors Towards the Heart After Image Guidance Linked With Poorer Survival in Lung Cancer Patients: Do We Need Stricter IGRT Protocols?’, *Int. J. Radiat. Oncol. Biol. Phys.*, vol. 102, no. 2, pp. 434–442, Oct. 2018, doi: 10.1016/j.ijrobp.2018.05.052.
- [141] D. Thorwarth, ‘Biologically adapted radiation therapy’, *Z. Für Med. Phys.*, vol. 28, no. 3, pp. 177–183, Aug. 2018, doi: 10.1016/j.zemedi.2017.08.001.
- [142] S. M. Bentzen, ‘Theragnostic imaging for radiation oncology: Dose-painting by numbers’, *Lancet Oncol.*, vol. 6, no. 2, pp. 112–117, 2005, doi: 10.1016/S1470-2045(05)01737-7.
- [143] D. Thorwarth, S.-M. Eschmann, F. Paulsen, and M. Alber, ‘Hypoxia dose painting by numbers: a planning study’, *Int. J. Radiat. Oncol. Biol. Phys.*, vol. 68, no. 1, pp. 291–300, May 2007, doi: 10.1016/j.ijrobp.2006.11.061.
- [144] D. Thorwarth, X. Geets, and M. Paiusco, ‘Physical radiotherapy treatment planning based on functional PET/CT data’, *Radiother. Oncol.*, vol. 96, no. 3, pp. 317–324, Sep. 2010, doi: 10.1016/j.radonc.2010.07.012.
- [145] E. Jiménez-Ortega *et al.*, ‘Dose painting by means of Monte Carlo treatment planning at the voxel level’, *Phys. Med.*, vol. 42, pp. 339–344, Oct. 2017, doi: 10.1016/j.ejmp.2017.04.005.
- [146] C. C. Ling, X. A. Li, and W. R. Hendee, ‘Over the next decade the success of radiation treatment planning will be judged by the immediate biological response of tumor cells rather than by surrogate measures such as dose maximization and uniformity’, *Med. Phys.*, vol. 32, no. 7Part1, pp. 2189–2192, 2005, doi: 10.1118/1.1930908.
- [147] S. M. Bentzen, ‘Dose Painting and Theragnostic Imaging: Towards the Prescription, Planning and Delivery of Biologically Targeted Dose Distributions in External Beam Radiation Oncology’, in *Radiation Oncology Advances*, S. M. Bentzen, P. M. Harari, W. A. Tomé, and M. P. Mehta, Eds., in *Cancer Treatment and Research*. Boston, MA: Springer US, 2008, pp. 40–61. doi: 10.1007/978-0-387-36744-6_3.
- [148] M. Busk, M. R. Horsman, and J. Overgaard, ‘Resolution in PET hypoxia imaging: Voxel size matters’, *Acta Oncol.*, vol. 47, no. 7, pp. 1201–1210, Jan. 2008, doi: 10.1080/02841860802307716.
- [149] S. Chen, D. Yan, A. Qin, P. Maniawski, D. J. Krauss, and G. D. Wilson, ‘Effect of uncertainties in quantitative 18F-FDG PET/CT imaging feedback for intratumoral dose-response assessment and dose painting by number’, *Med. Phys.*, vol. 47, no. 11, pp. 5681–5692, 2020, doi: 10.1002/mp.14482.
- [150] E. G. C. Troost, J. Bussink, A. L. Hoffmann, O. C. Boerman, W. J. G. Oyen, and J. H. A. M. Kaanders, ‘18F-FLT PET/CT for Early Response Monitoring and Dose Escalation in Oropharyngeal Tumors’, *J. Nucl. Med.*, vol. 51, no. 6, pp. 866–874, Jun. 2010, doi: 10.2967/jnumed.109.069310.
- [151] X. Shi, X. Meng, X. Sun, L. Xing, and J. Yu, ‘PET/CT imaging-guided dose painting in radiation therapy’, *Cancer Lett.*, vol. 355, no. 2, pp. 169–175, Dec. 2014, doi: 10.1016/j.canlet.2014.07.042.

- [152] I. Madani *et al.*, ‘Positron Emission Tomography-Guided, Focal-Dose Escalation Using Intensity-Modulated Radiotherapy for Head and Neck Cancer’, *Int. J. Radiat. Oncol.*, vol. 68, no. 1, pp. 126–135, May 2007, doi: 10.1016/j.ijrobp.2006.12.070.
- [153] J. Fleckenstein *et al.*, ‘F-18-FDG-PET Confined Radiotherapy of Locally Advanced NSCLC With Concomitant Chemotherapy: Results of the PET-PLAN Pilot Trial’, *Int. J. Radiat. Oncol.*, vol. 81, no. 4, pp. e283–e289, Nov. 2011, doi: 10.1016/j.ijrobp.2011.01.020.
- [154] F. Kong *et al.*, ‘A phase II trial of mid-treatment FDG-PET adaptive, individualized radiation therapy plus concurrent chemotherapy in patients with non-small cell lung cancer (NSCLC).’, *J. Clin. Oncol.*, vol. 31, no. 15_suppl, pp. 7522–7522, May 2013, doi: 10.1200/jco.2013.31.15_suppl.7522.
- [155] E. Grönlund, S. Johansson, A. Montelius, and A. Ahnesjö, ‘Dose painting by numbers based on retrospectively determined recurrence probabilities’, *Radiother. Oncol.*, vol. 122, no. 2, pp. 236–241, 2017, doi: 10.1016/j.radonc.2016.09.007.
- [156] M. Witte, G. Shakirin, A. Houweling, H. Peulen, and M. van Herk, ‘Dealing with geometric uncertainties in dose painting by numbers: Introducing the ΔV_{H1} This work was supported by Dutch Cancer Society grant 2007-3895.1’, *Radiother. Oncol.*, vol. 100, no. 3, pp. 402–406, Sep. 2011, doi: 10.1016/j.radonc.2011.08.028.
- [157] M. A. Deveau, S. R. Bowen, D. C. Westerly, and R. Jeraj, ‘Feasibility and sensitivity study of helical tomotherapy for dose painting plans’, *Acta Oncol.*, vol. 49, no. 7, pp. 991–996, Oct. 2010, doi: 10.3109/0284186X.2010.500302.
- [158] D. Thorwarth and M. Alber, ‘Implementation of hypoxia imaging into treatment planning and delivery’, *Radiother. Oncol.*, vol. 97, no. 2, pp. 172–175, Nov. 2010, doi: 10.1016/j.radonc.2010.05.012.
- [159] B. Vanderstraeten, W. Duthoy, W. D. Gerssem, W. D. Neve, and H. Thierens, ‘[18F]fluoro-deoxy-glucose positron emission tomography ([18F]FDG-PET) voxel intensity-based intensity-modulated radiation therapy (IMRT) for head and neck cancer’, *Radiother. Oncol.*, vol. 79, no. 3, pp. 249–258, Jun. 2006, doi: 10.1016/j.radonc.2006.03.003.
- [160] D. Berwouts *et al.*, ‘Three-phase adaptive dose-painting-by-numbers for head-and-neck cancer: initial results of the phase I clinical trial’, *Radiother. Oncol.*, vol. 107, no. 3, pp. 310–316, Jun. 2013, doi: 10.1016/j.radonc.2013.04.002.
- [161] S. S. Korreman *et al.*, ‘Feasibility of dose painting using volumetric modulated arc optimization and delivery Feasibility of dose painting using volumetric modulated arc optimization and delivery’, 2010, doi: 10.3109/0284186X.2010.498440.
- [162] E. Grönlund, E. Almhagen, S. Johansson, E. Traneus, and A. Ahnesjö, ‘Robust maximization of tumor control probability for radicality constrained radiotherapy dose painting by numbers of head and neck cancer’, *Phys. Imaging Radiat. Oncol.*, vol. 12, no. September, pp. 56–62, 2019, doi: 10.1016/j.phro.2019.11.004.
- [163] M. R. Arnesen *et al.*, ‘Dose painting by numbers in a standard treatment planning system using inverted dose prescription maps’, *Acta Oncol.*, vol. 54, no. 9, pp. 1607–1613, Oct. 2015, doi: 10.3109/0284186X.2015.1061690.
- [164] S. M. Bentzen and V. Gregoire, ‘Molecular Imaging–Based Dose Painting: A Novel Paradigm for Radiation Therapy Prescription’, *Semin. Radiat. Oncol.*, vol. 21, no. 2, pp. 101–110, Apr. 2011, doi: 10.1016/j.semradonc.2010.10.001.
- [165] G. Meijer, J. Steenhuijsen, M. Bal, K. De Jaeger, D. Schuring, and J. Theuws, ‘Dose painting by contours versus dose painting by numbers for stage II/III lung cancer: practical implications of using a broad or sharp brush’, *Radiother. Oncol. J. Eur. Soc.*

- Ther. Radiol. Oncol.*, vol. 100, no. 3, pp. 396–401, Sep. 2011, doi: 10.1016/j.radonc.2011.08.048.
- [166] T. F. DeLaney, ‘Proton Therapy in the Clinic’, *IMRT IGRT SBRT*, vol. 43, pp. 465–485, 2011, doi: 10.1159/000322511.
- [167] A. E. Nahum, D. P. Dearnaley, and G. G. Steel, ‘Prospects for proton-beam radiotherapy’, *Eur. J. Cancer*, vol. 30, no. 10, pp. 1577–1583, Jan. 1994, doi: 10.1016/0959-8049(94)00316-W.
- [168] A. Wambersie, ‘The future of high-let radiation in cancer therapy Justification of the heavy-ion therapy programmes’, International Atomic Energy Agency (IAEA), 1989.
- [169] H. Paganetti and T. Bortfeld, ‘Proton Therapy’, in *New Technologies in Radiation Oncology*, W. Schlegel, T. Bortfeld, and A.-L. Grosu, Eds., in Medical Radiology. Berlin, Heidelberg: Springer, 2006, pp. 345–363. doi: 10.1007/3-540-29999-8_27.
- [170] ‘Proton Therapy | Advanced Radiation Therapy Treatment | Provision’, *Provision Healthcare*. <https://provisionhealthcare.com/about-proton-therapy/advantages-of-proton/> (accessed Sep. 01, 2022).
- [171] W. S. Lee, S.-J. Seo, H. K. Chung, J. W. Park, J.-K. Kim, and E. H. Kim, ‘Tumor-treating fields as a proton beam-sensitizer for glioblastoma therapy’, *Am. J. Cancer Res.*, vol. 11, no. 9, pp. 4582–4594, Sep. 2021.
- [172] R. R. Wilson, ‘Radiological Use of Fast Protons’, *Radiology*, vol. 47, no. 5, pp. 487–491, Nov. 1946, doi: 10.1148/47.5.487.
- [173] ‘PTCOG - Home’. <https://www.ptcog.ch/> (accessed Sep. 01, 2022).
- [174] H. Media, ‘Cost vs Benefits: The Controversy Over Proton Beam Radiotherapy’, *Oncology Nurse Advisor*, Feb. 28, 2018. <https://www.oncologynurseadvisor.com/home/cancer-types/general-oncology/cost-vs-benefits-the-controversy-over-proton-beam-radiotherapy/> (accessed Sep. 02, 2022).
- [175] U. Schneider, E. Pedroni, and A. Lomax, ‘The calibration of CT Hounsfield units for radiotherapy treatment planning’, *Phys. Med. Biol.*, vol. 41, no. 1, pp. 111–124, 1996, doi: 10.1088/0031-9155/41/1/009.
- [176] B. Schaffner and E. Pedroni, ‘The precision of proton range calculations in proton radiotherapy treatment planning: experimental verification of the relation between CT-HU and proton stopping power’, *Phys. Med. Biol.*, vol. 43, no. 6, pp. 1579–1592, 1998, doi: 10.1088/0031-9155/43/6/016.
- [177] ‘ICRU Report 78, Prescribing, Recording, and Reporting Proton-Beam Therapy – ICRU’. <https://www.icru.org/report/prescribing-recording-and-reporting-proton-beam-therapy-icru-report-78/> (accessed Sep. 01, 2022).
- [178] D. Maleike, J. Unkelbach, and U. Oelfke, ‘Simulation and visualization of dose uncertainties due to interfractional organ motion’, *Phys. Med. Biol.*, vol. 51, no. 9, pp. 2237–2252, 2006, doi: 10.1088/0031-9155/51/9/009.
- [179] M. Cubillos-Mesías *et al.*, ‘Impact of robust treatment planning on single- and multi-field optimized plans for proton beam therapy of unilateral head and neck target volumes’, *Radiat. Oncol.*, vol. 12, no. 1, p. 190, Nov. 2017, doi: 10.1186/s13014-017-0931-8.
- [180] A. Fredriksson, A. Forsgren, and B. Hårdemark, ‘Minimax optimization for handling range and setup uncertainties in proton therapy’, *Med. Phys.*, vol. 38, no. 3, pp. 1672–1684, 2011, doi: 10.1118/1.3556559.

- [181] D. Pflugfelder, J. J. Wilkens, and U. Oelfke, ‘Worst case optimization: a method to account for uncertainties in the optimization of intensity modulated proton therapy’, *Phys. Med. Biol.*, vol. 53, no. 6, pp. 1689–1700, 2008, doi: 10.1088/0031-9155/53/6/013.
- [182] C. Liu *et al.*, ‘Robust Optimization for Intensity Modulated Proton Therapy to Redistribute High Linear Energy Transfer from Nearby Critical Organs to Tumors in Head and Neck Cancer’, *Int. J. Radiat. Oncol. Biol. Phys.*, vol. 107, no. 1, pp. 181–193, 2020, doi: 10.1016/j.ijrobp.2020.01.013.
- [183] D. Corwin *et al.*, ‘Toward Patient-Specific, Biologically Optimized Radiation Therapy Plans for the Treatment of Glioblastoma’, *PLOS ONE*, vol. 8, no. 11, p. e79115, Nov. 2013, doi: 10.1371/journal.pone.0079115.
- [184] M. Baumann and C. Petersen, ‘TCP and NTCP: a basic introduction’, *Rays*, vol. 30, no. 2, pp. 99–104, Apr. 2005.
- [185] M. Atiq, A. Atiq, K. Iqbal, Q. Shamsi, F. Andleeb, and S. A. Buzdar, ‘Evaluation of dose conformity and coverage of target volume for intensity-modulated radiotherapy of pelvic cancer treatment’, *Indian J. Cancer*, vol. 54, no. 1, pp. 379–384, 2017, doi: 10.4103/ijc.IJC_80_17.
- [186] ‘Dose Volume Histogram ’, *Medical Physics Blog*, May 19, 2021. <https://medicalphysics.blog/2021/05/19/dose-volume-histogram/> (accessed Sep. 05, 2022).
- [187] P. Wootton, ‘Dose Specification for Reporting External Beam Therapy with Photons and Electrons’, *Med. Phys.*, vol. 6, no. 6, pp. 541–542, 1979, doi: 10.1118/1.594621.
- [188] ‘ICRU Report 50, Prescribing, Recording, and Reporting Photon Beam Therapy – ICRU’. <https://www.icru.org/report/prescribing-recording-and-reporting-photon-beam-therapy-report-50/> (accessed Sep. 01, 2022).
- [189] S. F. C. O’Rourke, H. McAneney, and T. Hillen, ‘Linear quadratic and tumour control probability modelling in external beam radiotherapy’, *J. Math. Biol.*, vol. 58, no. 4–5, pp. 799–817, 2009, doi: 10.1007/s00285-008-0222-y.
- [190] B. Warkentin, P. Stavrev, N. Stavreva, C. Field, and B. G. Fallone, ‘A TCP-NTCP estimation module using DVHs and known radiobiological models and parameter sets’, *J. Appl. Clin. Med. Phys.*, vol. 5, no. 1, pp. 50–63, 2004, doi: 10.1120/jacmp.v5i1.1970.
- [191] P. Pedicini *et al.*, ‘Clinical radiobiology of glioblastoma multiforme’, *Strahlenther. Onkol.*, vol. 190, no. 10, pp. 925–932, Oct. 2014, doi: 10.1007/s00066-014-0638-9.
- [192] X. S. Qi, C. J. Schultz, and X. A. Li, ‘An estimation of radiobiologic parameters from clinical outcomes for radiation treatment planning of brain tumor’, *Int. J. Radiat. Oncol. Biol. Phys.*, vol. 64, no. 5, pp. 1570–1580, 2006, doi: 10.1016/j.ijrobp.2005.12.022.
- [193] L. Barazzuol, N. G. Burnet, R. Jena, B. Jones, S. J. Jefferies, and N. F. Kirkby, ‘A mathematical model of brain tumour response to radiotherapy and chemotherapy considering radiobiological aspects’, *J. Theor. Biol.*, vol. 262, no. 3, pp. 553–565, 2010, doi: 10.1016/j.jtbi.2009.10.021.
- [194] D. M. Brizel, K. Light, S.-M. Zhou, and L. B. Marks, ‘Conformal radiation therapy treatment planning reduces the dose to the optic structures for patients with tumors of the paranasal sinuses’, *Radiother. Oncol.*, vol. 51, no. 3, pp. 215–218, Jun. 1999, doi: 10.1016/S0167-8140(99)00043-2.

- [195] G. L. Jiang *et al.*, ‘Radiation-induced injury to the visual pathway’, *Radiother. Oncol.*, vol. 30, no. 1, pp. 17–25, Jan. 1994, doi: 10.1016/0167-8140(94)90005-1.
- [196] M. K. Martel *et al.*, ‘Dose-volume complication analysis for visual pathway structures of patients with advanced paranasal sinus tumors’, *Int. J. Radiat. Oncol.*, vol. 38, no. 2, pp. 273–284, May 1997, doi: 10.1016/S0360-3016(97)00029-1.
- [197] C. Giannini *et al.*, ‘Anaplastic Oligodendroglial Tumors: Refining the Correlation among Histopathology, 1p 19q Deletion and Clinical Outcome in Intergroup Radiation Therapy Oncology Group Trial 9402’, *Brain Pathol.*, vol. 18, no. 3, pp. 360–369, Mar. 2008, doi: 10.1111/j.1750-3639.2008.00129.x.
- [198] M. Bou Zerdan and H. I. Assi, ‘Oligodendroglioma: A Review of Management and Pathways’, *Front. Mol. Neurosci.*, vol. 14, p. 722396, Oct. 2021, doi: 10.3389/fnmol.2021.722396.
- [199] ‘Phase III Trial of Chemotherapy Plus Radiotherapy Compared With Radiotherapy Alone for Pure and Mixed Anaplastic Oligodendroglioma: Intergroup Radiation Therapy Oncology Group Trial 9402 | Journal of Clinical Oncology’. https://ascopubs.org/doi/10.1200/JCO.2005.04.3414?url_ver=Z39.88-2003&rfr_id=ori:rid:crossref.org&rfr_dat=cr_pub%20%20pubmed (accessed Oct. 10, 2022).
- [200] M. Wang *et al.*, ‘Cognition and Quality of Life After Chemotherapy Plus Radiotherapy (RT) vs. RT for Pure and Mixed Anaplastic Oligodendrogliomas: Radiation Therapy Oncology Group Trial 9402’, *Int. J. Radiat. Oncol.*, vol. 77, no. 3, pp. 662–669, Jul. 2010, doi: 10.1016/j.ijrobp.2009.06.004.
- [201] M. Mizumoto *et al.*, ‘Radiation Therapy for Grade 3 Gliomas: Correlation of MRI Findings With Prognosis’, *Cureus*, vol. 13, no. 8, p. e16887, doi: 10.7759/cureus.16887.
- [202] F. Y. Moraes and C. Chung, ‘Radiation for skull base meningiomas: review of the literature on the approach to radiotherapy’, *Chin. Clin. Oncol.*, vol. 6, no. Suppl 1, Art. no. Suppl 1, Jul. 2017, doi: 10.21037/cco.2017.06.08.
- [203] L. Rogers *et al.*, ‘Intermediate-risk meningioma: initial outcomes from NRG Oncology RTOG 0539’, *J. Neurosurg.*, vol. 129, no. 1, pp. 35–47, Jul. 2018, doi: 10.3171/2016.11.JNS161170.
- [204] C. L. Rogers *et al.*, ‘High-risk Meningioma: Initial Outcomes From NRG Oncology/RTOG 0539’, *Int. J. Radiat. Oncol. Biol. Phys.*, vol. 106, no. 4, pp. 790–799, Mar. 2020, doi: 10.1016/j.ijrobp.2019.11.028.
- [205] K. Seidensaal *et al.*, ‘Radiotherapy in the treatment of aggressive fibromatosis: experience from a single institution’, *Radiat. Oncol.*, vol. 15, no. 1, p. 143, Jun. 2020, doi: 10.1186/s13014-020-01565-9.
- [206] L. Khan, H. Soliman, A. Sahgal, J. Perry, W. Xu, and M. N. Tsao, ‘External beam radiation dose escalation for high grade glioma’, *Cochrane Database Syst. Rev.*, no. 5, 2020, doi: 10.1002/14651858.CD011475.pub3.
- [207] B. Jeremic *et al.*, ‘Hyperfractionated radiation therapy for incompletely resected supratentorial low-grade glioma. A phase II study’, *Radiother. Oncol.*, vol. 49, no. 1, pp. 49–54, Oct. 1998, doi: 10.1016/S0167-8140(98)00074-7.
- [208] T. Bortfeld and R. Jeraj, ‘The physical basis and future of radiation therapy’, *Br. J. Radiol.*, vol. 84, no. 1002, pp. 485–498, Jun. 2011, doi: 10.1259/bjr/86221320.
- [209] S.-P. Weathers and M. R. Gilbert, ‘Current challenges in designing GBM trials for immunotherapy’, *J. Neurooncol.*, vol. 123, no. 3, pp. 331–337, Jul. 2015, doi: 10.1007/s11060-015-1716-2.

- [210] M. R. Gilbert *et al.*, ‘Dose-Dense Temozolomide for Newly Diagnosed Glioblastoma: A Randomized Phase III Clinical Trial’, *J. Clin. Oncol.*, vol. 31, no. 32, pp. 4085–4091, Nov. 2013, doi: 10.1200/JCO.2013.49.6968.
- [211] M. M. Fitzek *et al.*, ‘Accelerated fractionated proton/photon irradiation to 90 cobalt gray equivalent for glioblastoma multiforme: results of a phase II prospective trial’, *J. Neurosurg.*, vol. 91, no. 2, pp. 251–260, Aug. 1999, doi: 10.3171/jns.1999.91.2.0251.
- [212] M. A. Schmidt and G. S. Payne, ‘Radiotherapy planning using MRI’, *Phys. Med. Biol.*, vol. 60, no. 22, pp. R323–R361, 2015, doi: 10.1088/0031-9155/60/22/R323.
- [213] K. W. Yeom *et al.*, ‘Diffusion-Weighted MRI: Distinction of Skull Base Chordoma from Chondrosarcoma’, *Am. J. Neuroradiol.*, vol. 34, no. 5, pp. 1056–1061, May 2013, doi: 10.3174/ajnr.A3333.
- [214] W. C. Dewey, L. E. Hopwood, S. A. Sapareto, and L. E. Gerweck, ‘Cellular Responses to Combinations of Hyperthermia and Radiation’, *Radiology*, vol. 123, no. 2, pp. 463–474, May 1977, doi: 10.1148/123.2.463.
- [215] G. S. Stamatakos, V. P. Antipas, N. K. Uzunoglu, and R. G. Dale, ‘A four-dimensional computer simulation model of the in vivo response to radiotherapy of glioblastoma multiforme: studies on the effect of clonogenic cell density’, *Br. J. Radiol.*, vol. 79, no. 941, pp. 389–400, May 2006, doi: 10.1259/bjr/30604050.
- [216] T. Kikuchi, T. Kumabe, S. Higano, M. Watanabe, and T. Tominaga, ‘Minimum apparent diffusion coefficient for the differential diagnosis of ganglioglioma’, *Neurol. Res.*, vol. 31, no. 10, pp. 1102–1107, Dec. 2009, doi: 10.1179/174313209X382539.
- [217] R. Murakami *et al.*, ‘Magnetic Resonance Imaging of Pilocytic Astrocytomas: Usefulness of the Minimum Apparent Diffusion Coefficient (ADC) Value for Differentiation from High-Grade Gliomas’, *Acta Radiol.*, vol. 49, no. 4, pp. 462–467, Jan. 2008, doi: 10.1080/02841850801918555.
- [218] Y. Hayashida *et al.*, ‘Diffusion-weighted Imaging of Metastatic Brain Tumors: Comparison with Histologic Type and Tumor Cellularity’, *Am. J. Neuroradiol.*, vol. 27, no. 7, pp. 1419–1425, Aug. 2006.
- [219] J. Chen *et al.*, ‘[Correlation between magnetic resonance diffusion weighted imaging and cell density in astrocytoma]’, *Zhonghua Zhong Liu Za Zhi*, vol. 27, no. 5, pp. 309–311, May 2005.
- [220] A. C. Guo, T. J. Cummings, R. C. Dash, and J. M. Provenzale, ‘Lymphomas and High-Grade Astrocytomas: Comparison of Water Diffusibility and Histologic Characteristics’, *Radiology*, vol. 224, no. 1, pp. 177–183, Jul. 2002, doi: 10.1148/radiol.2241010637.
- [221] K. Kono *et al.*, ‘The Role of Diffusion-weighted Imaging in Patients with Brain Tumors’, *Am. J. Neuroradiol.*, vol. 22, no. 6, pp. 1081–1088, Jun. 2001.
- [222] K. Gauvain *et al.*, ‘Evaluating Pediatric Brain Tumor Cellularity with Diffusion-Tensor Imaging’, *AJR Am. J. Roentgenol.*, vol. 177, pp. 449–54, Sep. 2001, doi: 10.2214/ajr.177.2.1770449.
- [223] O. Eidel *et al.*, ‘Automatic analysis of cellularity in glioblastoma and correlation with ADC using trajectory analysis and automatic nuclei counting’, *PLoS ONE*, vol. 11, no. 7, pp. 1–10, 2016, doi: 10.1371/journal.pone.0160250.
- [224] V. Brancato, S. Nuzzo, L. Tramontano, G. Condorelli, M. Salvatore, and C. Cavaliere, ‘Predicting Survival in Glioblastoma Patients Using Diffusion MR Imaging Metrics—A Systematic Review’, *Cancers*, vol. 12, no. 10, Art. no. 10, Oct. 2020, doi: 10.3390/cancers12102858.

- [225] B. S. Kim *et al.*, ‘Apparent Diffusion Coefficient as a Predictive Biomarker for Survival in Patients with Treatment-Naive Glioblastoma Using Quantitative Multiparametric Magnetic Resonance Profiling’, *World Neurosurg.*, vol. 122, pp. e812–e820, Feb. 2019, doi: 10.1016/j.wneu.2018.10.151.
- [226] ‘NiftyReg - CMIC’. <http://cmictig.cs.ucl.ac.uk/wiki/index.php/NiftyReg> (accessed Sep. 02, 2022).
- [227] S. Ali, N. M. Joseph, A. Perry, R. F. Barajas, and S. Cha, ‘Apparent diffusion coefficient in glioblastoma with PNET-like components, a GBM variant’, *J. Neurooncol.*, vol. 119, no. 2, pp. 353–360, Sep. 2014, doi: 10.1007/s11060-014-1485-3.
- [228] R. F. Barajas *et al.*, ‘Glioblastoma Multiforme Regional Genetic and Cellular Expression Patterns: Influence on Anatomic and Physiologic MR Imaging1’, *Radiology*, vol. 254, no. 2, pp. 564–576, Feb. 2010, doi: 10.1148/radiol.09090663.
- [229] M. Neska-Matuszewska, J. Bladowska, M. Sasiadek, and A. Zimny, ‘Differentiation of glioblastoma multiforme, metastases and primary central nervous system lymphomas using multiparametric perfusion and diffusion MR imaging of a tumor core and a peritumoral zone—Searching for a practical approach’, *PLOS ONE*, vol. 13, no. 1, p. e0191341, Jan. 2018, doi: 10.1371/journal.pone.0191341.
- [230] C. C. Ko *et al.*, ‘Differentiation between Glioblastoma Multiforme and Primary Cerebral Lymphoma: Additional Benefits of Quantitative Diffusion-Weighted MR Imaging’, *PLOS ONE*, vol. 11, no. 9, p. e0162565, Sep. 2016, doi: 10.1371/journal.pone.0162565.
- [231] E. Grönlund, S. Johansson, T. Nyholm, C. Thellenberg, and A. Ahnesjö, ‘Dose painting of prostate cancer based on Gleason score correlations with apparent diffusion coefficients’, *Acta Oncol.*, vol. 57, no. 5, pp. 574–581, 2018, doi: 10.1080/0284186X.2017.1415457.
- [232] M. Orlandi *et al.*, ‘Feasibility of voxel-based Dose Painting for recurrent Glioblastoma guided by ADC values of Diffusion-Weighted MR imaging’, *Phys. Med.*, vol. 32, no. 12, pp. 1651–1658, 2016, doi: 10.1016/j.ejmp.2016.11.106.
- [233] D. J. Brenner, L. R. Hlatky, P. J. Hahnfeldt, E. J. Hall, and R. K. Sachs, ‘A convenient extension of the linear-quadratic model to include redistribution and reoxygenation’, *Int. J. Radiat. Oncol.*, vol. 32, no. 2, pp. 379–390, May 1995, doi: 10.1016/0360-3016(95)00544-9.
- [234] E. K. Liu, E. P. Sulman, P. Y. Wen, and S. C. Kurz, ‘Novel Therapies for Glioblastoma’, *Curr. Neurol. Neurosci. Rep.*, vol. 20, no. 7, p. 19, May 2020, doi: 10.1007/s11910-020-01042-6.
- [235] P. D. Brown *et al.*, ‘A prospective phase II randomized trial of proton radiotherapy vs intensity-modulated radiotherapy for patients with newly diagnosed glioblastoma’, *Neuro-Oncol.*, vol. 23, no. 8, pp. 1337–1347, Aug. 2021, doi: 10.1093/neuonc/noab040.
- [236] R. Mohan *et al.*, ‘Proton therapy reduces the likelihood of high-grade radiation-induced lymphopenia in glioblastoma patients: phase II randomized study of protons vs photons’, *Neuro-Oncol.*, vol. 23, no. 2, pp. 284–294, Aug. 2020, doi: 10.1093/neuonc/noaa182.
- [237] K. A. Al Feghali *et al.*, ‘Phase II trial of proton therapy versus photon IMRT for GBM: secondary analysis comparison of progression-free survival between RANO

- versus clinical assessment’, *Neuro-Oncol. Adv.*, vol. 3, no. 1, p. vdab073, Jun. 2021, doi: 10.1093/noajnl/vdab073.
- [238] R. T. Flynn, S. R. Bowen, S. M. Bentzen, T. R. Mackie, and R. Jeraj, ‘Intensity-modulated x-ray (IMXT) versus proton (IMPT) therapy for theragnostic hypoxia-based dose painting’, *Phys. Med. Biol.*, vol. 53, no. 15, pp. 4153–4167, 2008, doi: 10.1088/0031-9155/53/15/010.
- [239] D. Thorwarth, M. Soukup, and M. Alber, ‘Dose painting with IMPT, helical tomotherapy and IMXT: A dosimetric comparison’, *Radiother. Oncol.*, vol. 86, no. 1, pp. 30–34, Jan. 2008, doi: 10.1016/j.radonc.2007.11.003.
- [240] V. Gondi *et al.*, ‘Radiotherapy (RT) Dose-intensification (DI) Using Intensity-modulated RT (IMRT) versus Standard-dose (SD) RT with Temozolomide (TMZ) in Newly Diagnosed Glioblastoma (GBM): Preliminary Results of NRG Oncology BN001’, *Int. J. Radiat. Oncol. Biol. Phys.*, vol. 108, no. 3, pp. S22–S23, Nov. 2020, doi: 10.1016/j.ijrobp.2020.07.2109.
- [241] F. P. Cammarata *et al.*, ‘Proton therapy and src family kinase inhibitor combined treatments on U87 human glioblastoma multiforme cell line’, *Int. J. Mol. Sci.*, vol. 20, no. 19, 2019, doi: 10.3390/ijms20194745.
- [242] F. Albertini, E. B. Hug, and A. J. Lomax, ‘Is it necessary to plan with safety margins for actively scanned proton therapy?’, *Phys. Med. Biol.*, vol. 56, no. 14, pp. 4399–4413, 2011, doi: 10.1088/0031-9155/56/14/011.
- [243] F. Tommasino *et al.*, ‘Clinical implementation in proton therapy of multi-field optimization by a hybrid method combining conventional PTV with robust optimization’, *Phys. Med. Ampmathsemicolon Biol.*, vol. 65, no. 4, p. 045002, 2020, doi: 10.1088/1361-6560/ab63b9.
- [244] X. Ding *et al.*, ‘Improving dosimetric outcome for hippocampus and cochlea sparing whole brain radiotherapy using spot-scanning proton arc therapy’, *Acta Oncol.*, vol. 58, no. 4, pp. 483–490, Apr. 2019, doi: 10.1080/0284186X.2018.1555374.
- [245] W. Liu, Y. Li, and X. Li, ‘Influence of robust optimization in intensity-modulated proton therapy with different dose delivery techniques’, *Med. Phys.*, vol. 39, no. June, pp. 3089–3101, 2012.
- [246] W. Liu *et al.*, ‘Dosimetric benefits of robust treatment planning for intensity modulated proton therapy for base-of-skull cancers’, *Pract. Radiat. Oncol.*, vol. 4, no. 6, pp. 384–391, Nov. 2014, doi: 10.1016/j.prr.2013.12.001.
- [247] U. Schneider, P. Pemler, J. Besserer, E. Pedroni, A. Lomax, and B. Kaser-Hotz, ‘Patient specific optimization of the relation between CT-Hounsfield units and proton stopping power with proton radiography’, *Med. Phys.*, vol. 32, no. 1, pp. 195–199, 2005, doi: 10.1118/1.1833041.
- [248] C. Hahn *et al.*, ‘Impact of range uncertainty on clinical distributions of linear energy transfer and biological effectiveness in proton therapy’, *Med. Phys.*, vol. 47, no. 12, pp. 6151–6162, 2020, doi: 10.1002/mp.14560.
- [249] H. Paganetti *et al.*, ‘Relative biological effectiveness ($\{RBE\}$) values for proton beam therapy’, *Int J Rad Oncol Biol Phys*, vol. 53, no. 2, pp. 407–421, 2002.
- [250] K. Håkansson *et al.*, ‘Radiation dose-painting with protons vs. photons for head-and-neck cancer’, *Acta Oncol.*, vol. 59, no. 5, pp. 525–533, 2020, doi: 10.1080/0284186X.2020.1714720.
- [251] J. Shan, T. T. Sio, C. Liu, S. E. Schild, M. Bues, and W. Liu, ‘A novel and individualized robust optimization method using normalized dose interval volume

- constraints (NDIVC) for intensity-modulated proton radiotherapy’, *Med. Phys.*, vol. 46, no. 1, pp. 382–393, 2019, doi: 10.1002/mp.13276.
- [252] M. Mizumoto *et al.*, ‘Long-term survival after treatment of glioblastoma multiforme with hyperfractionated concomitant boost proton beam therapy’, *Pract. Radiat. Oncol.*, vol. 5, no. 1, pp. e9-16, Feb. 2015, doi: 10.1016/j.prro.2014.03.012.
- [253] W. Liu *et al.*, ‘Effectiveness of robust optimization in intensity-modulated proton therapy planning for head and neck cancers’, *Med. Phys. Med Phys*, vol. 40, no. 10, pp. 51711–481, 2013, doi: 10.1118/1.4801899doi.org/10.1118/1.4801899.
- [254] Q. T. Ostrom *et al.*, ‘CBTRUS Statistical Report: Primary Brain and Other Central Nervous System Tumors Diagnosed in the United States in 2009-2013’, *Neuro-Oncol.*, vol. 18, no. suppl_5, pp. v1–v75, Oct. 2016, doi: 10.1093/neuonc/nov207.
- [255] C. I. Correia Veloso Da Veiga, ‘Toward adaptive radiotherapy’, Doctoral, UCL (University College London), 2016. Accessed: Jan. 04, 2023. [Online]. Available: <https://discovery.ucl.ac.uk/id/eprint/1489630/>
- [256] A. Castellano *et al.*, ‘Advanced imaging techniques for radiotherapy planning of gliomas’, *Cancers*, vol. 13, no. 5, pp. 1–30, 2021, doi: 10.3390/cancers13051063.
- [257] E. Höglund, ‘DNA fragmentation in cultured cells exposed to high linear energy transfer radiation’, 2000, Accessed: Jan. 04, 2023. [Online]. Available: <http://urn.kb.se/resolve?urn=urn:nbn:se:uu:diva-1254>